Optimization of Three-terminal Perovskite/ Silicon Tandem Solar Cell Using Opto-electrical Simulations in TCAD Sentaurus

2022

TU Delft

Musa Al-Zoubi

PVMD Group

EEMCS, TU Delft

10/31/2022

Optimization of Three-terminal Perovskite/Silicon Tandem Solar Cell Using Opto-electrical Simulations in TCAD Sentaurus

by

Musa Al-Zoubi

in partial fulfillment of the requirements for the degree of

Master of Science

in Sustainable Energy Technology

at the Delft University of Technology,

to be defended publicly on Friday October 31st, 2022, at 15:00 PM.

Student number:	4423836		
Supervisor:	Dr. ir. Rudi Santbergen	TU Delft, ESE - PVMD	Main supervisor
	Dr. Paul A. Procel Moya	TU Delft, ESE - PVMD	Daily supervisor
Thesis committee:	Prof. Dr ir. Olindo Isabella	TU Delft, ESE - PVMD	Head of PVMD group
	Dr. Jianning Dong	TU Delft, ESE - DCE&S	External committee member

Abstract

Perovskite/Silicon tandem cells are gradually becoming more promising in the field of photovoltaic technology since they have already surpassed the theoretical power conversion efficiency (PCE) limit of single junction (SJ) silicon cells (~30%), while they can be commercially compatible. Several architectures of Perovskite/silicon devices were proposed. The most known of them are four terminals tandem (4TT) and two terminals tandem (2TT). Which are well researched and have already surpassed the highest efficiency achieved by SJ silicon cells. On the other hand, 3TT is less known architecture which have received less attention in research than 2TT and 4TT but seems to combine the advantages of both and eliminate their disadvantages. Although of the few research done on 3TT, they revealed great potential of achieving high efficiency. Yet it is still practically challenging to design and fabricate stable 3TT devices that bring 30% PCE's goal to reality. To continue unveiling the potential of 3TT perovskite/Si device, more research needs to be done in areas that haven't been investigated before. And that was the target of this project.

The 3TT device structure proposed in this work is a perovskite top cell on a c-Si IBC bottom cell. And the focus of the project was to investigate and optimize the design parameters of the perovskite top cell as well as the IBC bottom cell to improve the overall efficiency of the tandem device using 2D modelling. To achieve these Objectives, a 2-D simulation model template was built for the mentioned tandem device with the help of Sentaurus TCAD. Further, the model template has been validated. Subsequently, the validated model was used to conduct a comparison between the proposed 3TT device and an identical 4TT device to examine the compactivity of the model with other tandem configurations. This has shown that the 3TT model has performed as good as the 4TT model. Both models showed capability of achieving efficiency beyond 30%.

Then, the performance of the 3TT model was examined under different thicknesses of Perovskite layer. This revealed that the 3TT device has the highest efficiency when the perovskite layer has a thickness between 0.5 - 1.2 µm where efficiency higher than 30% can be achieved.

The next step was to investigate and redesign the IBC bottom cell to improve the 3TT performance. First, the device performance under different pitch values in the IBC bottom cell was examined. It was found that the lower the pitch is, the higher the performance becomes. It was also found that the pitch value doesn't influence only the bottom cell but also the top cell. Which makes the performance of 3TT device more sensitive to pitch values than the SJ IBC cell. Second, the rear emitter to base ratio in the IBC bottom cell was investigated. Which showed that the emitter/base ratio has less influence on the 3TT behavior when the pitch value is within or less than the range of the diffusion length of the bulk material. But the influence of the ratio grows up when the pitch is higher. The 3TT device has its peak performance when the ratio is between 2:1 to 4:1.

After that, the tandem model was redesigned to corporate all the outcomes that was found in previous steps. This resulted in several scenarios based on best parameters to design 3TT models with the best outcome. Four scenarios have been suggested where each of them can achieve PCE higher than 31.5 %.

Finally, we have studied the effect of surface recombination on the performance of the 3TT device. Which revealed that most of surface recombination losses are coming from the interfaces between perovskite layer and ETL or HTL layers. Therefore, if these surface recombination losses are suppressed, that will lead to a PCE higher than 33 %.

Acknowledgment

I would like to thank the following people, whom I could not have been able to complete this research without their help. Neither I would have made it through my master's degree.

First, I would like to thank all the staff members in the SET program and the PMVD group who made this master program such a rich and diverse experience to the students. And who helped me whenever it is possible to flourish my knowledge and to extend my professional experience.

Second, I would like to express my sincere gratitude to my main supervisor Dr.ir. Rudi Santbergen for the help and tips he offered and for his genuine effort to guide me to produce excellent work. Also, for my daily supervisor Dr. Paul Procel Moya for his great assistance in learning Sentaurus software and tackling the daily challenges which I was facing in opto-electrical stimulations. And for Prof. Olindo Isabella and Dr. Jianning Dong for taking the time to assist and evaluate my thesis work and to be part of the thesis committee.

Also, my deep thanks to Dr. Malte Vogt for sharing with me some of his data, to Mark Vielvoije for his technical assistance and tips, and to Antoon Frehe for his technical assistance.

And my biggest thanks to my family for all the support that they have shown me through this journey and for being patient and caring.

Musa Al-Zoubi
Delft, October 2022

Contents

List of Figures

List of Tables

Nomenclature

1-D	One Dimensional
2-D	Two Dimensional
2T	Two Terminals
2TT	Two Terminals Tandem
3-D	Three Dimensional
3T	Three Terminals
3TT	Three Terminal Tandem
4T	Four Terminals
4TT	Four Terminal Tandem
A	Absorption
AM	Air Mass coefficient
ARC	Anti-reflecting coating
a-Si:H	Intrinsic hydrogenated amorphous silicon
BSF	Back surface field
CdTe	Cadmium telluride
CIGS	Copper indium gallium diselenide
c-Si	Crystalline Silicon
DJ	Dual Junction
E_{Fo}	Fermi Energy at equilibrium
E_{Fn} (E_{Fp})	Fermi energy level for electrons (holes)
E_g	Bandgap Energy
E_{ph}	Photon Energy
ETL	Electrons Transporting Layer
EY	Energy Yields
FEM	Finite element method
FF	Filling Factor
HTL	Holes Transporting Layer
IBC	Interdigitated Back Contact
I_{sc}	Short circuit Current
I_{mpp}	Maximum Power Point Current
ITO	Indium Tin Oxide
J	Current density
J_{sc}	Short circuit current density
J_{mpp}	Maximum Power Point Current Density
J_{ph}	Photo-current density
J-V	Current density-Voltage
LCOE	Levelized Cost of Energy
$MAPbI_3$	Archetypal methylammonium lead iodide
MJ	Multi Junction
MPP or mpp	Maximum Power Point
OGR	Optical generation rate
PCE	Power Conversion Efficiency
poly-Si(n+)	Polysilicon heavily doped with n-type
poly-Si(p+)	Polysilicon heavily doped with p-type
PSC	Perovskite Solar Cell
P-V	Power-voltage
PV	Photovoltaic

SBOB	Selective band offset barrier
SJ	Single Junction
SQ	Shockley–Queisser
SDE	Sentaurus structure design editor
S.Device	Sentaurus device
STC	Standard Test Condition
SVisual	Sentaurus visual
SWB	Sentaurus workbench
TCO	Transparent conductive Oxide
TF	Thin film
TOPCon	Tunnel oxide passivated contact
V_{bi}	Build-in voltage
V_{mpp}	Maximum Power Point Voltage
V_{oc}	Open Circuit Voltage

ϵ	Dielectric primitivity
η	Efficiency
λ	Wavelength
μ_n (μ_p)	Electron (hole) mobility
$\phi(\lambda)$	Spectral photons flux
X_e	Electron affinity

1 Introduction

1.1 Motivation

While global energy demand is growing, fossil fuels remain the major current energy sources although they are scarce and depleting [1]. Therefore, fossil fuels won't be able to meet energy demands soon. Moreover, continuing using fossil fuels speeds up environmental damage and climate change since it is the main contributor to CO2 emissions [2]. Thus, Renewable green energy, in particular solar energy, is the only feasible solution to these challenges since it can be accessed anywhere in the world and available in abundant quantities [3].

In the last decades, the most efficient approach to harvest solar energy so far was the photovoltaic (PV) technology. Where solar energy is converted to electricity [3]. PV technology is gradually becoming dominant among energy generating technologies around the globe. In recent years, energy generated from PV devices has achieved a competing levelized cost of energy (LCOE) comparable to or even lower than energy generated by fossil fuel technologies [4]. This is the result of continues reduction in the cost of PV cell production and enhancing the power conversion efficiency (PCE) of the cell.

But since the dominant commercial PV types in the market are single junction (SJ) devices and they are approaching their theoretical PCE and industrial fabrication costs limits. Therefore, we are looking at new novel technologies that further can push solar generated energy beyond these limits (efficiency & costs).

The next section explains briefly the working principle of PV solar cell and further explores its main limitations.

1.2 Photovoltaic technology and solar cells

Solar spectrum:

Solar energy is the electromagnetic radiation received from sun. The spectrum of this radiation nearly matches a black body radiation of 5,800 K [5]. The extraterrestrial solar spectrum measured at the top regions of the earth's atmosphere is referred as AM0 spectrum corresponds to total power density of 1353 W/m², the acronym AM0 stands for air mass zero [6]. The air mass coefficient anywhere on earth surface in reference to AM0 can be calculated according to the following formula:

$$AM = \frac{1}{\cos(\theta)} \qquad (1)$$

Where θ is the zenith angle. At angle θ = 48.2°, the air mass coefficient is AM1.5 corresponds to 1000 W/m² power density. AM1.5 is commonly used to characterize the performance of PV or solar cells under standardized conditions [6].

Working principles of PV cells:

Solar cells are photo-electrical devices which converts part of the incident solar irradiance into electricity by using the so-called photovoltaic effect [7]. The cell is made from two materials which

form a junction with a bandgap energy (E_g). If the energy of incident photons (E_{ph}) is lower than E_g, light won't be absorbed, which is referred to as non-absorption losses [7]. If E_{ph} is higher than E_g, the light will be absorbed and generate electron-hole pairs. which are separated and excited to different-energy states. then the separated charge carriers will diffuse through the cell and are collected at its electrodes (terminals). Which cause the current to flow in order to cancel the created potential [8]. the excess energy from absorbed photons will be released in form of heat in a process called *thermalization* [9]. Moreover, before charge carriers are collected, recombination of electrons and holes can occur due to short diffusion lengths L_n, defects etc. [8]. Additionally, solar cells suffer from ohmic losses coming from material resistivity as well as optical losses caused by reflection, refraction, and shadowing [9]. All these losses combined limit the PCE of a solar cell. Thus, producing sufficient solar cells requires careful designing and fabrications processes that take care of all losses.

In order to measure the performance of a solar cell at certain conditions, several characteristic parameters need to be measured at these conditions. The first parameter is called **open circuit voltage (V_{oc}),** which represent the maximum measured voltage across the solar cell's electrodes when no load is applied on the cell [10]. The second parameter is the **short-circuit current density (J_{sc})**, which is the current density measured by short circuiting the terminals of the solar cell under specific conditions and normalized on the cell's area [8]. Third is the **maximum power point (MPP**) which is the working point when electrical generated power in a solar cell is maximum under the given illumination conditions [11]. The corresponding generated current & voltage at MPP are I_{mpp} & V_{mpp} respectively. Finally, the **filling factor (FF)** is the ratio between I_{mpp} x V_{mpp} rectangle and the I_{SC} x V_{OC} rectangle, as shown in Figure 1, FF is calculated as in following equation [10]:

$$FF = \frac{J_{mpp} x V_{mpp}}{J_{SC} x V_{OC}} \quad (2)$$

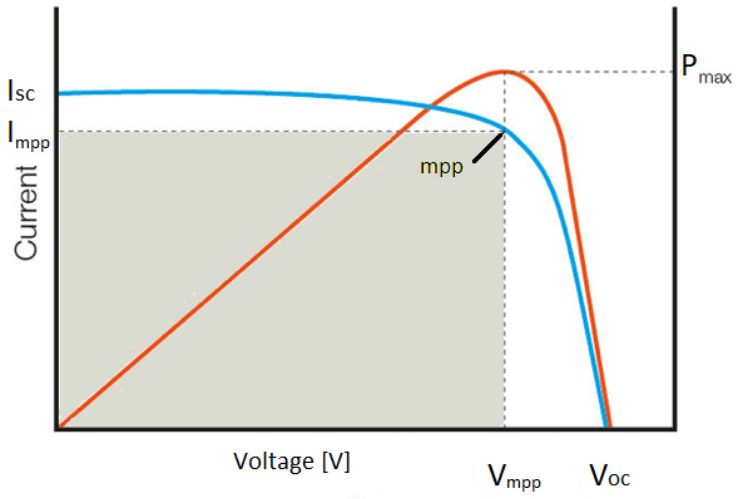

Figure 1 A typical diagram of IJ_V curve for illuminated solar cell. The figure also displays the external cell parameters and how they are related to each other.

The aforementioned parameters can be used to calculate the power efficiency (η) which is the ratio of maximum generated electrical power to the input solar power (P_{in}). The efficiency is then

$$\eta = \frac{J_{mpp} x V_{mpp}}{P_{in}} \quad (3)$$

To make comparison easier between different solar cells or modules, efficiencies and other parameters are normally measured under standard test conditions (STC) at AM1.5G, P_{in} = 1000W/m², and cell temperature of 25°C [12].

1.3 Classifications of PV technology

Solar cells can have different composing materials, designs and structures. Based on these variations and historical developments, three main generations have emerged as follow:

First generation of PV technology refers to wafer-based cells which are mainly mono/multi crystalline silicon (c-Si) cells in a single p–n junction (SJ p-n) configuration with indirect bandgap of E_g ~1.12 eV. c-Si cells are featured by having broad spectral range of light absorption as well as their high carrier mobilities beside the abundance of silicon, which made them one of the earliest forms to be used commercially and consequently the most common used in industry today [13]. To date, the highest PCE of a SJ c-Si solar cells is coming out of Kaneka's Interdigitated Back Contact (IBC) c-Si solar cell which has a record of 26.7% [14]. The IBC cell uses a double back contact at the rear of the cell to collect the generated current. Where the whole emitter is located at the rear and base structure in inter-digitated pattern. This allows the cell to minimize shading losses which leads to higher (photogenerated) or short circuit current. Furthermore, the existence of co-planar cell's interconnection reduces the module fabrication complexity by allowing thinner and larger wafers to be used [15]. In addition, the elimination of contact from the front of the cell gives the cell a uniform black appearance and allows for bigger and larger contacts to be used at the rear which will reduce resistive losses [16]. Some of the IBC cells drawbacks are their theoretical efficiency limit as well as the expensive and energy intensive manufacturing of crystalline silicon [17]. Figure 2 shows a schematic side cross section of a typical IBC solar cell with a correspondent rear cross section showing the contacts busbars.

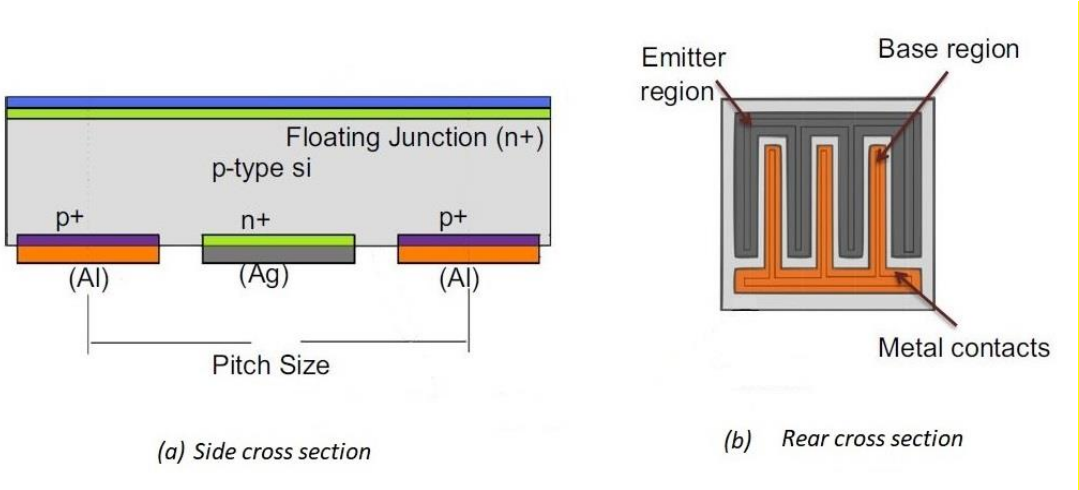

Figure 2 A typical schematic IBC cross-section (a) side cross section showing emitter contact, base contact and pitch (b) Correspondent rear surface showing interdigitated emitter-base busbar pattern [16].

From Figure 2, it is seen that the emitter & base busbars have different widths and areas. This is due to design optimization since emitter has to collect holes which are different in size and mobility from electrons which are collected by the base [16].

To utilize the generated charge carriers more efficiently, passivation is necessary in IBC cells. Where a layer/s of material are used to suppress recombination of charge carriers near interfaces. And facilitating the transport of one type of charge carrier toward certain metal contact. Example of such materials is intrinsic hydrogenated amorphous silicon (a-Si:H) which improves the vertical conductivity and provide carrier selectivity. Another example of passivating material is the use of polysilicon in tunnel oxide passivated contact (TOPCon), where a thin layer of tunneling oxide such SiO2 is deposited on n+ and p+ polysilicon layers forming a selective emitter and base contacts respectively [18]. Based on the used approach, passivation can reduce the recombination velocity and thus the losses at interfaces. Or it creates front and back surface fields which facilitate the transport and separation of carriers. Or it exploits tunneling effect where one type of carriers passes to the contact while the other is blocked. Which will result in higher V_{OC} in the IBC cell [19].

Although IBC solar cells have several advantages, but they still suffer from few challenges:

- low FF compared to conventional direct contact Si cell.
- high series resistance due to rear emitter.
- The manufacturing process complexity leads to significantly higher production cost.
- The need for higher material quality (high lifetime wafer = c-Si > wafer thickness, so that the carriers can travel from the surface to the back contact, thus thinner wafer is also needed) [16].

While several improvements can be made to tackle these challenges which will be considered in this project by:

- introducing intrinsic buffer layers for surface passivation which reduces surface recombination
- Optimizing the back geometry (pitch, ratio) which minimize series resistance [20]. The IBC structure requires fine pitch to be able to collect charge carriers, where the pitch is the distance from one middle of contact finger to the middle of the next finger with the same polarity. The finer the pitch the more carriers can be collected.

The second-generation of PV is the thin film (TF) PV technology that uses thin absorbing layers which ranges from a few microns to a few nanometers in thickness and deposited onto inexpensive substrates such as metals or glass [21]. Their significant small thickness gives them the advantages of being more flexible, transparent, and cheaper than traditional silicon cells. However, TF cells low efficiency stayed a challenge from industrial perspective for many years [22]. Several types of TF solar cells have improved their efficiency in the last years such as cadmium telluride (CdTe) with 21.5% PCE record, copper indium gallium diselenide (CIGS) with 21.7% PCE record [23] [24]. Which put them back on the track of competition. In particular, one type of TF technology has outperformed other technologies in a short time span and that is the *Perovskite* single junction (SJ) TF cell. During the last decade, its efficiency has improved from PCE of 3.5 % to 25.5 % in 2020, which placed it as one of the fastest growing PV technologies so far [25].

Perovskite solar cells (PSCs) are made from hybrid organic-inorganic lead or tin halide-based material as absorbing layer in an orthorhombic crystal structure with a structure formula of ABX_3, where A & B represent cations and X is anion as positions in the crystal lattice [26]. These materials have high absorption coefficient which enables them to absorb the solar spectrum within very small thickness. Further, they have long carrier lifetime which leads to long charge carrier diffusion length as well as high carrier mobilities. They also hold suitable properties to be fabricated as TF solar devices at low costs [27]. In addition, altering the A, B and X elements can create a wide range of options to control bandgap energy as well as electron affinity which makes worthy options for solar tandem devices.

However, they suffer from toxicity and instability by humidity & temperature. Thus, encapsulation and coatings are needed which are promising approaches to contain their toxicity and improve their stability [28].

PSCs are made in mesoporous structure (where mesoporous medium penetrates the perovskite absorber) or planar structure (where it is formed from separate stacked layers consisting of the hole transport layer (HTL), perovskite absorber layer, and the electron transport layer (ETL)) [29]. Furthermore, the planer structure can be structured in two configurations based on polarity, the p-i-n and n-i-p configuration. Where the letter's "p", "n" & "i" represent the order of the "HTL", "ETL" and the Perovskite layer respectively. When the HTL material is firstly deposited on the substrate, the configuration is commonly called inverted planar or p-i-n. In contrast, when the first material that is deposited on the substrate is ETL, it is called regular planar or n-i-p PSC. A schematic of these configurations is shown in Figure 3:

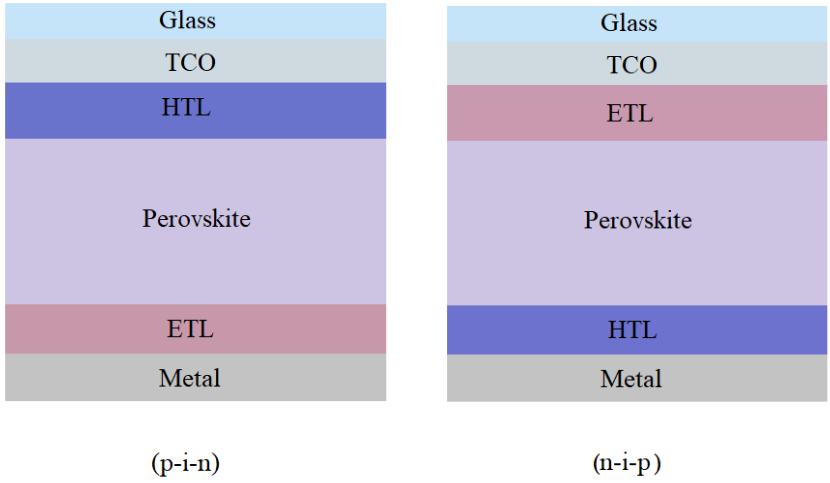

Figure 3 Schematic of planer configurations of PSC (p-i-n) on left and (n-i-p) on right.

Typically, n-i-p structure is best used for SJ PSC applications while p-i-n structure is favored in tandem devices because of its suitable optical properties to the tandem structure [30]. It is important to choose ETL and HTL from materials that are aligned in their bandgap energy with the perovskite so that the charge carriers can be separated and transported to the intended terminals. Usually, low Perovskite bandgap energy material is desired for SJ applications, while high bandgap energy is desired for tandem devices. Furthermore, both electron transporting layer (ETL) and holes transporting layer (HTL) need to be adjusted in accordance with the Perovskite properties in order to optimize the efficiency [30].

The third generation PV technology refers to high power converting efficiency (PCE) solar cells that use approaches such spectral up/down conversion, light concentration and/or multijunction (MJ) cells to exceed the single junction Shockley–Queisser (SQ) limit. More information about third generation PV cells can be found in reference [8]. The focus of this project will be limited to MJ solar cells, in particular, dual tandem perovskite/c-Si devices. Next section will discuss this type of cells in more details.

1.4 Perovskite/c-Si tandem solar cells

The typical solar cell is made up of a single c-Si (p-n) junction that has a maximum theoretical PCE of ~29% according to SQ limit with Auger recombination restricted [31]. This limit is due to different internal loss mechanisms which are blackbody radiation, recombination processes, spectrum losses, and impedance matching [32]. On the other hand, multi-junction (MJ) or tandem solar cells are made up from different absorbers forming multiple p–n junctions with different bandgaps, where each absorber allows absorption from certain part of the incident spectrum. This result in a higher maximum theoretical PCE that can go as high as 68.7% when the number of junctions is infinite [33]. Thus, MJ or tandem cells offer excellent alternative to replace the SJ PV technologies that many of them are approaching their theoretical limit.

The simplest structure of MJ cells is a double junction (DJ) solar cell made from two SJ cells above each other. The top cell, usually, has higher bandgap energy (E_g) that is optimized for the absorption of short wavelength photons. While the bottom cell has lower E_g to optimize absorption of the long wavelength photons. This reduces both radiative and thermalization losses, which consequently lead to a solar tandem device that can surpass a PCE of 30% [34]. An example of such DJ tandem devices is the Perovskite/c-Si tandem. This type of tandem devices has at the top a perovskite SJ thin film solar cell based on organic-inorganic metal-halide material as the absorbing layer. Which is paired with SJ c-Si wafer bottom cell. As it was discussed before, both these SJ cells are well-researched in the field of PV technology and have already achieved high PCE [35] [36]. The emergence of PSC/c-Si tandem is promising because of the abundance of both silicon and Perovskite material as well as cheaper fabrication cost compared to III-V tandem devices. Furthermore, PSCs have high tunable bandgap energy varying from 1.5 to 2.0 eV [37]. Which makes them attractive as top cell candidate, while the indirect bandgap of c-Si is most suitable as bottom cell [38].

Perovskite sub-cell can be staked on the top of c-Si sub-cell mechanically or monolithically in the tandem structure in different configurations based on the number and the positions of terminals (contacts). the most common configurations are two terminals (2T), four terminals (4T), and three terminals (3T) [39]. Next sub-sections will describe each configuration with the focus on comparing between them as well as to highlight their common advantages/disadvantages.

1.4.1 2T configuration

in this layout, the two sub-cells of the tandem device are brought together monolithically without mechanical separation. This result in a series connection of both sub-cells.

Figure 4 describes the schematic cross section of 2T tandem device, we can see from the figure that the higher energy photons are absorbed by the perovskite layer generating electron-hole pairs. Electrons are transported by the ETL and collected by the front top silver terminal, while the holes are transferred to the recombination layer by HTL. On the other hand, low energy photons are absorbed by c-Si layer generating electron-holes pairs. Where holes are collected at the rear back silver contact while the electrons recombine with the holes produced from perovskite layer at the recombination junction (RJ).

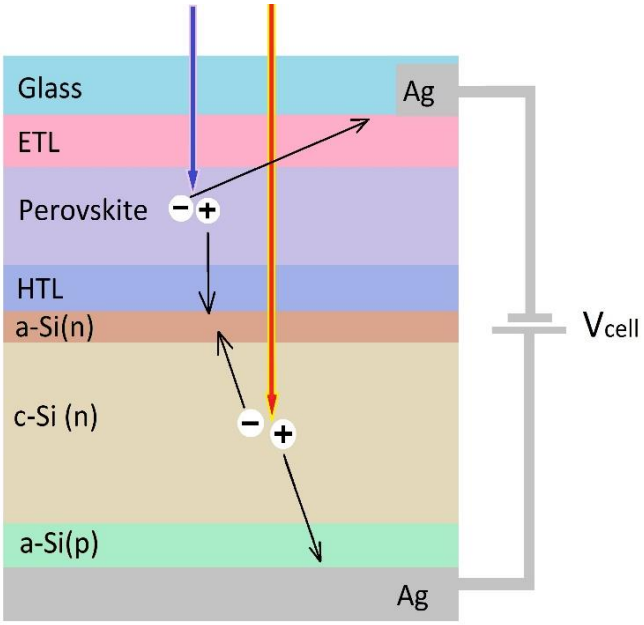

Figure 4 Schematic cross section of 2T PSC/c-Si tandem device (not to scale).

The generated current of the tandem device is limited by the sub-cell that produces less electron-holes pairs while the voltage of the tandem is the sum of the potential produced by both sub-cells [39]. Current density reduction then lowers the PCE of a 2T tandem. To achieve higher PCE, current matching between the top and lower sub-cell is needed. This additional step is considered the main disadvantage of 2T layout since it constrains the material choices and requires careful current optimization [40]. While the main advantage of 2T layout is the simplicity of the design which doesn't need mechanical separation of the two sub-cells or any additional transparent conductive layers between them that could cause extra parasitic losses. Thus, 2T configuration reduces the costs of fabrication on a modular level [41].

In 2019, a new record of 2T perovskite/c-Si tandem device was achieved with PCE of 26.7% [42]. Followed by another record in 2022 exceeding the 28.7% by Hanwha Q Cells [43]. And again in 2022, the 30% parity was surpassed by EPFL and CSEM achieving a world record of 31.25 % for the first time for perovskite on silicon tandem cells [44].

1.4.2 4T configuration

In a 4T layout, the two solar sub-cells are separated mechanically, and the charge carriers are collected separately at different 4 terminals. The result is two staked electrical junctions with sperate circuitry that allows the generated power from each sub-cell to sum up collectively [39].

Figure 5 describes the schematic cross section of 4T device, we can see from the figure that the higher energy photons are absorbed by the perovskite layer and collected separately from bottom cell by two terminals. On the other hand, the lower energy photons are absorbed by c-Si layer and also collected apart from the top cell by another two different terminals. Thus, each sub-cell operates individually. Which make the current and voltage that is produced by one cell causes no influence on the other sub-cell. Thus, there is no need for current matching between them as it is needed in 2T configuration [40].

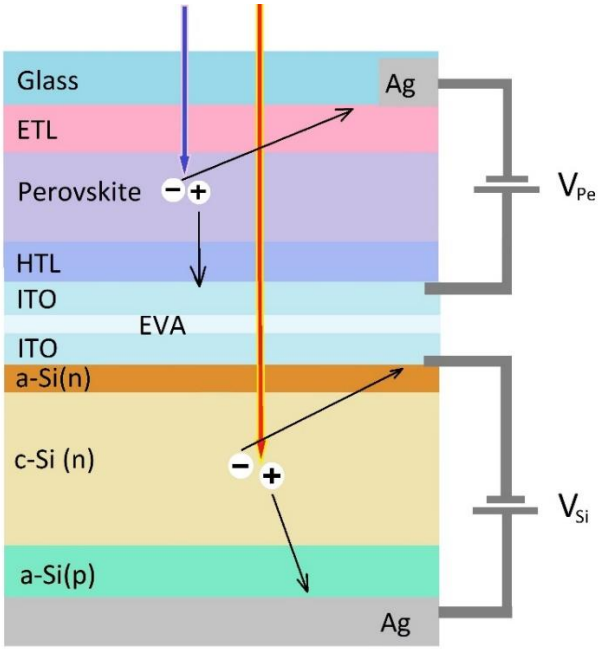

Figure 5 Schematic cross section 4T Perovskite/c-Si tandem device (not to scale).

However, 4T layout requires additional two transparent conductive layers to collect charge carriers from the back of the top sub-cell and the front of the bottom sub-cell as well as one additional isolation layer between the sub-cells [45]. Therefore, generated current as well as PCE will suffer from reduction coming from the additional reflection and absorption losses in these layers [46]. Furthermore, these layers add extra level of complexity to the design and fabrication of the tandem device [40].

In 2020, a record with 28.2% PCE was already achieved in lab environment for 4T configuration [47]. A newer record has been announced by the German research institute Helmholtz-Zentrum Berlin (HZB) surpassing 29.8% [48]. The higher efficiency and the wider range of bandgap selection made 4T perovskite/c-Si tandem the most widely used approach in research among Perovskite/c-Si tandems. And it is expected to exceed the 30% PCE parity very soon [49]. On the other hand, 2T is more preferred approach for industry since it simpler and cheaper to produce [39]. However, a 3T configuration could be a breakthrough in the solar tandem technology since it has the potential to compete with both 2T & 4T approaches.

1.4.3 3T configuration

In the 3T layout as in the 2T layout, the two sub-cells are staked monolithically on a single substrate. The charge carriers are collected at the top and rear of the tandem device. However, a third electrical terminal is added either at the rear of the bottom sub-cell or between the two sub-cells to overcome the current mist-match. This contact is shared by both sub-cells [45]. The result is an integrated architecture that doesn't require mechanical separation of sub-cells, neither it requires current matching optimization. At the same time, it allows both sub-cells to operate independently at their MPP conditions similar to 4T device [40]. Which makes the device's energy yield more stable against spectral variation and has less parasitic absorption [50]. Therefore, 3T layout in tandem devices carries optimistic promises to surpass the PCE achieved in both 2T & 4T, likewise to reduce fabrication costs.

Figure 6 shows a schematic cross section of a 3T tandem device with one terminal at the front of top cell and two contacts at the rear of bottom cell i.e., with an IBC bottom cell.

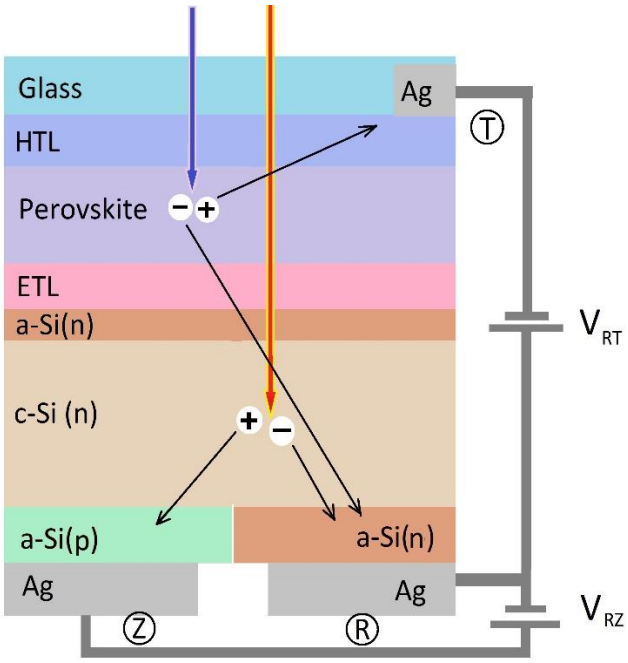

Figure 6 Schematic cross section of 3T Perovskite/c-Si tandem device (not to scale).

As it is seen in Figure 6, the high energy photons are absorbed by the Perovskite layer while the low energy photons are absorbed by the c-Si layer. The energy bandgaps in each layer of the tandem are chosen in a way to facilitate collecting electrons (holes) from both absorbers at one rear terminal while holes (electrons) generated by Perovskite layer are collected at the front top contact and those generated by c-Si are collected at the second rear contact [45].

Although it is not intensively researched as 2T and 4T, the 3T architecture can be designed in different configurations with different levels of complexity which makes it attractive research topic in the field of PV technology. It can combine the advantages of both 2T & 4T configuration and overcomes their disadvantages [51]. More about the current research of 3T tandems is discussed in the next section.

1.5 State of art of 3T Perovskite/IBC Tandem cells

The current state of art of 3T perovskite/c-Si tandem device is based on a few but fruitful research. So far, two main 3T configurations were used to realize a 3TT device. Either by introducing the third terminal in the middle between the sub-cells or by adding it to the rear of bottom sub-cell [50]. One of the recent experiments on the first approach is done by *Park et al in 2019,* which resulted in a stable physical tandem cell with PCE of 23.1% that could maintain 97% of its initial efficiency for more than 100 days. The third terminal in this tandem was established between the sub-cells as a thin transparent ITO conduction layer that serves also as a recombination layer on the top of a flat-surface c-Si substrate [52]. The drawback of this approach is the high parasitic absorption when the middle (contact) layer is thicker than 100nm which reduces the performance of the bottom sub-cell significantly [50].

On the other hand, the second 3T configuration (PSC on top of c-Si IBC cell) has gained more interest in research. This approach was developed over years starting from the concept of a 3T Si cell with back contact emitter that was first introduced by *Chiang et al.* in 1978 to make use of the transistor effect in such cells [53]. Later on in 2000, *Nagashima et al.* has proposed a new design where the top cell was AlGaAs and the bottom cell was based on either Si or Ge. The basic principle of this device is to allow carrier selectivity by altering the doping to produce barriers that facilitate diffusion of one carrier type (electrons or holes) in certain directions while the other type is blocked in those directions. Which leads to collecting carriers at each terminal selectively with minimal recombination probability [54]. The model of Nagashima has opened the door for researchers to further exploit it with new materials with some enhancement on the original design. One of the most distinguished works in this regard is the work of *Warren et al.* where they used Sentaurus-TCAD simulation package to investigate the performance of the 3T III-V/c-Si tandem device over a range of different conditions to optimize power extraction from the device [54]. Furthermore, they were the first to experimentally build a 3T tandem device of GaInP cell on top of c-Si POLO IBC cell with PCE of 27.3%, where (POLO) stands for carrier-selective polysilicon on oxide (POLO) [55]. In 2020, *Warren et al.* also introduced a taxonomy for Three-Terminal Tandem (3TT). The created taxonomy has cleared a lot of confusion and differences of used terminologies when it comes to 3TT device. More details about the taxonomy can be found in reference [46].

Further, in 2019, *R. Santbergen et al.* produced one of the first 3TT Perovskite/ c-Si models using the carrier selective concept of *Nagashima et al.* [51]. The model had n-type Silicon Heterojunction IBC bottom cell passivated by hydrogenated amorphous silicon (a-Si:H). while the top cell is a Perovskite cell in n-i-p or p-i-n order. This result in two different models with the top cell having a similar or inverted polarity from the bottom cell. Which allowed to compare the performance of these two different circuitries [51]. The model was realized using the software GenPro4 for optical simulation and ASA or Quokka software for electrical simulations. The results showed that organizing the junctions in np-np order has obtained a bit higher efficiency than a pn-np order. In addition, higher power yield can be achieved when using thicker perovskite layers. But the most important finding of this pioneer work was that this 3TT configuration has the potential to surpass 32% PCE [51]. Similarly, the group of *Tockhorn et al* in 2020 has considered the same 3TT device layout with slight changes. The simulations were based on drift-diffusion of charge carriers and continuity equation using the software package Sentaurus TCAD [50]. The result has demonstrated that potential of 27% PCE can be obtained. Further, they were able to fabricate, physically, a tandem device that reached 17.1% PCE under MPP conditions [50]. Which confirmed that a high efficiency 3TT device using this configuration is feasible.

Furthermore, *Connolly et al.* took the 3T Perovskite/ n-type c-Si IBC a step further by adding a highly doped perovskite layer on top of the perovskite absorber to enhance selectivity of terminals by creating a selective band offset barrier (SBOB). Which allows each sub cell to operate independently with less recombination and thermal losses [56]. This model predicts a high potential of exceeding 35% PCE [57].

3T perovskite/c-Si IBC tandem cells have not only the potential of higher efficiency but also higher energy yields (EY). According to the work of *Gota et al* in comparing 3T with 4T & 2T tandem architectures, the 3T layout has demonstrated almost 6% higher generated photocurrent density (J_{ph}), under all climate conditions compared to 4T layout. Which therefore resulted in extra ~3% to 9% EY [45]. Additionally, compared to 2T layout, a 3T tandem device outperformed the 2T tandem device against spectral variations and showed more robustness caused by reduced mismatch losses in 3TT device [45].

The work of researchers has given the platform for further research to be conducted on different material choices, approach, and/or structures of 3TT devices. But yet, only few materials, structures, or approaches were investigated by other researchers. For example, using advanced 2-D modeling is still limited. As well, investigating 3TT Perovskite on top of POLO IBC cell is uncommon. Furthermore, the design of the IBC bottom cell which is used in 3TT device is the same design of SJ IBC cell, which could not be optimum for 3TT device performance. Thus, re-designing the IBC for optimum performance is a necessity for tandem device. These issues will be the focus of this project.

1.6 Objectives, research question and Outline of Thesis

Despite the major progress in the field of 3T Perovskite/Si tandem solar cells, yet it is still practically challenging to design and fabricate stable devices that bring 30% PCE's goal to reality. Achieving this goal is important to prove that 3TT perovskite/Si device is capable of breaking the SQ limit of SJ Si cells as well as competing with other tandem configurations such 2TT and 4TT devices. The challenge in achieving that goal is due to the difficulty in understanding the nature of optical-electrical coupling between the component layers and sub-cells, as well as the complexity of design of such high efficiency tandem devices. Moreover, the integration between module and tandem cells is intricately dependent on their architecture which needs careful testing and study. Tackling these challenges is of great importance since it is a bottle neck problem in the future of 3T perovskite/c-Si tandem cells. And due to these challenges and the complexity of fabrication of 3TT devices, more research on them is carried by modeling the device with the help of different simulation software's. Which saves time and costs. In addition, simulation helps searching and researching new materials and options which are experimentally almost impossible to do. It also speeds up development of solar technology by conducting many simulations simultaneously.

However, since most of research which is done on 3T perovskite/c-Si tandem cells involves a bottom IBC cell, a two-dimensional (2-D) modelling of tandem device is required to reflect accurate realistic results. Moreover, the need to provide rich information about the charge carriers requires advance 2-D model that produce higher simulation precision of opto-electrical properties between the layers of the tandem device. Because of these reasons, this project will be focused on 2-D opto-electrical modeling to investigate and enhance the performance of 3TT PSC/c-Si IBC device.

Furthermore, the perovskite top cell as well as the c-Si IBC bottom cell need to be investigated and re-designed for optimum 3TT device's performance. Therefore, the main research question and aims of this master research project are:

Can a 3TT PSC/c-Si IBC tandem device exceed the single junction limit and compete with 2TT & 4TT devices?

And can we improve the design of the tandem cell to increase efficiency of the device?

These research questions lead to the following objectives:

- To propose and design an advance stable 2-D 3T Perovskite/c-Si IBC tandem device's model capable of reaching high PCE.
- To validate the model and compare it with SJ reference cells as well as with another tandem configuration.
- Redesign parameters of perovskite top cell (layer's thickness) and the architecture of c-Si IBC bottom cell (pitch and emitter/base ratio) to optimize the proposed 3TT model.

To achieve these goals, a 2-D simulation model template needs to be built for the mentioned tandem device with the help of the commercial software package Sentaurus TCAD. Further, the created model template must be tested and validated with reference data. Then, the validated model can be used to conduct a comparison between the proposed 3TT device and an identical 4TT device to examine the compactivity of the model. Furthermore, the 3TT model is used to investigate and improve the design parameters of the tandem device in general and the design of c-Si IBC bottom cell in particular. The improved model will deliver an estimation of the realistic potential of the 3TT proposed model and enable us to assist future research recommendations

Outlines:

This report is put forward in the following structure. Chapter 2 presents the selected device structure to be simulated, the physical working principles of the device and the opto-electrical simulation setups. In chapter 3, the initial opto-electrical simulations results of the 3TT template are presented, explained, and validated. Further, the chapter compare the simulated performance between our proposed 3TT device and an equivalent 4TT device. Chapter 4 discusses different approaches to optimize the 3TT device. This includes optimizing the perovskite layer thickness, comparing the pitch behavior between SJ IBC pitch and 3T IBC and redesigning the IBC cell to optimally work for a 3TT device as well as optimizing the emitter/base ratio. Finally, Chapter 5 draws the final conclusions of the project. Furthermore, this chapter will provide suggestions on how to enhance the results as well as recommendations for further research projects.

2 3TT Device Structure and Simulation's Setups

This chapter aims to propose and design an advance stable 2-D 3T Perovskite/c-Si IBC tandem device's model capable of reaching high PCE. And to explain the methodology and setups to simulate that model. Section 2.1 deals with the 3TT device architecture and components. Then, the device physical working principles are explained in section 2.2. After that, section 2.3 describes the basic simulation's principles and the flow mechanism of simulation. Moreover, the section provides a brief summary of the used TCAD Sentaurus tools and their roles & dependency in the simulation process as well as enlisting the physical models and parameters that are used for in Sentaurus. Section 2.4. explains the optical simulation approach and enlists the necessary parameters for it. Finally, section 2.6 describes the electrical simulation approach.

2.1 Device design and structure

As it was discussed in chapter one, the main objectives of this project are to simulate and optimize a 3TT Perovskite/c-Si IBC device based on advance 2-D modeling. But to be able to build such a model and optimize it, a basic device structure needs first to be proposed which agrees with the 3TT device physical working principles. Since there are different 3TT configurations, the tendency of this project goes for a top perovskite cell in p-i-n configuration on a n-type c-Si IBC bottom cell with polysilicon carrier selective passivating contacts.

The reason for choosing this type of 3TT configuration is for their excellence predicted PCE as reported by *Tockhorn et al. and Santbergen et al.* [50] [49]. In addition, they don't need a tunneling recombination junctions between the two sub-cells to activate the third terminal which reduces the complexity of the flow mechanism of charge carriers. Moreover, TOPcon (Tunnel Oxide Passivated Contact) SJ IBC have high efficiency and promising accurate carrier's selectivity when using poly-Si(n+)/poly-Si(p+)/SiOx as tunnel junctions [58]. This allows to eliminate shading losses and reduce contact resistance by high carriers' selectivity. On the other hand, choosing Perovskite top cell in a p-i-n configuration is to create a reverse junction with the n-type IBC so that both sub-cells operate independently by the natural diffusion of charges without the need for a tunnel recombination junction between the two sub-cells to select the carriers.

The schematic diagram of the proposed 3TT device structure with a p-i-n PSC on top of poly-Si passivated contacts (TOPcon) IBC cell can be seen in Figure 7, Figure 7 displays the charge carrier's paths and extractions at contacts. The materials and functions of layers also can be recognized. The correspondent parameters of these materials and their physical roles are listed below. Which are used in our simulation to resemble the actual behavior of proposed 3TT device. The layers are ordered from top to bottom as follow:

- **Anti-reflecting coating (ARC) layer**
  This layer helps reducing reflections and let more photons to be utilized. Which leads to higher optical generation. ARC can be a single layer or a stack of several layers to improve light management. But it is selected to be one layer in this project to reduce complexity and time of simulations. For optical simulation, SiO_2 was used as ARC layer with a thickness of 70 nm.

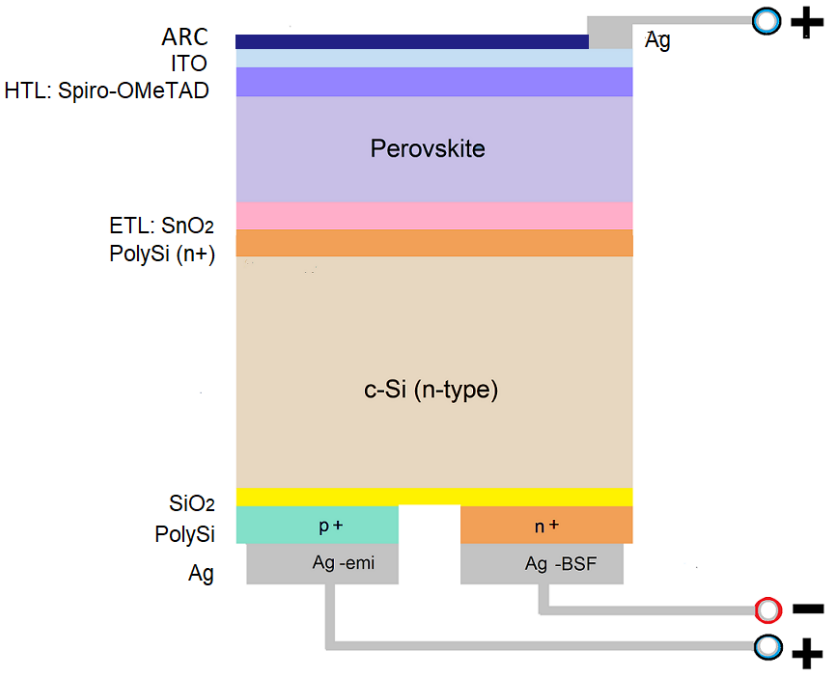

Figure 7 Schematic (not to scale) of the 3TT layer's stack that is used in the Sentaurus TCAD simulation.

- **Ag top metal contact**
  The top metal contact is meant to collect the charge carriers from the top terminal. The material was chosen to be silver for their high conductivity and chemical stability.
- **ITO** works as a TCO layer, (40 nm)
  Indium tin oxide (ITO) is used as a transparent conductive oxide due to the poor conductivity of the HTL layer. TCO layer on the top of HTL will facilitates collecting the charge carriers and acts as a contact that helps generated holes in the top cell to reach the front metal contact. In the basic simulation, this layer will be omitted to detect the performance of the tandem device without the help of TCO layer. Then it is added to observe how much improvement this layer has added to the performance [40].
- **Spiro-OMeTAD** as HTL, (40 nm)
  This layer Serves as hole transporting layer which facilitates the flow of holes from the perovskite absorbing layer to the TCO layer with minimal recombination losses. At the same time, it acts as a barrier to block transferring electrons to the front top contact [40]. This layer should have high hole mobility and low electron affinity to serve its purpose. For this project, Spiro-OMeTAD was chosen. It can work as HTL layer in both n-i-p & p-i-n PSC configurations and it has suitable thermal and optical properties [59]. The disadvantages of this material are its high absorption and reflection in the short wavelengths range [40]. Which requires the thickness of the layer to be small and carefully tuned to boost power conversion. For this work 40-20 nm was found to be the most effective thickness for Spiro-OMeTAD.
- **Perovskite**:
  Since this project is attempting to create a basic model for 3TT devices, the absorbing material for top cell is chosen to be the standard form of Perovskite which is archetypal methylammonium lead iodide ($CH_3NH_3PbI_3$) or ($MAPbI_3$). This type of Perovskite has relatively shorter diffusion length compared with other mixed halide perovskite's materials, which narrow the window of efficient

thickness range [60]. That is why the performance of 3TT device will be investigated under different thicknesses of perovskite layer to optimize it for highest performance. The initial basic model will use a 500 nm thick layer of perovskite. The same thickness is also used in reference SJ PSC.

- **SnO_2** Tin (IV) Oxide (40 nm)
  Serves as an electron transporting layer (ETL) to facilitate the flow of electrons from the perovskite absorbing layer toward the bottom cell. For this project, SnO_2 is used as ETL which reduces parasitic loss formed by the HTL. According to literatures, high efficiency PSCs usually use SnO2 or TiO_2 as ETL [30]. The disadvantage of TiO_2 is the high temperature of its processing which could damage the IBC layers during deposition and annealing processes. And the relatively low electron mobility which requires it to be in thin thicknesses to serve as effective ETL [61]. That is why TiO2 was avoided and SnO2 was used instead. Which is normally prepared and annealed at lower temperature ~ 120 °C that doesn't cause damage or shift in properties for lower layers [62]. Furthermore, SnO2 has anti-reflection properties, higher stability, more ability to extract electrons than TiO_2, and better band alignment with perovskite that produces less hysteresis [40]. For this project, a 40 nm is considered effective thickness For SnO_2 layer.
- **poly-Si(n+)** (20 – 50 nm)
  The use of this lightly doped n-type polysilicon layer at the front surface of the IBC bottom cell will create front surface field (FSF) passivating layer which reduces surface recombination by preventing the minority carriers from recombining [63]. Moreover, the formed electric field creates a tendency for the electrons generated in silicon bulk to not penetrate toward the perovskite top cell and improve the lateral current by decreasing the resistivity in the base [63]. Thus, it helps preventing electrons and holes from premature recombination and enhances the carrier selectivity concept of the 3TT device.
- **c-Si** (n-type) absorbing material for bottom cell (260 µm)
  The bottom cell absorber is made of n-type c-Si wafer of 260 µm thick. The layer serves as low energy light's absorber which absorbs the rest of spectrum that passes from the top cell. The c-Si bulk material has indirect band gap with E_g =1.12 eV which makes it convenient as a bottom absorber. However, since the bottom cell in the 3TT device need to be an IBC cell, the Si wafer has to be in a pure crystalline form in order to deliver high efficiency [17].
- **SiO_x** Silicon dioxide (ultra-thin tunnel layer) (1.2 nm)
  The purpose of this layers is to enhance selective tunneling probability of majority carriers that pass through either the emitter or base respectively and to block minority carriers from passing through [58]. This is made possible using ultra-thin layer of SiO_x that creates a potential energy barrier which allows carriers to tunnel selectively based on the doping concentration of the polysilicon layers beneath the SiO_x layer [58]. In addition, the existence of SiO_X at the back of IBC plays also important role as passivating layer that reduces the number of minority charge carriers at the rear surface [64].
- **Poly-Si(n+)** and **poly-Si(p+)**
  Highly doped n-&p-type polysilicon (poly-Si(n+), poly-Si(p+)) layers which function as carrier selective passivating contacts where the poly-Si(n+) layer has average thickness about (20 nm) covering the base contact and acts as a back surface field (BSF) or base that help collecting electrons that tunnels from the SiO_x layer. While the poly-Si(p+) layer covers the emitter contact with average thickness about (20 nm). It serves as an emitter which helps collecting selectively the holes that tunnels from the SiO_x layer [58]. Both layers are separated by a gap of 10 µm which prevents contacts and pre-mature recombination from occurring in the region where the two

layers meet. Moreover, the stack of Poly-Si(n+/p+)/SiO_X acts as a shallow diffused region that increases the tunnel current [64].

It is worth mentioning that the selectivity of tunneled charge carriers depends on several factors, which are the doping concentration in the polysilicon contacts, and the thickness of the SiOx layer. Where active doping and a layer of SiO_x thinner than 2 nm are pre-requirements to make almost perfect tunneling of the majority carriers and zero tunneling of minority carriers in each contact respectively [58].

- **Ag rear metal contacts** (1-5 µm)

  Finally, the back metal contacts are made of silver. And the width is chosen in this project to be 80% of the width of the respective passivating polysilicon layer (i.e., 80% of emitter or base width). This allows for better coverage and lower the contact resistance losses.

2.2 Device working principle

As it was discussed in the previous section, 3TT device requires a delicate design and careful selection of layers to function properly. A brief description of the functionality of the layers was introduced. In this section, the working principles of the 3TT structure are further discussed with the focus on the alignment of the bandgap energies to result in a 3T configuration. Moreover, we distinguish between dark conditions and illumination conditions in the 3TT device.

2.2.1 Alignment of band gap energies of the layers

To build a robust working 3TT device structure, a careful alignment of bandgap energies is required in order to achieve the desired outcome. This is realized by selecting materials with bandgap energies and electron affinities to allow for spontaneous flow of charge carriers in the directions they are meant to have. Figure 8 below shows a sketch of the aligned stack of layers in the proposed 3TT device based on bandgap energies and affinities differences.

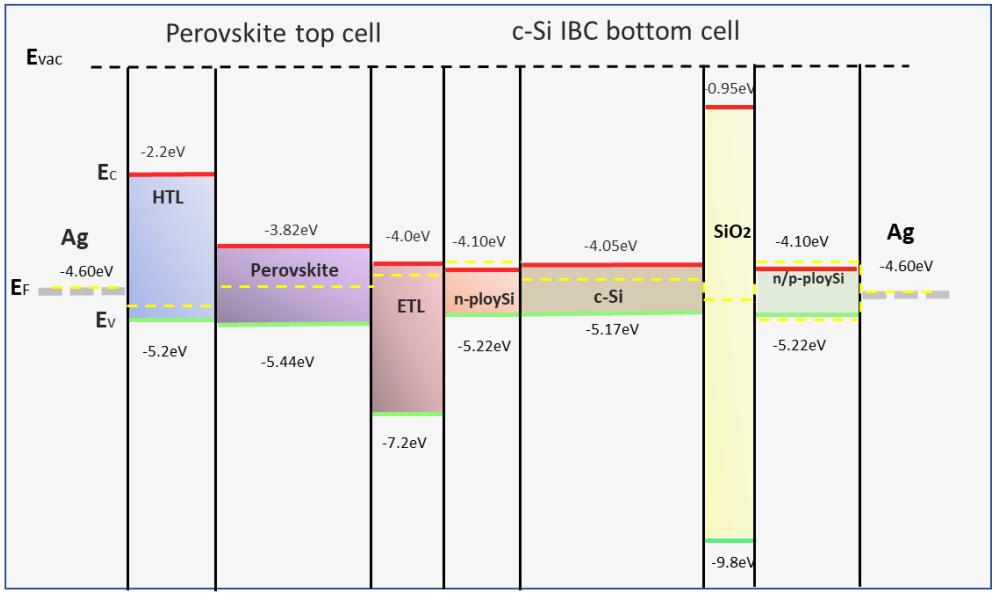

Figure 8 Bandgap alignment of 3TT device's layers.

From Figure 8 it is observed that the recombination junction between the top and bottom cells is selected from materials with electron affinities and band gaps that allows electrons which are

generated at the perovskite top cell to flow toward the bottom cell to the rear n-contact. On the other hand, holes which are generated at the top or bottom cells will face energy barriers that block them to intercross between the two cells. Thus, hole generated by the perovskite cell will be pushed toward the front top contact. And the holes generated by c-Si cell will be collected by the rear emitter through selective tunneling.

To fully understand the working mechanism of solar device, it is important to distinguish between two conditions that influence the band diagram and energy states of electrons and holes in the device. These conditions are dark conditions and Illuminated conditions.

The dark conditions are when solar cell is in a stable thermal equilibrium with no illumination, magnetic field, or mechanical stress [8]. Under these conditions, the fermi energy levels of each layer in the cell are matching and equal to E_{Fo}. Furthermore, the differences in the work functions between ETL, absorber layer, and HLT will form a build in voltage V_{bi}. This voltage is caused by the presence of electric fields on the boundaries between layers which move holes towards the HTL and electrons toward the ETL [8].

2.2.2 3TT under illumination

Illumination conditions are when light hits the absorber layer, and consequently generates electron-hole pairs. The generation process will disrupt the equilibrium status which was mentioned in dark conditions. Therefore, new fermi-levels for valance & conduction bands will form for holes and electrons respectively. The generation process will trigger different recombination processes which need to be reduced when designing the tandem device. This requires sufficient thicknesses and properties of each layer such as diffusion length, carrier lifetime and sufficient mobilities as well as light management to reduces recombination, optical, and electrical losses [8]. To do so, the parameters of layers in each sub-cell need to be adjusted carefully to keep flow of charges optimal.

The generated charge carriers by illumination must be extracted at the proper contacts selectively to generate efficient power. But since the 3TT device has two absorbers that generate carriers simultaneously. Each carrier type must be separated and extracted with minimal chances for recombination. The carrier generation and selection in the proposed PSC/c-Si IBC 3TT device configuration, can be tracked per absorber as follows:

Generation at top cell (perovskite): Here, electrons are optically generated at the perovskite absorbing layer then transported through the n-layers (TiO2/poly-Si(n+)/poly-Si(i)/c-Si/SiO_X/poly-Si(n+)) to be collected at the base rear contact (-). The stack of ETL & poly-Si(n+) layers facilitate electrons in the perovskite layer to diffuse to the bulk of c-Si and from there to tunnel to the BSF (base) contact with the help of SiO_X. While the holes generated in perovskite cannot pass to the bottom cell due to misalignment of fermi levels which caused by the lower edge of valance band in the ETL that forbids holes from passing to the direction of bottom cell. Thus, they are blocked by the potential of n-layers and forced to move to the front top silver contact through (Sipro-OMeTAD/ITO layers) and collected at the front top terminal.

Generation at bottom cell (poly-Si IBC): In this case, electrons which are optically generated in the n-type c-Si absorbing layer tend to pass through SiOx/poly-Si(n+) toward the rear base contact rather than to go upward perovskite top cell. This is because the ultra-thin layer of SiO_2 combined with poly-Si(n+) will act as selective tunneling layer which is almost perfect for electrons [65]. On the other hand, the generated holes in c-Si have tendency to be collected at rear emitter contact by tunnelling through SiOx/poly-Si(p+) since the SnO_2 layer will block holes from intercrossing in both sub-cells.

Therefore, the device will form a 3TT layout in P-n-n-P configuration that allows the base contact to collect the generated current in both top and bottom cells while the holes are collected locally by the emitter of the respective sub-cell.

After clarifying the working principle of our proposed 3TT device, the next step is to embed the layer's parameters and properties into the simulation setups so that the performance of the device can be observed. But to achieve that, the step-ups and methodology of simulation need to be clarified and a robust approach need to be taken.

2.3 Simulations description

After the device structure and working principle of the proposed 3TT device are put forward, a description of the used simulation software is necessary to help understanding the simulation setups and mechanism. This also introduces how the opto-electrical stimulation of 3TT are approached and gives a brief introduction of Sentaurus TCAD working principles and the workflow of Sentaurus tools.

Since the bottom cell in our 3TT model represents an IBC unit cell which asymmetric in two dimensions, this mean that modeling the 3TT tandem device in one dimension is not an option. Therefore, only 2-D or 3-D modeling can unveil the full behavior of the device. But since a unit cell in tandem device is periodically repeated in 2-D, a 3-D simulation would be less favorable because it is much more time consuming. Thus, modeling in this project will be carried out by 2-D simulations.

To simulate the 3TT device in 2-D sufficiently and accurately, it is necessary to pick a reliable software. The commercial Sentaurus TCAD software package by Sypnosis was chosen to execute the job. This software is selected because of its excellence in performing multi-dimensional device structure's simulations in the field of semi-conductors. Further, it has advanced physical models that covers the fields of optical physics, thermodynamics, quantum physics and electromagnetism [66].

Sentaurus TCAD uses the numerical finite element method FEM to solve partial differential equations in space and time domains for the selected physical models. The FEM is based on dividing the unit cell into mesh blocks (2-D or 3-D). then it solves the physical models for the (area, or volume) of each mesh block and its boundaries. Thus, FEM obtains approximation solutions and the accuracy of them depends on both the physical models used and the mesh resolution. Usually, finer mesh is applied nearby interfaces between layers because these areas represent significant changes in boundary conditions and consequently less steady flow of physical behavior [67].

For PV devices, modeling requires two types of simulations, optical, and electrical stimulations. Where the electrical simulations are dependent on the outputs of the optical ones. Figure 9 shows a flow chart of the logical approach used in this project to execute both optical and electrical modelling of the chosen 3TT device.

As it is shown in Figure 9, the first step is to collect all data that is necessary for optical and electrical simulations for the selected 3TT device configuration. This includes physical materials properties, geometrical parameters, ambient conditions, and any other implied conditions. Then these data are fed to various Sentaurus tools which have dependency order. These tools are managed together by Sentaurus workbench (SWB) which is a graphical user interface that allows editing, controlling, and running the tools in different scenarios as well as importing external software and integrating them with other internal tools [68].

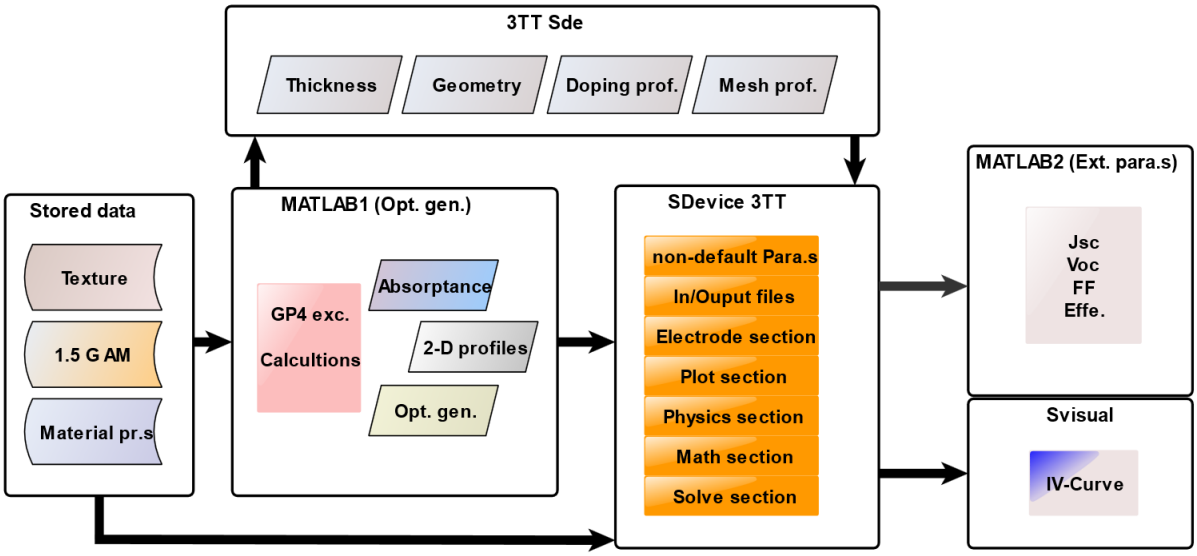

Figure 9 Flow chart of opto-electrical simulation process.

The first tool in our simulation process is a MATLAB code embedded in SWB. Which imports the external GenPro4 software to execute optical simulations. This code also transfers the optical generation outputs to 2-D profiles so they can be used in Sentaurus structure design editor (SDE) tool and Sentaurus device (S.Device) tool.

Next, in the simulation process, comes SDE tool, which is used to design the geometry of the 3TT device. The tool also builds the grids of the device structure and assigns electrical contacts, doping profiles, optical generation profiles to different regions and materials in the structure. Furthermore, it builds the meshing profiles of the device and tune it according to the specified requirements of the simulation or scenario.

After that, the SDE's outputs together with materials characteristics & parameters are taken by the S.Device tool as inputs to carry out the simulation of physical models. Many of these parameters and values need to be added or adjusted manually in the S.Device based on the literature reference values. Otherwise, Sentaurus will use default values which may shift the output results and lead to incorrect outcomes. Table 1 summarizes the featured material's characteristics and parameters in the 3TT device that need to be supplied to the S.Device in order to solve the simulations correctly and imitate the characteristics of our proposed 3TT device.

Table 1: Material parameters which need to be implemented in Sentaurus S.Device to imitate the characteristics of the proposed 3TT device.

Parameter Mat. name	E_g [eV]	X_e [eV]	ϵ []	μ_n [$cm^2/V.s$]	μ_p [$cm^2/V.s$]	N_D [cm^{-3}]	N_A [cm^{-3}]	N_c [cm^{-3}]	N_v [cm^{-3}]
c-Si	1.12 [8]	-4.05 [8]	11.9 [69]	1400 [70]	470 [70]	$2x10^{15}$ [71]	-	$2.8x10^{19}$ [71]	$1.04x10^{19}$ [71]
Perovskite	1.62 [72]	-3.82 [72]	30 [72]	0.7 [73]	0.4 [73]	-	-	$2.2x10^{18}$ [74]	$1.8x10^{19}$ [74]
Sipro-OMeTAD	3.0 [74]	-2.2 [74]	3 [74]	$1x10^{-4}$ [75]	$1x10^{-4}$ [75]	-	$3x10^{18}$ [74]	$1.0x10^{18}$ [74]	$1.0x10^{20}$ [74]
SnO2	3.5 [76]	-4.0 [76]	9 [76]	20 [76]	10 [76]	$2x10^{19}$ [71]	-	$2.2x10^{18}$ [76]	$1.8x10^{19}$ [76]
ITO	3.6 [74]	-4.7 [74]	3.5 [74]	160 [74]	40 [74]	$1x10^{20}$ [74]	-	$4.1x10^{18}$ [74]	$1.7x10^{19}$ [74]
Poly-Si (n)	1.12 [77]	-4.1 [77]	11.9 [69]	1400 [70]	470 [70]	$1x10^{20}$ [58]	-	$2.8x10^{19}$ [58]	$1.04x10^{19}$ [58]
Poly-Si(p)	1.12 [77]	-4.1 [77]	11.9 [69]	1400 [70]	470 [70]	-	$1x10^{20}$ [58]	$2.8x10^{19}$ [58]	$1.04x10^{19}$ [58]
SiO2	8.9 [78]	-0.95 [78]	3.9 [79]	140 [79]	47 [79]	$5x10^{19}$ [18]	-	$2.7x10^{19}$ [18]	$3.1x10^{19}$ [18]

Where:

E_g: bandgap energy	X_e: electron affinity	ϵ: dielectric primitivity
μ_n (μ_p): e(h) mobility	N_A: Acceptor concentration	$N_{D:}$ Donor concentration
N_C: effective density of states of the conduction band	N_v: effective density of states of the valence band	

To help understand how the S.Device processes the simulations, we view briefly the content of its command file which has different sections, each of them is responsible to carry out a certain task or groups of tasks in the simulation process. First, the "File section" is responsible on calling out input flies and importing all files that are needed for the simulation to work properly as well as producing simulation's output files and plots. Second, the "Electrodes section", it declares which contacts in the structure to be used as electrodes. And it specifies the initial conditions of these electrodes. Third is the "Plot section" which specifies all physical properties that need to be extracted from the simulation results and illustrated in the device structure. Forth is the "Physical section", where the suitable physical models are selected and applied on the whole structure, or certain region or material in the device. The selection of these physical models is user-specified, which means that the user has the freedom to include or exclude models based on his/her proposed theory/ies. Table 2 gives a brief summary of the physical models used in simulation of 3TT device of this project. Further, the "Math section" is responsible for the speed, step size, number of iterations and computational initial conditions of the simulation. Finally, the "Solve section" determines how the electrodes are swept, the logical dependency of physical models in the solving process, the conditions when the solving starts and breaks out, and the goals that need to be reached in the simulation.

Table 2: Based on the device structure band diagrams and the 3TT device working mechanism. Table 2 summarizes the needed physical models to be solved in the S.Device in order to obtain valid opto-electrical simulations of our proposed 3T Perovskite/ TopCon IBC tandem device.

Physical concept	Physical model
Charge carriers transport	Drift-Diffusion Model
Heterostructure device simulation	Thermionic emission
Recombination	SRH recombination
	Auger recombination
	Radiative recombination
Interface recombination	SRH surface recombination
Free carrier statistics	Fermi-Dirac
Tunneling	Band to band tunneling
Doping	Constant profile doping
Free carrier mobility	Mobility Model
	High field saturation

Table 3 Parameters used in simulation for carrier recombination models.

Parameter	Value	Description
	Perovskite	
β [$cm^3.s^{-1}$]	$1.0x10^{-10}$	Radiative recombination [80]
C_n [$cm^6.s^{-1}$]	$1.0x10^{-29}$	Auger recombination (eeh) [81]
C_p [$cm^6.s^{-1}$]	$1.0x10^{-29}$	Auger recombination (ehh) [81]
	c-Si	
β [$cm^3.s^{-1}$]	$4.73x10^{-15}$	Radiative recombination [82]
C_n [$cm^6.s^{-1}$]	$2.8x10^{-31}$	Auger recombination (eeh) [82]
C_p [$cm^6.s^{-1}$]	$1.0x10^{-31}$	Auger recombination (ehh) [82]

Finally, Sentaurus visual (SVisual) tool is used to plot and analyze the band diagrams, physical variables such as current densities, carriers' distributions, electric field, etc. The tool also exports all user-selected simulation's outputs to be displayed or for further processing. Then an extra MATLAB code can be used to obtain certain useful quantities such as efficiency, MPP-power. MPP-current etc.…

Figure 10 shows the processing dependency of the various Sentaurus tools in the workbench and the order of simulation priorities.

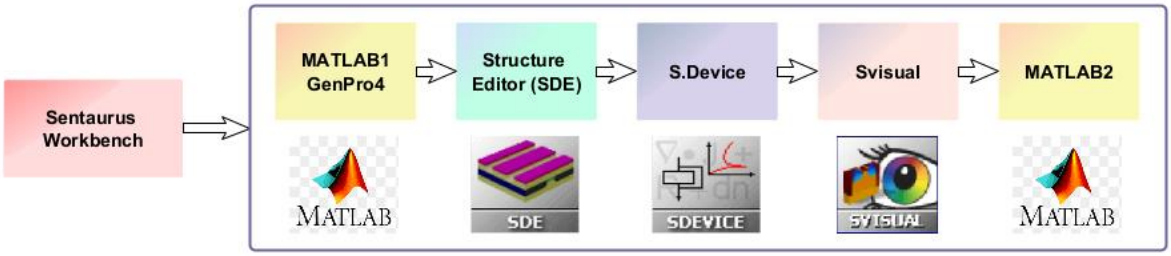

Figure 10 Sentaurus tool's dependency.

2.4 Optical simulation approach

After the whole simulation workflow and Sentaurus software's line of action have been described in the previous section. This section further explains the optical simulation methodology, gives a brief introductory to GenPro4 software, and discusses how optical generation rate profiles are extracted from GenPro4 and transferred to Sentaurus SDE tool.

The optical simulation in this project aims to extract the values of optical absorption caused by each layer of the tandem to calculate for both optical losses and generations. For this purpose, GenPro4 software uses both wave and ray's optics to accurately obtain absorptance and optical generated current in a relatively short computational time. The software makes use of Fresnel equations and Lambert-Beer law to calculated for transmittances and reflectance's on interfaces between flat layers (net radiation method) [83]. GenPro4 is also used to optimize the tandem device optically by trying different thicknesses, adding ARC layers as well as adding texture patterns at the bottom or the top of the sub-cells. In this project, only one ARC layer was added, and no surface texture was implanted. Because (based on fabrication techniques used to produce such tandems), adding a thin film PSC on c-Si cell requires that the c-Si bottom cell to have a flat top surface [84].

As it was mentioned earlier, GenPro4 is integrated with Sentaurus workbench as external tool. And it needs a MATLAB code that executes GenPro4 and exports its outputs to SDE device in form of optical generation rate (OGR) profiles in the depth domain. The depth profile is needed because the electrical simulation is based on FEM that requires generation profile for each 2-D mesh block. Thus, the optical generation profile should be distributed as a function of depth.

Our method of calculating the OGR profile is by dividing the absorber medium into several slices in the y-direction (depth). The silicon slab was sliced to equal slices of thickness 0.1 μm, and the perovskite slab to slices of 0.01 μm. This slicing method guarantees a high resolution of the changes in optical generations rate along all points of depth. Then, the optical generated current density for each slice in

each absorber is extracted from GenPro4. The extract photo-current density is then used to calculate the optical generated rate by the following equations:

$$G = \frac{n}{\Delta V.\Delta t} = \frac{n}{d.A.\Delta t} \quad (4)$$

Where G is the OGR per unit volume, ΔV is Volume unit, Δt = time interval, n is the number of electrons generated by absorbed light and d is thickness of layer. While Optical Current density can be expressed as:

$$J_{ph} = \frac{I}{A} = \frac{\Delta Q}{A.\Delta t} = \frac{q.n}{A.\Delta t} \quad (5)$$

Where q is the charge of electron, A is cross section area of the layer. Then the total optical generation rate produced by a slice of thickness d can be expressed as:

$$G\_slice = \frac{J_{ph}}{q.d\_slice} \quad (6)$$

After doing these calculations for all slices in an absorber, a table of generation rates vs depth is formed which presents the generation rate profile for that absorber. Then that table is saved in a file which is exported to the SDE device and applied in the SDE tool on absorber layer. Figure 11 displays the OGR profiles for perovskite and c-Si absorber layers respectively as they are applied on the device structure made by SDE tool.

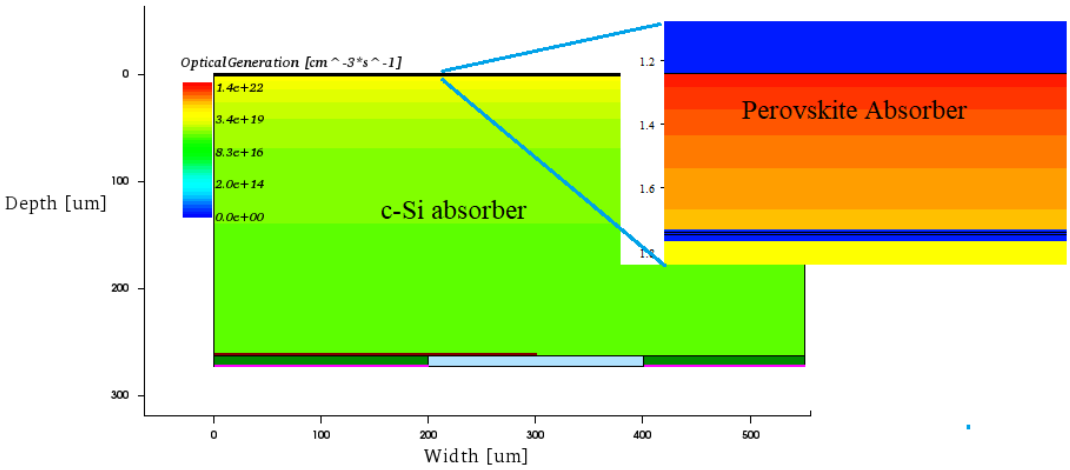

Figure 11 Optical generation rate profiles as they are applied on c-Si & Perovskite's absorber layers respectively in the 3TT PSC/c-Si IBC device.

From the figure above, it is seen that the highest generation occurs in the first few nanometers of the perovskite layer. then the generation drops exponentially with the depth. While for c-Si layer, it starts with lower generation rate than that of perovskite then it drops exponentially. The exponential drop in both layers is because the flux of the light is highest near the top surface of the layer. thus, it can generate the most of electron-hole pairs. But the deeper the light penetrates, the sharper the flux decays because most of it is either already converted to photo-current or reflected. Only a tiny part penetrates. This effect has influence on the recombination losses. since charge carriers generated near the surface of the layer need to travel short distance if the terminal is closer to the surface and longer distance if the terminal is at the bottom and vice versa for carriers generated far from surface.

2.5 Electrical simulation approach

The purpose of electrical stimulation is to describe and analyze the electrical behavior of charge carriers in the tandem device. This can be realized by numerically solving the physical models of carrier's transport in semi-conductors based on drift diffusion model. Which is a model that solves differential equations of drift current (caused by the presence of electric field in the material) and diffusion current (caused by difference in concentration of charge carriers) in time-space domain. More can be found in [85]. But as mentioned earlier, it is necessary to perform electrical simulations in both dark and illuminated conditions to have a full picture of the device behavior. Below is a description of how to obtain these simulations and the simulation band diagram at each set of conditions:

2.5.1 Band diagram at dark conditions

The dark condition measurements are done by introducing the charge carriers in the cell circuit with electrical means rather than by solar simulator. This is because the fluctuation of light intensity will create a noise in readings of charge carriers which are generated by illumination [86]. That is why dark measurements or simulations are more accurate in determining IV characteristics of solar cells and the quality of the junction.

To obtain the electrical simulation at dark, the condition in the S.Device should be set to "light turned off" and the initial applied voltage to zero (0 V). The solution then is used as initial solution to solve the continuity equations for electrons and holes iteratively by increasing the applied voltage in small steps. Each time the voltage is increased, the initial conditions are applied from the solution of the step before it until the sweeping reach its final goal. This allows to solve the Poisson's equation at initial boundary at dark conditions. The graph below displays the resulted simulated band diagram in dark conditions for the proposed 3TT device using Sentaurus TCAD. Where the conduction band edge is presented in green, valence band edge in red, and fermi level as a dashed line. As it is expected and can be seen from Figure 12, the fermi level across the whole device is the same which confirm that the simulation is indeed at dark condition where the quasi-fermi level of electrons is equal to that for holes. As well, it indicates that no photocurrent is generated in dark conditions. It is also observed that there is a steady alignment of the lower level of conduction band that pave the way for electrons to diffuse naturally from the top layers to the bottom layers across the whole 3TT device.

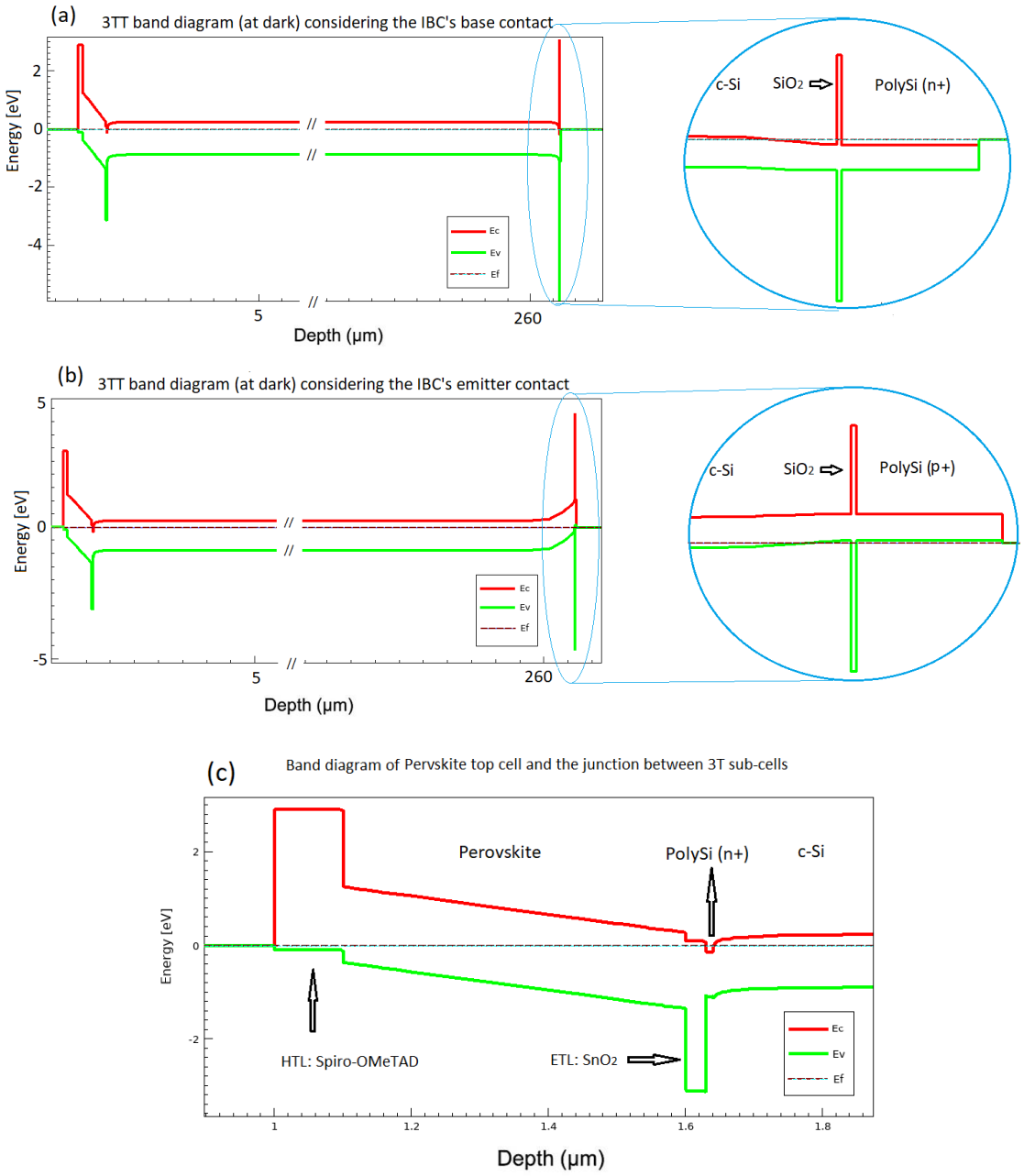

Figure 12 Simulated band diagrams of 3TT device using TCAD at dark conditions.

Further, Figure 12 (a) represents the simulated band diagram at dark regarding the top cell, junction between sub-cells, and the junction between IBC and rear bottom base (n-Contact) with a zoom-in on the stack c-Si/SiO2/polySi (n+). While Figure 12 (b) represents the band diagram of the 3TT regarding the top cell, junction between sub-cells, and the junction between IBC and rear bottom emitter (p-contact) with a zoom-in on the stack c-Si/SiO2/polySi (p+). The difference between figure (a) and (b) is the type of passivated contact. Where in (a) the contact is made of heavily doped n-type polysilicon layer that serves as ETL for the IBC cell and in (b) the contact is made of heavily doped p-type polysilicon layer that serves as HTL for the IBC cell. By zooming-in into these junctions, it is observed that the band-bending and conduction or valence band offsets agree with purpose of these layers. Where the base contact attracts electrons and builds a barrier against holes while the emitter attracts holes and builds a barrier against electrons.

On the other hand, Figure 12 (c) is a zoom-in of the stack HTL/perovskite/ETL/nploy(n+)/c-Si. It is observed that the band bending of the Perovskite intrinsic absorbing layer is resembling the expected behavior of this layers in the dark, where a build-in electric field is formed. Furthermore, it is observed that the resulted conduction band offset between the perovskite layer and ETL is relatively small compared with that between perovskite and HTL which is in agreement with the theoretical assumption that the ETL should facilitates the flow of electrons to the bottom cell and the HTL should block them form passing to the top. Similarly. The valence band offset between the HTL & perovskite is relatively small and that between ETL & perovskite is large which is favoring holes created in the perovskite layer to pass to the top and to be blocked by the ETL.

2.5.2 Band diagram at illuminated conditions

Illuminated conditions are important to measure because they unveil the solar device behavior and performance when interacting with light [86]. For example, the change in light intensity will influence all the external cell parameters such as the short circuit current, open circuit voltage, shunt resistance and filling factor. Also illuminated conditions show the realistic influence of each layer in the device on light and on generated charge carriers.

To simulate the 3TT device under illuminated conditions, we use a similar approach but slightly different from dark conditions. After the solution of Poisson's equation is obtained at initial conditions, this solution is set as initial condition for continuity equation. Here however, the light is then turned on to one sun while followed by increment increasing of the voltage in small steps. The sweeping span is set to break when V_{OC} is reached because it is pointless to keep increasing the applied voltage after the V_{OC} is reached since no current will be generated. The correspondent simulated band diagrams of the proposed 3TT device at illumination conditions is shown in Figure 13. It can be seen in all-band diagrams, that the fermi energy levels for electrons and holes are not matching each other anymore and they are E_{Fn} & E_{Fp} respectively. The gap between them indicates the creation of open circuit potential caused by the conversion of photons energy to potential energy in the charge carriers. The open circuit voltage is limited by the photo-generated current, and the difference between work functions of ETL & HTL layers in the Perovskite top cell, and by the difference between passivating contact work functions in the bottom IBC cell.

Further, the figure distinguishes between two cases, the first case (Figure 13 (a)) when the sweeping voltage is applied on the top terminal (p2Contact), and the band diagram between top front terminal and the rear back base terminal is considered. In this case, it can be observed that the top terminal is acting as a hole collecting terminal, while the rear base is acting as electrons collecting terminal. By investigating the band diagram between c-Si and polySi (n+) layers. It can be seen (from the zoom-in circle) that the rear base contact is very likely to behave as electrons selective layer through tunneling of major charge carriers. This is made possible by the existing thin SiO_2 layer which has low electron affinity and large bandgap energy. If the thickness of the SiO2 layer is small enough (ultra-thin < 2nm), the tunneling effect is maximized and almost all electrons will tunnel while hindering holes' transport.

The second case (Figure 13 (b)) when the band diagram between top front terminal and the rear back emitter terminal is considered. It is observed in this case that the top cell band diagram is similar to that at dark condition with the exception of the split in quasi-fermi levels. This is because the applied voltage at the rear emitter contact will not influence the front top contact since the flow of holes between them is blocked by the ETL layer in the perovskite cell. This leads to a non-engagement of the top cell. Which indicates that charge carriers cannot intercross between these two terminals. And this

confirms that both sub-cells are indeed independent in operation since the generated holes are collected exclusively by each sub-cell independently. And that confirms again that the structure used in this tandem device is indeed leading to three terminal layout.

As it was for rear base contact, the investigation of the band diagram of the stack c-Si/SiO2/polySi (p+) layers lead to the same conclusion that the polySi (p+) layer acts as a tunneling selecting contact for holes where almost all holes will tunnel, and electrons transport is hindered if the SiO_2 layer is thin enough.

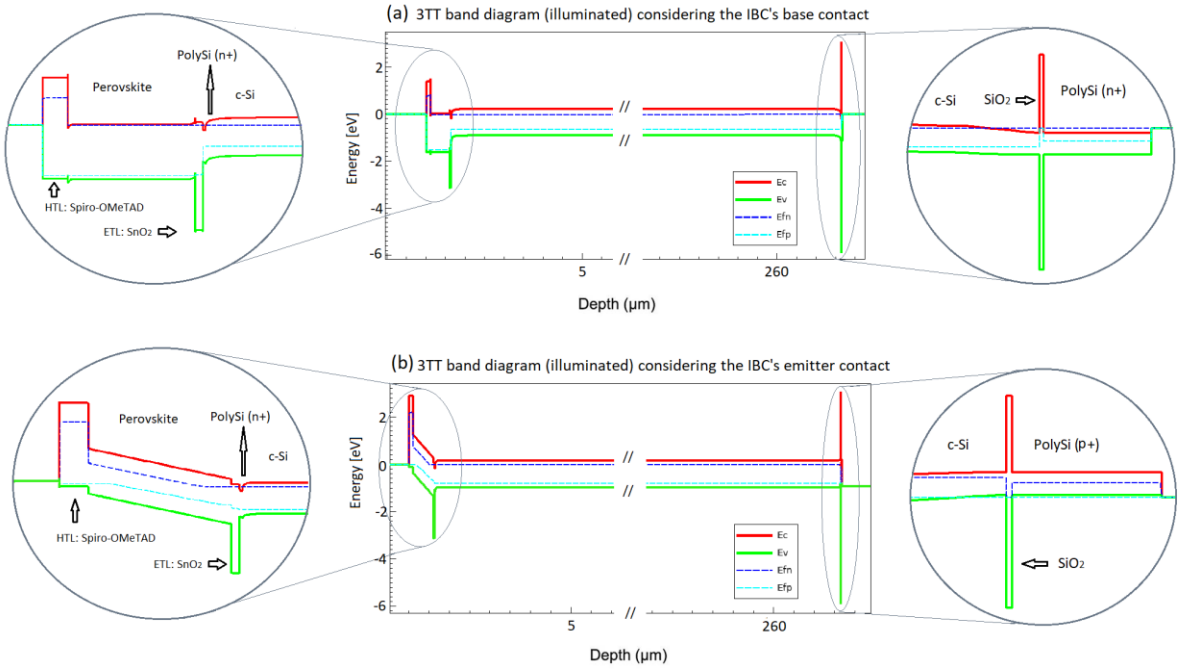

Figure 13 3TT device band diagrams under illumination.

It can be concluded that the band diagrams confirms that the structure is indeed a 3TT structure and it agrees with the working principles of the proposed device which were discussed in section 2.1 & 2.2. where the front top terminal collects only the holes that are generated at the top cell, the rear emitter collects only the holes that are generated at the bottom cell with no holes intercrossing between the sub-cells. And the rear base collects electrons from both sub-cells. which leads to independent operation of each sub-cell.

2.5.3 Approach to obtain the J-V curves

After performing the electrical simulation in dark and illuminated condition and confirming that the respective band diagrams agree with the 3TT device's working principles, the subsequent step is to be able to extract the correct J-V simulated data for the tandem device and the respective sub-cell's (sub-circuits). It is worth mentioning that we deal here with 3T device which has more complex electrical circuitry than a 2T or 4T devices. Simply because a 3T device represents two independent circuits but coupled at the same time. Which adds extra degree of freedom to the current-voltage relations. That means, the full performance of the device can only be obtained by measuring at least one variable in each circuit simultaneously (two voltages, two currents, or one current of one circuit and a voltage

from the other) [46]. Graphically, the current-voltage relation of the whole tandem also cannot be described fully by a line (J-V curve) but rather with a surface (contour plots) [53]. That is why the "solve section" in the S.Device needs to be conditioned carefully to obtain valid 3T simulation's results. Which means that the sweeping span, initial conditions, and goals in that section are dependent on which electrode it is swept, and which voltage is investigated. The following figure aims to explain how the voltage sweeping in the S.Device is performed and conditioned.

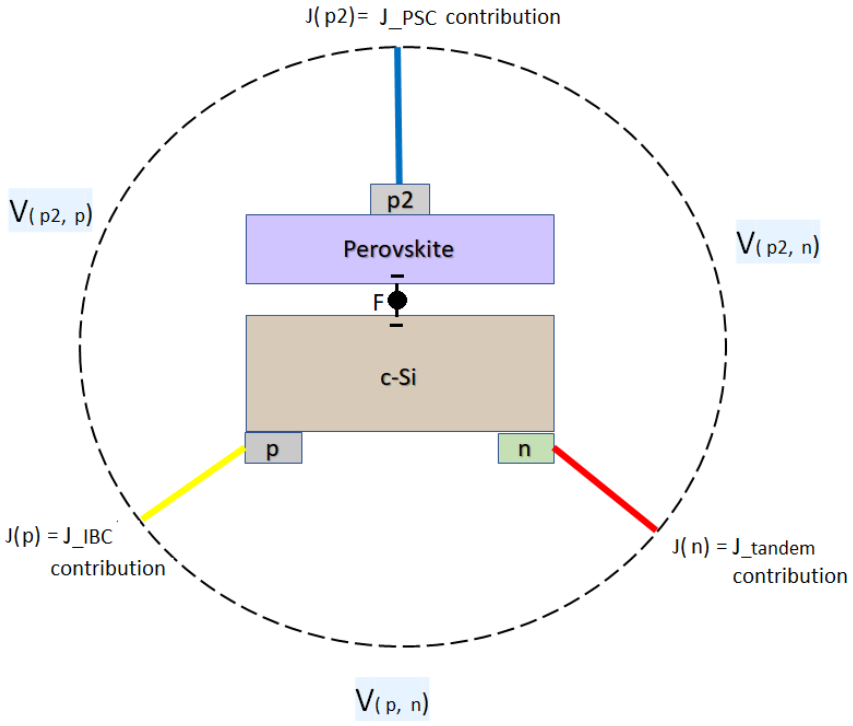

Figure 14 Schematic representation of the 3TT simplified circuitry and loading.

Figure 14 above displays a schematic representation of the 3TT simplified circuitry and loading. showing the electrodes of the 3TT device, the voltages between these electrodes, the current collected/accumulated between them, and how they are related.

Where F is a virtual point that separate the negative back side of the top cell from the negative front side of bottom cell, the point is added only for convenience to understand the circuits. J_p is the current collected or accumulated between the rear back emitter terminal (p-contact) and the point F, J_{p2} is the current collected between the front top (p2-contact) and the point F, J_n is the current collected between the rear back base (n-contact) and the point F, $V_{p2,n}$ is he voltage between the front p2-contact and the back n-contact, $V_{p2,p}$ is the voltage between the front p2-contact and back p-contact. and $V_{p,n}$ is the voltage between back p and back n contacts.

From Figure 14 there are three terminals where only two can have loads while the third is treated as a common terminal (otherwise the system will be overstrained) [46]. These two loads allow measuring the contribution of both bottom and top cells. Thus, the summation of the power generated simultaneously by two sub-cells, represent the total power produced by the 3TT device.

Case1, sweeping the voltage at p-contact while n-&p2-contacts remain at zero voltage. In this case, the circuit between p-&n-contacts (IBC) will experience the applied voltage which will change from 0V to V_{OC_IBC}. The applied voltage will allow the current between p-contact and point F (J_{p2}) to be collected which represents the holes generated by the IBC cell. While the collected current between point F and the n-contact (J_n) will represent the total contribution of the tandem device since the n-contact collects electrons from top and bottom cells together. J_n will also be limited by the voltage between n-&p-contacts and falls to zero when the applied voltage reaches V_{OC_IBC}. On the other hand, the accumulated current between the point F and the top p2-contact will remain constant because the top cell is not affected by the bottom p-contact and thus won't react to the applied voltage. The current therefore will remain at the same initial voltage condition which is $J_{\_SC\_PSC}$. That is why it won't decrease when the voltage at p-contact increases. Thus, the J-V curve of the top cell will be a straight line. The extracted results from the first sweeping case are shown as follow:

- If P-contact is swept, voltage difference between p-&n-contacts (V_{p-n}) is taken, current density collected between F and p-contact (J_p) is taken. The following J-V curve is produced in Figure 15.

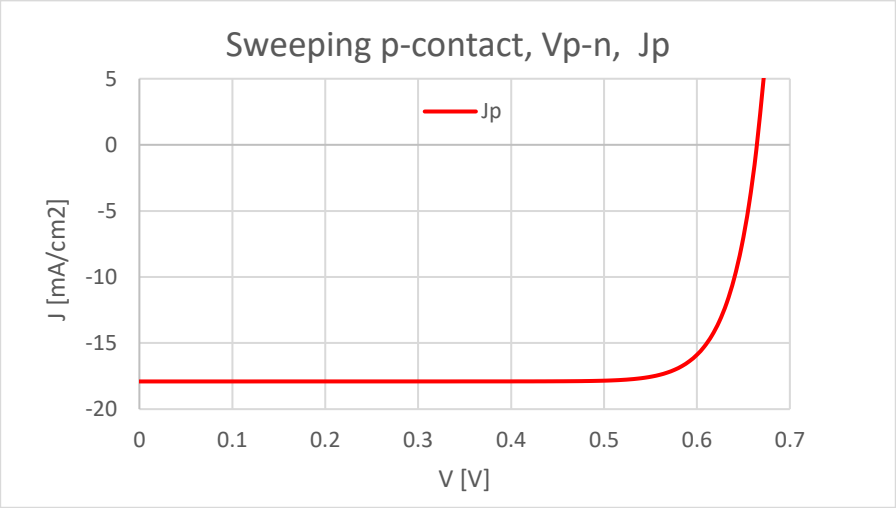

Figure 15 Current at p-contact when the voltage at p-contact is swept.

Which represents the contribution of the IBC absorber into the tandem cell. It is noticed that the open circuit voltage is also matching that of the IBC cell. And the current density is negative because it represents the collected holes.

- If P-contact is swept, voltage difference between p&p2-contacts (V_{p-p2}) is taken, current density is J_{p2}. The following J-V curve is produced in Figure 16. Which represents the contribution of the perovskite cell within the tandem device. It is noticed that the curve does not have an open circuit voltage (the current density remains the same over the sweeping span). This is because the sweeping voltage has no influence at the top cell since the holes at the top or the bottom cell are blocked from inter-crossing. Thus, the current density at the top cell remains at the 0V condition (J_{SC} condition). And that confirms that the 3TT configuration is indeed working properly since the target from this configuration is to prevent holes created locally at each sub-cell from crossing to the other sub-cell.

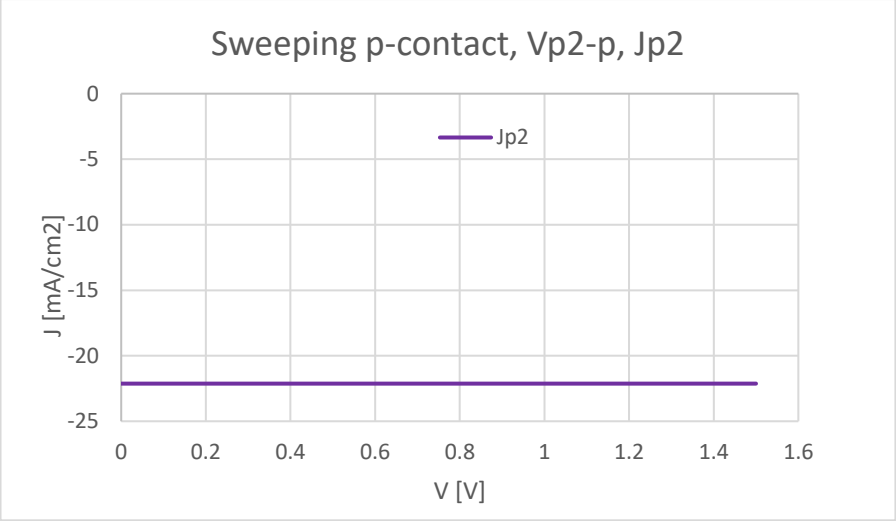

Figure 16 Current at p2-contact when the voltage at p-contact is swept.

- If P-contact is swept, voltage difference between p-&n-contacts (V_{p-n}) is taken, and current density collected is J_n. The following J-V curve is produced in Figure 17.

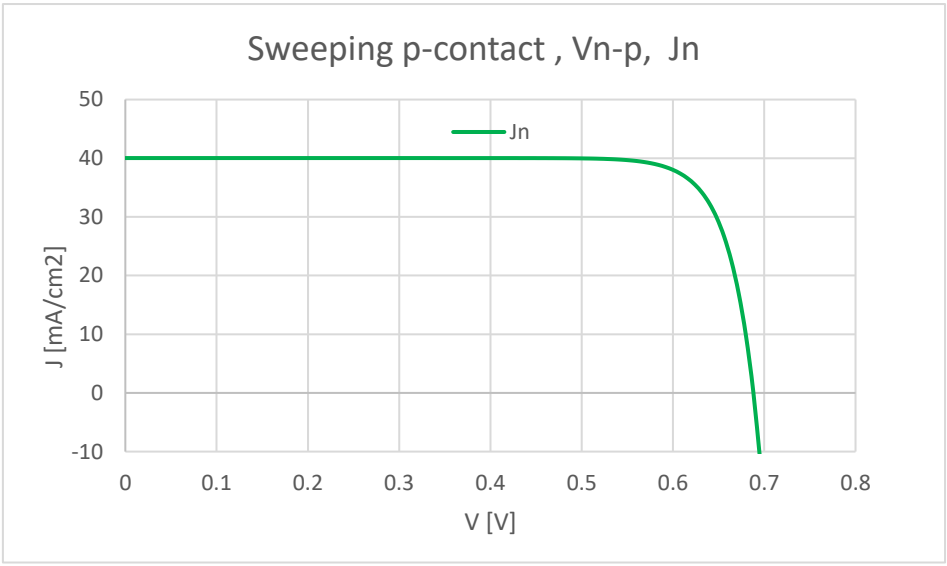

Figure 17 Current at n-contact when the voltage at p-contact is swept.

Which represents the contribution of both absorbers (tandem current) into the tandem cell. It is noticed that the open circuit voltage is matching that of the IBC cell which is logical since the voltage created between n-&P-contacts is limited to the V_{OC} of the IBC cell. And the current density is positive because it represents the collected electrons.

Case2, when the p2-contact voltage is swept, while the p-&n-contacts remain at zero voltage. The sub-circuit connecting p2- and n-contacts will experience the applied voltage which will change from oV to V_{OC_PSC}. Thus, the current collected between F and the p2-, or n-contacts will drop to zero when the applied voltage reaches the V_{OC} of the perovskite cell. On the other hand, the current collected between F and p-contact will remain constant since the holes exchange between top and bottom cells is forbidden both ways. The extracted J-V curve results from the second sweeping case are shown as follow:

- If P2-contact is swept, voltage difference between p2&p-contacts ($V_{p2\text{-}p}$) is taken, current density collected is J_p. The following J-V curve is produced in Figure 18. Which represents the contribution of the IBC bottom cell within the tandem device. We notice that the curve does not have an open circuit voltage and the current accumulated between F and p-contact is matching that of the J_{SC} IBC cell and it remains constant. The reason for that is the same reason mentioned earlier regarding the blockage of holes from intercrossing between the sub-cells. (But in this case, we notice that at higher applied voltages, the current start to show small changes which could indicate a leak of holes occurring at high applied voltages. But investigating the reasons for that behavior is beyond the scope of this project).

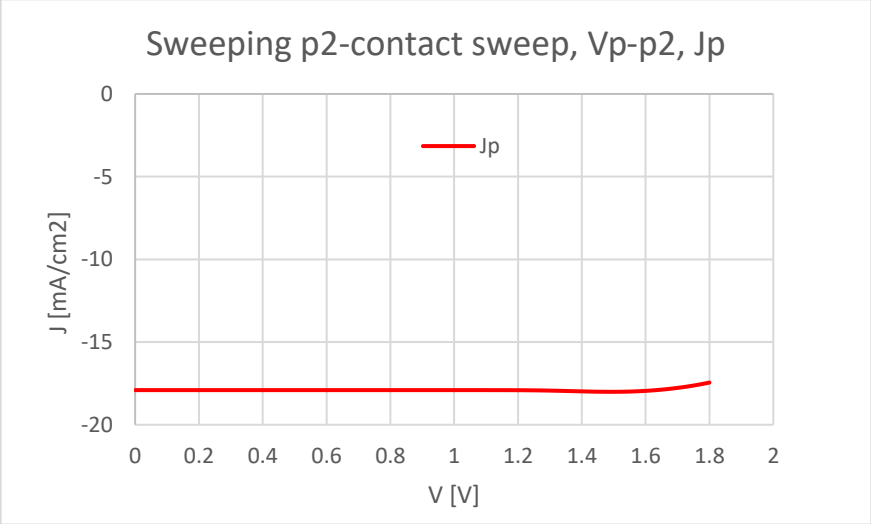

Figure 18 Current at p-contact when the voltage at p2-contact is swept.

- If P2-contact is swept, voltage difference between p2-&n-contacts ($V_{p2\text{-}n}$) is taken and collected current density is J_{p2}. The following J-V curve is produced in Figure 19.

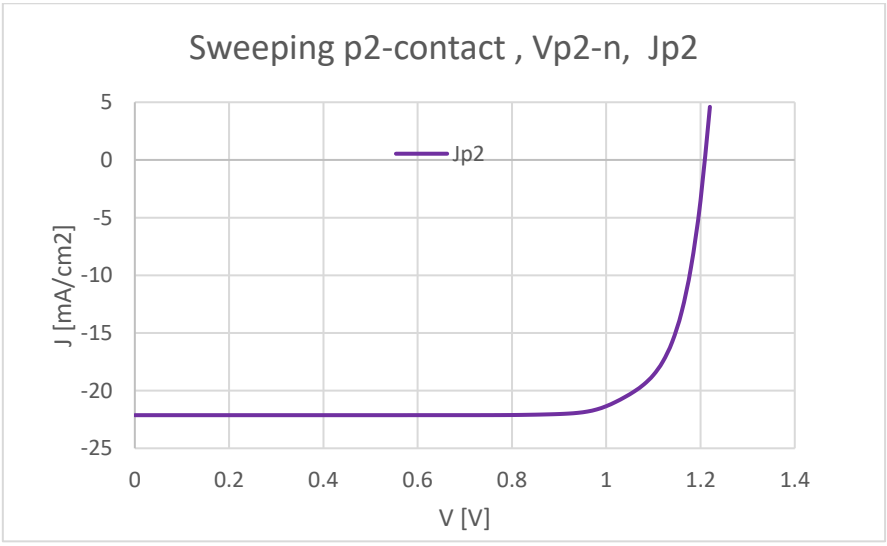

Figure 19 Current at p2-contact when the voltage at p2-contact is swept.

Which represents the contribution of the top cell in the tandem device. The open circuit voltage here is also matching that of the PSC cell. And the current density is negative because it represents the collected holes.

- If P2-contact is swept, voltage difference between p2&n-contacts (V_{p2-n}) is taken, and the collected current density collected is J_n. The following J-V curve is produced in Figure 20.

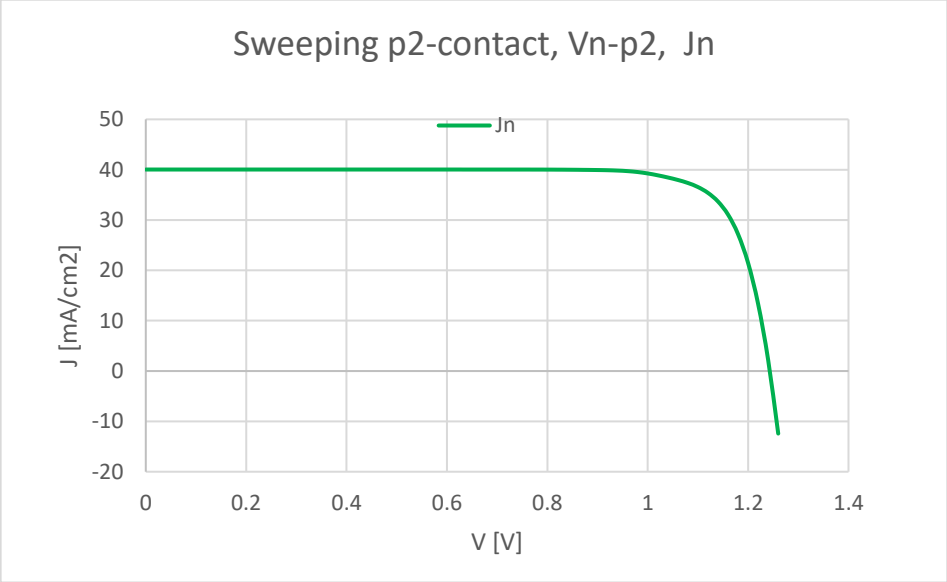

Figure 20 Current at n-contact when the voltage at p2-contact is swept.

Which represents the contribution of both absorbers (tandem current) into the tandem cell. It is observed that the open circuit voltage is matching V_{OC_PSC}, which is logical since the voltage created between n&P2-contacts is limited to the V_{OC} of the PSC cell. And the current density is positive because it represents the collected electrons.

Case3, sweeping the voltage at n-contact while p-&p2-contacts remain at zero voltage. The sweeping span in this case will be in the negative domain (reversed biasing) since the n-contact has negative polarity. And the applied voltage on the n-contact will influence the current accumulated at all three terminals. The two sub-circuits (n- with p2-contacts and n- with p-contacts) will witness a changing in current flow based on the applied voltage. Therefore, the current collected between F and n- or p-contact will drop to zero when the applied voltage exceeds V_{OC_IBC}, while the current collected between F and p2-contact will drop to zero when applied voltage exceeds V_{OC_PSC}. The extracted results from the third sweeping case for the contribution of each sub-circuit are shown as follow:

- If n-contact is swept, voltage difference between n-&p-contacts (V_{n-p}) is taken, and the collected current density collected is J_p. The following J-V curve is produced Figure 21.

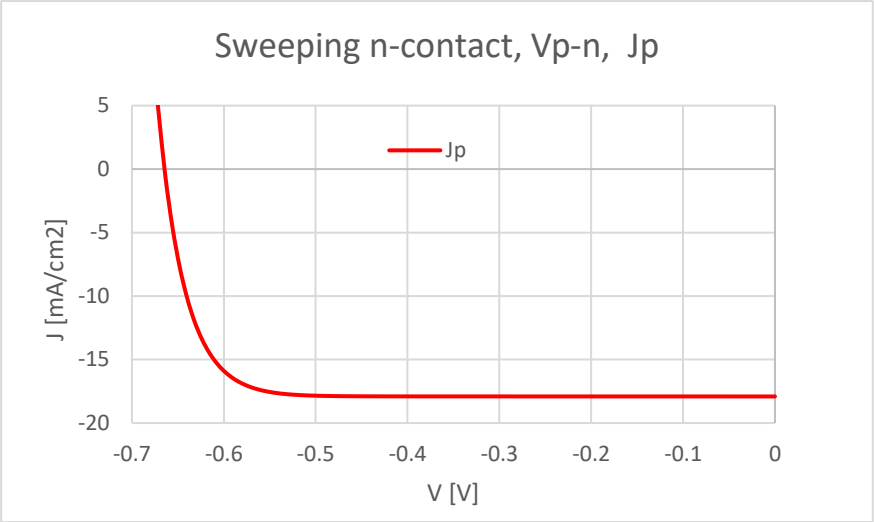

Figure 21 Current at p-contact when the voltage at n-contact is swept.

Which represents the contribution of the IBC absorber in the tandem device. We notice that the open circuit voltage is matching the IBC V_{OC} but in negative direction because the sweeping polarity now is reversed while the current accumulated on p-contact is matching that of the IBC cell. And the current density is negative because it represents the collected holes.

- If n-contact is swept, voltage difference between n&p2-contacts ($V_{n\text{-}p2}$) is taken, and the current density collected is J_{p2}. The following J-V curve is produced Figure 22.

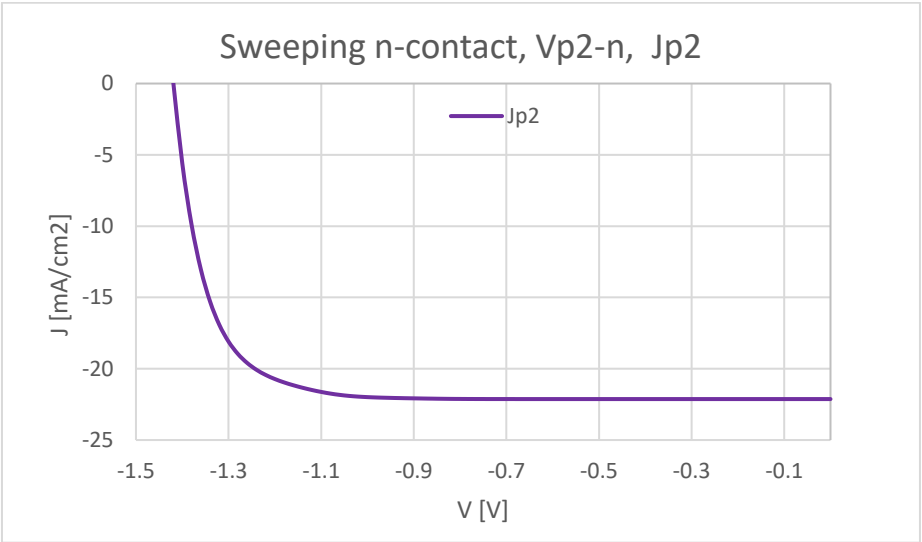

Figure 22 Current at p2-contact when the voltage at n-contact is swept.

Which represents the contribution of the top cell in the tandem device. The open circuit voltage here is also matching that of the PSC cell but again negative because the polarity is reversed. And the current density is negative because it represents the collected holes.

- If n-contact is swept, voltage difference between n-&p-contacts ($V_{n\text{-}p}$) is taken, current density collected between F and n-contact (J_n). The following J-V curve is produced Figure 23.

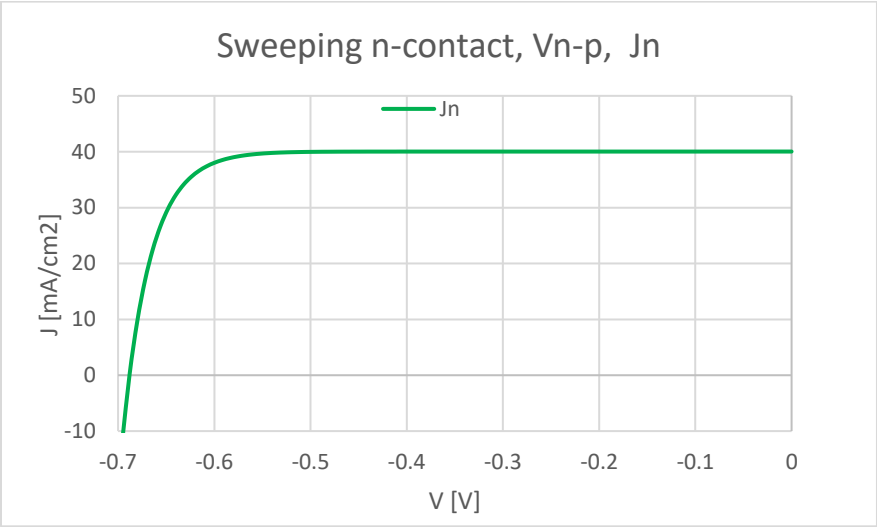

Figure 23 Current at n-contact when the voltage at n-contact is swept.

Which represents the contribution of both absorbers (tandem current density) in the tandem device. The open circuit voltage is matching that of the IBC cell which is logical since the voltage created between n-&P-contacts is limited to the V_{OC} of the IBC cell. And the current density is positive because it represents the collected electrons.

2.6 Conclusion

The purpose of this chapter was to achieve the first objective of this project, which is proposing and designing a high efficiency 2-D 3TT PSC/c-Si IBC device's model. This was realized by proposing a device structure which complies with 3TT device's working principle. Furthermore, the functionality, material choice, and initial geometry parameters of each layer in the structure were determined based on experimental and literature references. After that, the simulation and software setups as well as the methodology and process flow were explained. In addition, optical simulation approach was discussed in more details. This included the use of GenPro4 software as well as the method to produce optical generation depth profiles to be used by SDE tool in 2-D simulations.

Finally, an electrical simulation approach was created for 3TT device's circuitry which is more complicated than that of two terminal or four terminal devices. Where 3TT device has independent operational cells but one terminal is shared between them at the same time. We described how to simulate such device in dark and illuminated condition and explained how to obtain J-V curve for each sub-cell.

This chapter also showed the simulated band diagrams of the proposed 3TT device in both dark and illuminated conditions, which showed what was expected theoretically from this structure and confirmed that the device indeed functions as a three-terminal device. Furthermore, the initial simulations were used to show how to obtain J-V curves of each sub-cell and how these curves are related to the terminal which is been swept in voltage.

The next step will be to validate this model and compare its outputs with those of SJ & 4TT models that are identical in material choices and/or geometry and/or structure.

3 3TT Device's Simulation Results and Discussions

The goal of this chapter is to achieve the second objective of the project. Which is to validate the model and compare the three terminal (3T) sub-cells with the reference single junction (SJ) cells as well as with another tandem configuration. Section 3.1 views the optical generation profiles of SJ IBC, SJ perovskite solar cell (PSC), and 3TT PSC/c-Si IBC device and examines the accuracy of these profiles. In section 3.2 the electrical simulation outputs of SJ IBC, SJ PSC, and 3TT PSC/c-Si IBC device are presented. These outputs confirm the working of 3TT device. Then the performance of the SJ sub-cells with the correspondent 3T sub-cells is compared. Moreover, section 3.3 makes the comparison between the 3TT device model and an identical 4TT device model. The comparison is helpful to demonstrate the competency of the 3TT model with other tandem configurations.

3.1 Optical simulation results

This section aims to display and analyze the optical simulation results based on GenPro4 software's outputs and the MATLAB code which was impeded in the SWB tool. The optical simulations were carried out for the 3TT device as well as for the reference SJ cells.

3.1.1 Optical generation absorptance

First, the optical generation absorptance was obtained and optimized by GenPro4 for SJ IBC & SJ PSC under one sun spectrum for each cell individually. Both SJ cells were set to have flat front surfaces, same layer's thicknesses, material properties, and 2-D geometry like that of the proposed 3TT device model. Then we show the absorptance of the 3TT device. The reason for this is to make a fair comparison between the SJ cells and their correspondent 3T sub-cells.

Figure 24 shows the simulated absorptance of the SJ reference cells. It can be seen that the SJ IBC suffers from low absorption between the ultra-violet to the blue regions of spectrum while it maintains high absorption in the green to near infra-red regions. On the other hand, SJ PSC shows high absorption in the blue short wavelength's region, while it shows almost no absorption in the long wavelength's region of the spectrum. It is also noticed that the SJ IBC cell can generate higher photogenerated current compared with the PSC due to its convenient indirect band gap.

The next step is to obtain the optical generation absorptance for the 3TT PSC/Si IBC device which was done again by GenPro4. The simulated results reveals that the 3T IBC and 3T PSC have performed optically less efficiently in the tandem device than their performance as SJ cells. Which is logical, since each sub-cell, in case of tandem, receives less light, since the one sun spectrum flux is split between both sub-cells. However, the absorptance in the whole tandem outperforms that of SJ cells. Since wider range of wavelengths and more energy is utilized. Figure 25 shows the simulated absorptance of the 3TT device in the domain of wavelengths. Where it can be seen that the 3T PSC utilized most of the high energy photons while the 3T IBC utilized most of low energy photons.

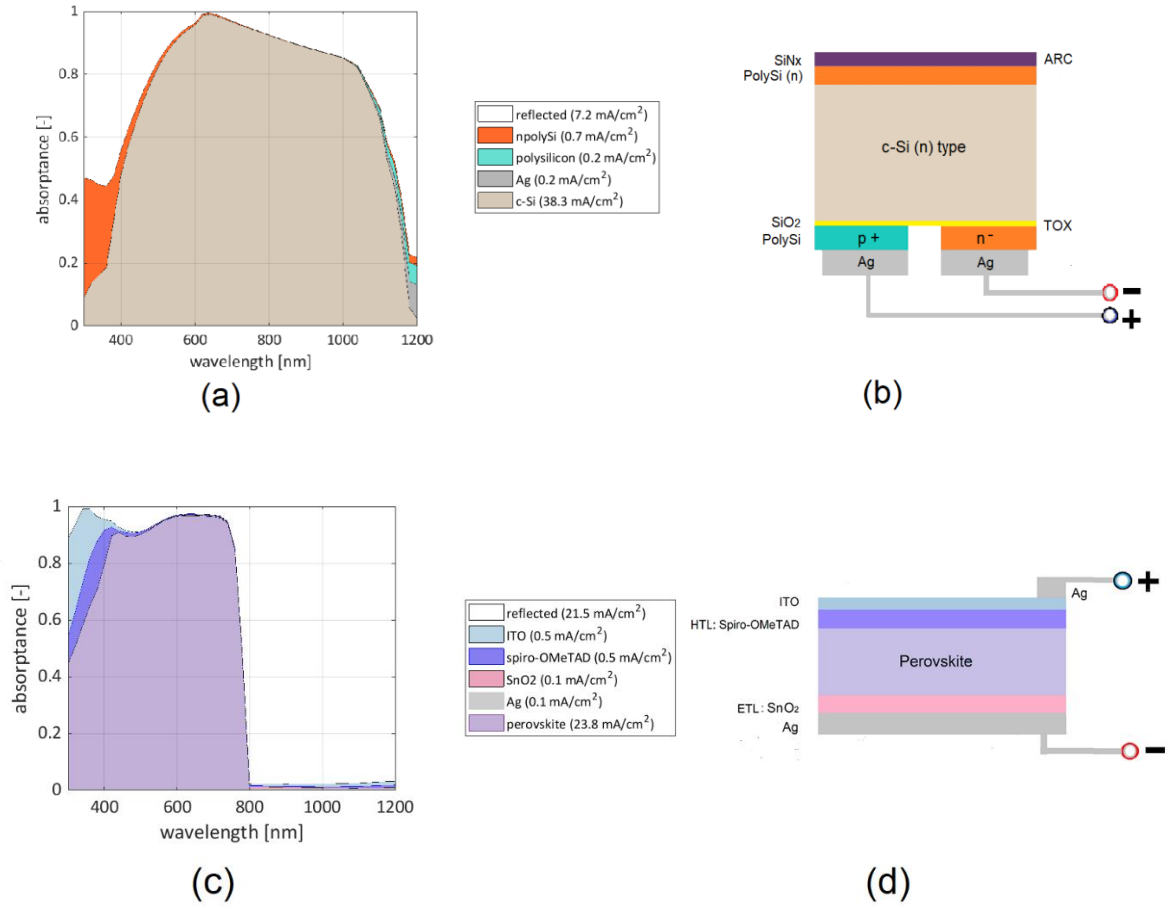

Figure 24 displays (a) the optical simulated absorptance of SJ IBC with 260 um thick bulk c-Si, flat top, and one layer of ARC (SiO_2). (b) is a schematic diagram of the SJ-IBC cell layer's structure. (c) the optical simulated absorptance of SJ PSC with 0,5 µm Perovskite's layer thickness, flat top, p-i-n configuration, and one layer of ARC. (d) is a schematic diagram of the SJ-PSC cell layer's structure.

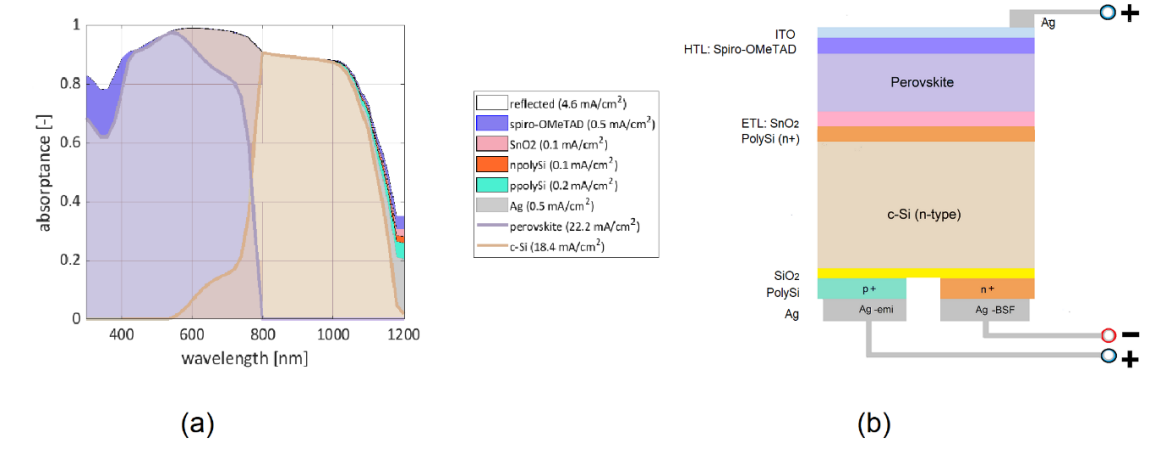

Figure 25 displays (a) the optical simulated absorptance of 3TT PSC/c-Si IBC device with flat top/flat middle and one layer of ARC (SiO_2). (b) is a schematic diagram of the 3TT device's structure.

3.1.2 Confirming accuracy of optical generation profiles

After the optical absorptance for the 3TT device model has been obtained and optimized. The next step was to produce the OGR profiles in the depth domain for that model. This is because these profiles need to be used as inputs for 2-D electrical simulations in Sentaurus, which works correctly only with optical generation rates that have depth profiling. The method how to produce these profiles has been discussed in section 2.4. However, applying these profiles in the SDE tools won't necessarily results with the same optical generation outcome as that obtained directly from GenPro4. This is due to differences between the interpolation methods and the way how the SDE tool apply them, and the resolution of the mesh profiles in the SDE tool. Which results in a mismatch between the direct profiles produced by GenPro4 and the converted profiles used by Sentaurus for the electrical stimulation. That is way examining the mismatch of these profiles is important step to assure the accuracy of electrical simulation's results.

To confirm the precision of our approach, the direct optical generation output of GenPro4 must be compared with the optical generation output extracted from solving the opto-electrical simulation in S.Device. This can be realized by calculating the OGR profile from the wavelength domain and compare it with the method that was discussed in section 2.4. If both are matching, then the method which is used is accurate and valid to be used for the simulations in Sentaurus TCAD. Calculating the OGR profile using the absorptance of wavelengths can be summarized as follow:

First the absorptance for each wavelength range in each slice (depth layer) is extracted. The result is a table for each slice of absorptance vs wavelength range. Then by using the photon flux of the sun for each range of wavelengths, we can calculate the optical generation rate for each wavelength range in a slice by the following equations:

- OGR produced by a wavelength λ at depth range Δx is

$$g(\lambda, x) = \frac{A(\lambda, x) * \varphi(\lambda)}{\Delta x} \quad (7)$$

  Where A(λ,x) is the absorption of photons at λ and depth x, where $\lambda < \lambda_o$, λ_o is the energy gap wavelength, ϕ(λ) is the spectral photons flux at λ.

- OGR for the whole wavelength's range in a slice layer of thickness d_slice is:

$$G(slice\_x) = \int_{\lambda i}^{\lambda f} g(\lambda, x).d\lambda \quad (8)$$

- Incrementally, the above integration can be written as:

$$G(slice\_x) = \sum_{\lambda=300\,nm}^{\lambda=1200nm} A(\lambda, x).\Phi(\lambda).\frac{\Delta\lambda.10^3}{d_{slice}} \quad (9)$$

  Where 10^3 is to correct the final unit of generation rate to be in [$cm^{-3}.s^{-1}$]

By integrating these optical generation rates over the whole ranges of wavelengths from 300 nm to 1200 nm, the total generation rate in a whole slice is obtained. By repeating this for all slices, a table of OG rates vs depth can be formed. Each absorber in the 3TT device produces its own table. These tables can be used in comparison with the tables produced by the other method (in section 2.4) to detect the

differences between profiles. For that purpose, the OGR profiles from the two methods were plotted together for each absorber to detect any mismatch. Also, the total optical current density of the absorber can be calculated and compared for each method in each absorber. Therefore, the margin (difference) from GenPro4 gives an indication of how accurate the method used in this project is. The results of this comparison can be seen in Figure 26 & Figure 27 for both Perovskite & c-Si absorbers respectively. The match between the two methods exceeds 99.7 %. Also notice that the error margin increases around the edges (surfaces) of the absorber slab. This is due to resolution of the slicing and meshing, since finer slices and meshing will increase resolution and thus increase accuracy and vice versa.

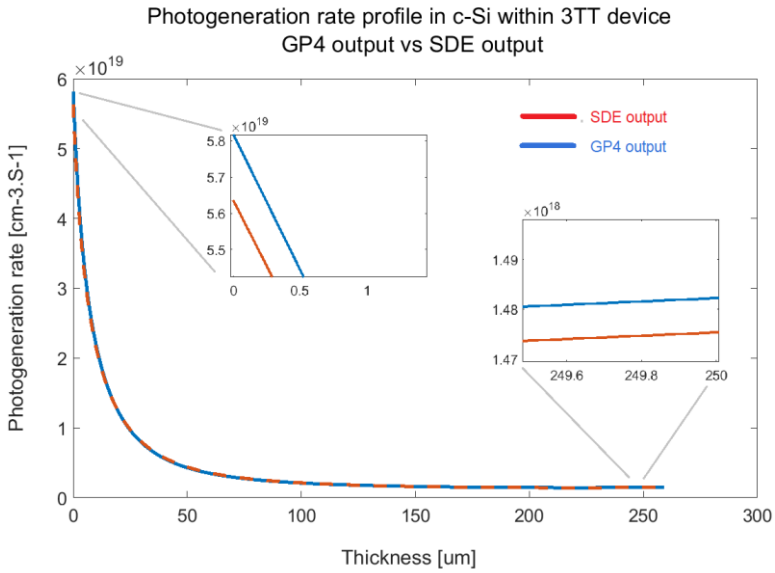

Figure 26 the match between the direct output of OGR profile from GenPro4 and the actual profile processed in Sentaurus simulation for the c-Si absorber.

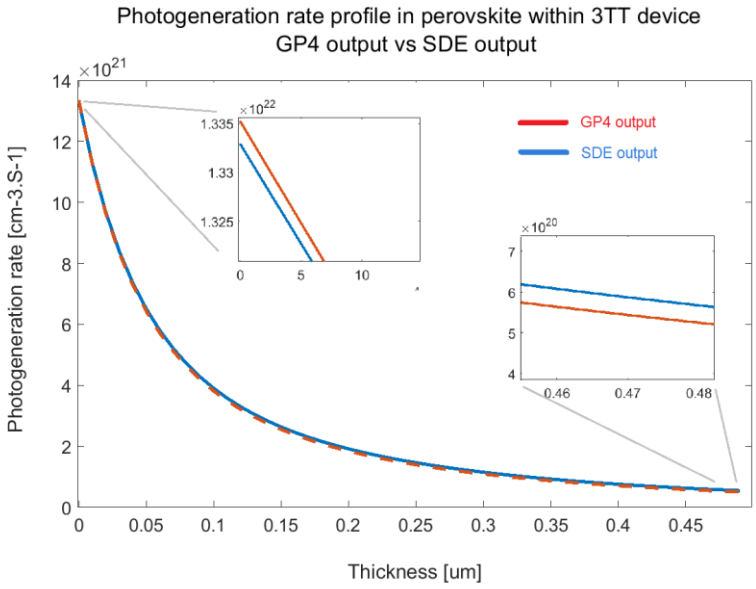

Figure 27 the match between the direct output of OGR profile from GenPro4 and the actual profile processed in Sentaurus simulation for the Perovskite absorber.

By integrating the photo generated current over the whole slab thickness, it is also found that less than 1% difference in photo current density is encountered between the two profiles. Which confirm that the room of error is significantly small. Further, the difference between the two profiles was investigated around the edges of the slab nearby interfaces between layers. The difference here is also significantly small, which indicated that these profiles provide fine precision nearby the interfaces. Which is a requirement for high resolution mesh around these inference's areas. A further refinement of the slices and mesh will increase the precision, but it will come on the cost of higher simulation time.

3.2 Electrical simulation results validation

After getting a working 3TT device template as it was shown in section 2.5, the need to validate this template is necessary to approve that the simulation results are reliable and accurate. But since, the 3TT model structure that is used in this project has no equivalent physical device or similar 3TT device measurements, direct validation is not possible. But validating the main components in the 3TT device based on logical connection with equivalent components models and cells from literature will be an acceptable approach. To do so, the sub-cells of the 3TT device were based on single junction (SJ) IBC & SJ PSC cells that have models which are previously validated. These validated models were recreated and simulated to confirm their agreement with the original models. Then, the codes of these models are used for 3T sub-cell's codes after making small modifications to them to be integrated with the 3TT device model.

3.2.1 IBC cell validation:

The bottom cell in the 3TT device is based on identical (in structure, geometry, and layer's material) reference SJ IBC model used by Procel et al. [58]. Which is validated based on a real experimental physical IBC cell made by G. Yang et al. that achieved a PCE of 21.2%? [87]. We have recreated the model of Procel et al. and removed the texture pattern from top surface to make it comparable to the bottom IBC cell used in 3T device. The model is then simulated to form a picture about the performance after these modifications. The simulation results of the SJ IBC model under AM1.5G spectrum are presented in Figure 28.

J_{SC} [mA/cm²]	37.75
V_{OC} [V]	0.715
J_{mpp} [mA/cm²]	35.77
V_{mpp} [V]	0.632
P_{mpp} [mW/cm²]	22.61
FF [-]	0.837
η [%]	22.61

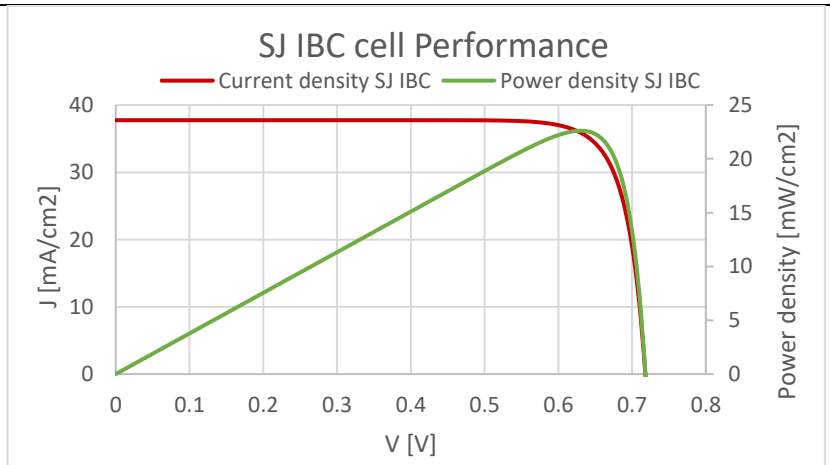

Figure 28 The simulated J-V & P-V curves of the reference SJ IBC TOPCon cell with flat top surface.

From the chart above and the table beside it, it is observed that SJ IBC with flat top surface has achieved power conversion efficiency of 22.6%. Although this is not the best efficiency for a bottom cell, but it still sufficient to be part of highly efficient tandem device.

The IBC model was then modified to be integrated in the 3TT device model. The simulation results of 3T IBC bottom cell are displayed in Figure 29.

J_{SC} [mA/cm²]	17.91
V_{OC} [V]	0.664
J_{mpp} [mA/cm²]	17.02
V_{mpp} [V]	0.576
P_{mpp} [mW/cm²]	9.80
FF [-]	0.824
η [%]	9.80

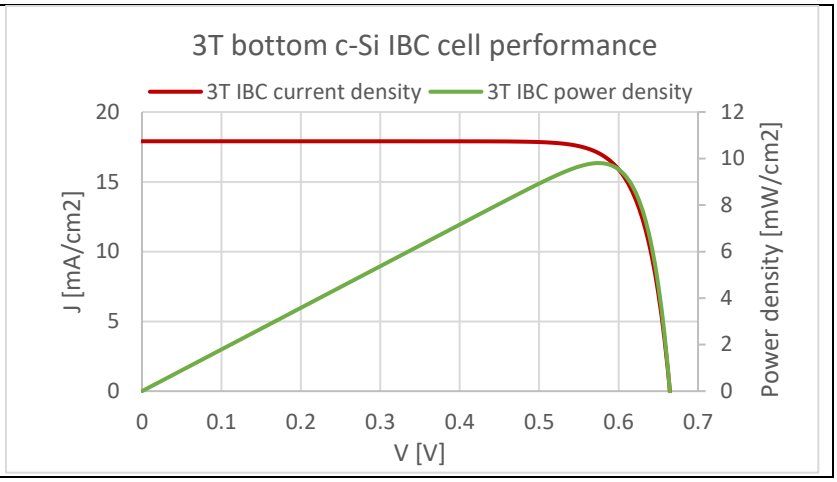

Figure 29 The simulated J-V & P-V curves of the 3T IBC bottom cell with flat top surface

In Figure 29, it is seen that the bottom cell IBC cell has lower PCE than an Identical SJ IBC, similpply because the top perovskite cell act as a filter of high energy photons which prevent a big portion of light from reaching the bottom cell. The biggest shift is seen in the SC current density which dropped from 37.7 mA/cm² in the SJ IBC to 17.91 mA/cm² in the 3T IBC cell. Also, V_{OC} & V_{mpp} experienced a small drop. Consequently, the PCE dropped from 22.61% to 9.8 %. This behavior is expected from the 3T IBC cell since most the top perovskite cell utilizes most of incident energy.

3.2.2 Perovskite cell validation

Likewise, as in the IBC bottom cell, the 3T PSC top cell model is based on a SJ PSC reference model which was validated by reference cell used by D. Yang et al. that achieved PCE of 21.6% for a planar p-i-n layout [88]. This kind of PSC with SnO2 as ETL and Spiro-OMeTAD as HTL is considered high-performance planar Perovskite cells with the best efficiency around for planer PSC so far [88]. The same model is used in the 3TT device with some modifications on some layer's thickness to optimize the 3TT device optically.

Therefore, the SJ PSC model was recreated and simulated. The outputs of the electrical simulations of this model agrees with reference model. The simulation results of the SJ IBC model under AM1.5G spectrum are presented in Figure 30.

J_{SC} [mA/cm²]	22.8
V_{OC} [V]	1.212
J_{mpp} [mA/cm²]	21.42
V_{mpp} [V]	1.04
P_{mpp} [mW/cm²]	22.79
FF [-]	0.806
η [%]	22.79

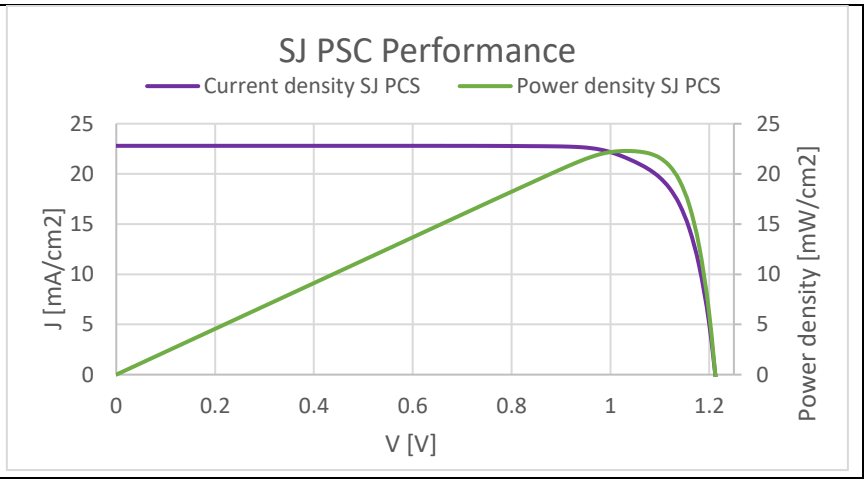

Figure 30 The simulated J-V & P-V curves of the reference SJ PSC cell.

Then the model was integrated in the 3TT device model. Next, the simulation results of 3T PSC are obtained and displayed in Figure 31.

J_{SC} [mA/cm²]	22.13
V_{OC} [V]	1.212
J_{mpp} [mA/cm²]	19.91
V_{mpp} [V]	1.02
P_{mpp} [mW/cm²]	22.31
FF [-]	0.757
η [%]	22.31

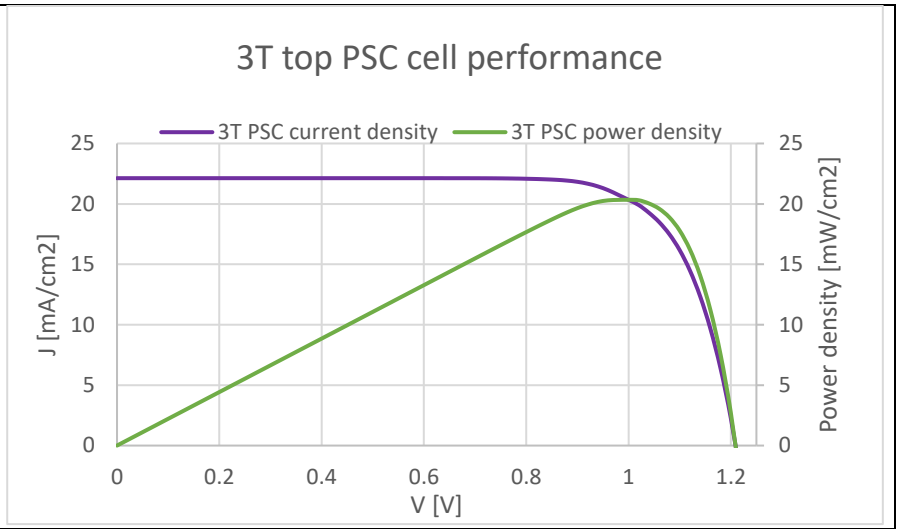

Figure 31 The simulated J-V & P-V curves of the 3T PSC cell.

It is seen from Figure 31 that the performance of the 3T PSC has also decreased compared with SJ PSC although the full spectrum hit the surface of the perovskite cell. This is because the charge carriers in created by the top cell are constrained in the flow by the presence of the bottom cell. For example, electrons that are created at top cell will travel longer distance to the rear contact of the bottom cell to be collected. Which means that they will suffer from higher resistance and recombination losses.

However, the PSC drop of performance is lower than the drop of the IBC cell, Simply, because the 3T PSC still receive the full spectrum of light while the 3T IBC receives only what was not reflected or absorbed by the PSC top cell.

3.3 The 3TT device vs 4TT device

The goal of this section is to evaluate how efficient is our proposed 3TT model in comparison with other tandem configurations such as 4TT device. This comparison will enable us to judge whether a 3TT device, in general, is worth investment and research in term of efficiency, complexity, and cost. Further, it can tell us how competitive this 3TT model (that is adopted in this project) is with an equivalent 4TT model.

To answer these inquiries, a 4TT model need to be built and simulated. the model should be identical in structure, parameters, thicknesses, layer's order, and layer's material to the 3TT model with the exception that the 4TT will have additional one ITO layer at the rear of the top cell and a physical transparent gap between the sub-cells. The table below summarizes the layers and thicknesses of both 3TT and 4TT models:

Table 4 A summary of material choces and thicknesses of both 3TT & 4TT models

3TT model			4TT model		
layer	material	thickness	layer	material	thickness
ARC	SiO2	85 nm	ARC	SiO2	85 nm
Front top contact1	Silver	300 nm	Front top contact1	Silver	300 nm
HTL	Spiro-OMeTAD	40 nm	HTL	Spiro-OMeTAD	40 nm
Absorber1	MAPbI3	500 nm	Absorber1	MAPbI3	500 nm
ETL	SnO_2	40 nm	ETL	SnO_2	40 nm
---	---	---	TCO	ITO	40 nm
---	---	---	Back top contact2		300 nm
---	---	---	Middle Isolation	EVA	400 µm
FSF_IBC	PolySi(n+)	20 nm	FSF_IBC	PolySi(n+)	20 nm
Absorber2	c-Si	260 µm	Absorber2	c-Si	260 µm
Tunneling layer	SiO_2	1.5 nm	Tunneling layer	SiO_2	1.5 nm
Passivating contacts	PolySi(n+)/(p+)	10 nm	Passivating contacts	PolySi(n+)/(p+)	10 nm
Rear metal contacts	Silver	5 µm	Rear metal contacts	Silver	5 µm

The correspondent structure schematics for both models are displayed in the following Figure 32:

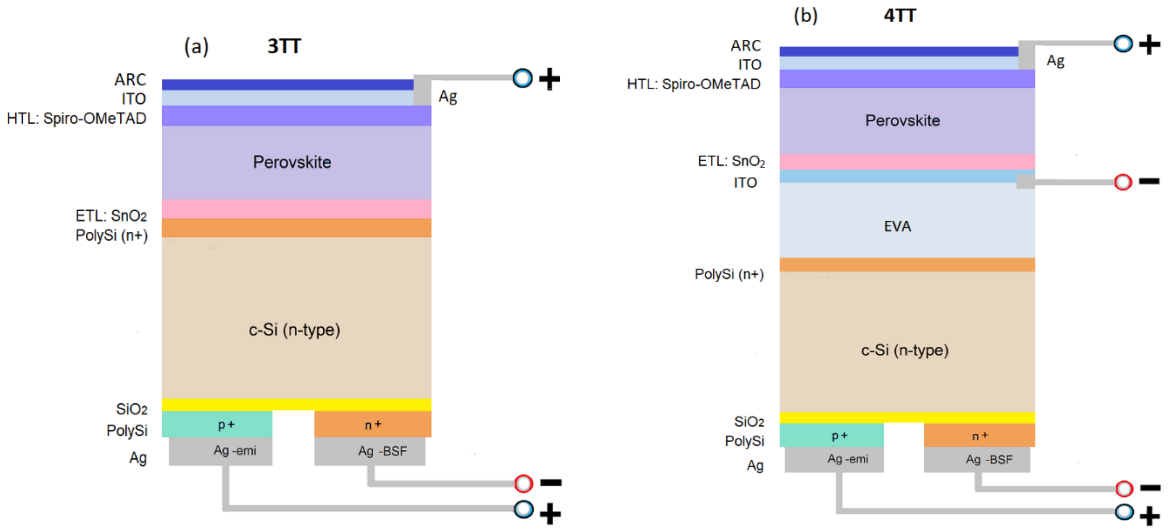

Figure 32 schematic diagram (not to scale) of (a) 3TT PSC/c-Si IBC model (b) 4TT PSC/c-Si IBC c-Si model.

It is worth mentioning that the used structure here for both models is meant to deliver an initial basic functional device structure without additional optimization. Thus, the models don't have additional ARC layers (only single coating of SiO_2 is used). Neither they have any extra texture that utilize more light. In reality, a 4TT device will have an extra glass substrate where the top cell is deposited on. But in this proposed model, such a layer is removed to make the comparison with 3TT device more just. Therefore, these models are meant for basic comparison and not advanced compression since this will be out of the scope of this project.

The main difference between the two structures is the extra ITO contact layer at the back of top cell and the transparent isolation layer in the 4TT model. This layer is chosen from an ethyl-vinyl acetate (EVA) matrix with a thickness of 450 µm based on literature data [89]. The purpose of this layer is to

guarantee that no current or charge carriers can be exchanged between the two sub-cells. Therefore, the two cells will operate separately.

After building the models by Sentaurus TCAD and performing opto-electrical simulations, the electrical simulation's results for these two models are summarized and displayed in the following two figures:

J_{SC_IBC} [mA/cm²]	14.93
J_{SC_PSC} [mA/cm²]	22.69
V_{OC_IBC} [V]	0.692
V_{OC_PSC} [V]	1.208
J_{mpp_IBC} [mA/cm²]	14.15
J_{mpp_PSC} [mA/cm²]	21.35
V_{mpp_IBC} [V]	0.600
V_{mpp_PSC} [V]	1.040
FF_IBC [-]	0.822
FF_PSC [-]	0.809
η_IBC [%]	8.49
η_PSC [%]	22.20
η_3TT [%]	30.69

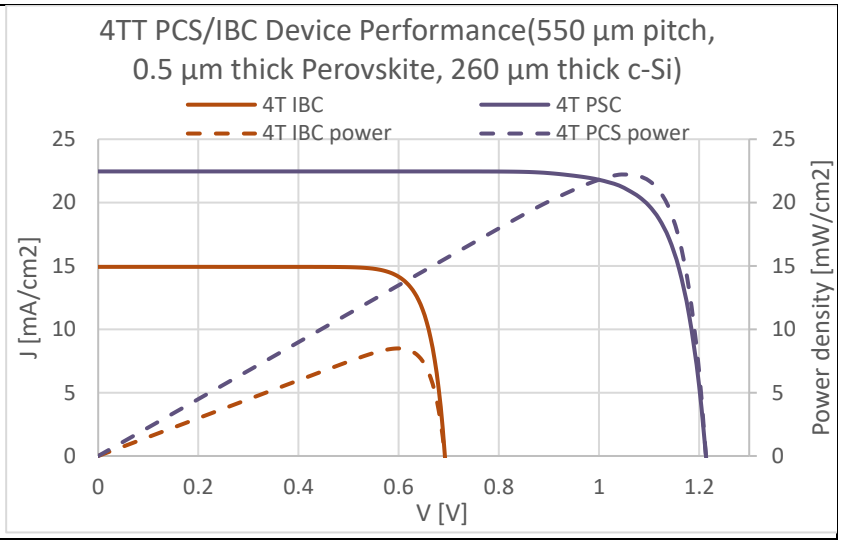

Figure 33 The simulated J-V & P-V curves of the basic 4TT PSC/c-Si IBC model with flat top surface.

J_{SC_IBC} [mA/cm²]	17.91
J_{SC_PSC} [mA/cm²]	22.13
V_{OC_IBC} [V]	0.665
V_{OC_PSC} [V]	1.205
J_{mpp_IBC} [mA/cm²]	17.03
J_{mpp_PSC} [mA/cm²]	20.08
V_{mpp_IBC} [V]	0.576
V_{mpp_PSC} [V]	1.02
FF_IBC [-]	0.824
FF_PSC [-]	0.768
η_IBC [%]	9.81
η_PSC [%]	20.48
η_3TT [%]	30.38

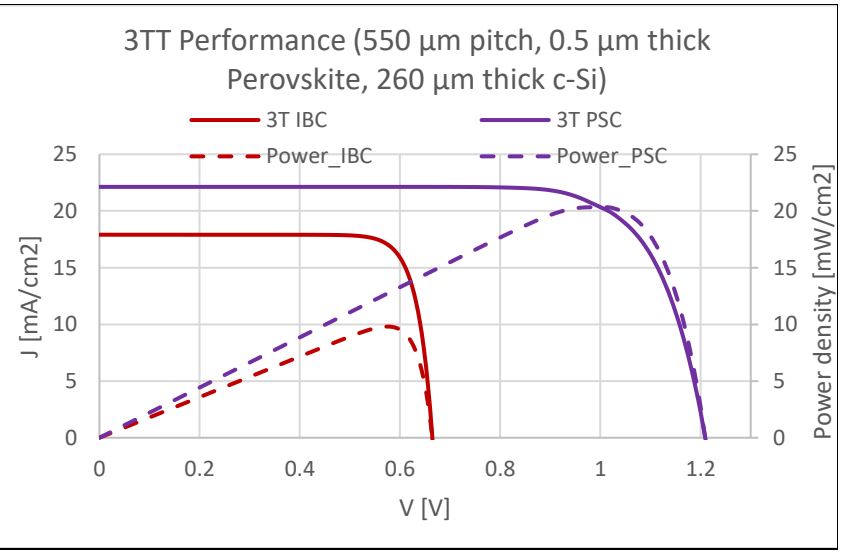

Figure 34 The simulated J-V & P-V curves of the basic 3TT PSC/c-Si IBC model with flat top surface.

Figure 33 & Figure 34 represent the J-V & P-V curves for the 4TT & 3TT models respectively. From the results, it is noticed that the top cell in 4TT device is behaving similar to the SJ PSC, since it is operating without constraints from the bottom cell. While in the 3TT device, the top cell current is influenced (but not significantly) by the bottom cell current, which lowers the contribution of the 3T PSC compared with that of 4T PSC. By the same token, both V_{OC} & V_{mpp} of the bottom cell in 4TT are higher than their correspondent in the 3TT device. However, the 4TT model will suffers from extra parasitic losses in the bottom cell (for low energy photons) caused by the additional middle EVA and ITO layers. Since considerable portion of low energy light will be absorbed by these layers which will lower the received light by the bottom cell and consequently will lead to a lower energy yield. On the other hand, 3TT model eliminates these parasitic losses. Therefore, it has higher total current density, but it suffers from a reduced V_{mpp} in the bottom IBC cell which will lower the efficiency of the bottom cell. So, it can be

said that both models show high performance larger than the 30% PCE parity even when advanced optimization and enhancement are not used.

But from manufacturing point of view, the 4TT will be easier to fabricate on a cell level because each sub-cell can be built separately and brought together mechanically. This adds extra level of freedom in fabrication conditions and techniques. Which leads to more choices and cheaper feasible options. On the other hand, the 3TT device is more complex to fabricate since the whole device need to be produced from bottom to top monolithically without causing damage or changes in properties to the prior deposited layers. This makes the fabrication techniques limited in choices and causes the fabrication conditions to be tricky and critical. Which could add to the costs and complexity of fabrication. However, these 3TT devices cost cheaper on a module level, since they have less terminals which exist on the top and bottom of the device only, not in the middle. And that leads to a reduced balance of the system (BOS) costs. To sum it up, both 3TT & 4TT devices have their advantages and disadvantages when it comes to fabrication costs and complexity. Which makes judgment hard to reach from a researcher perspective but more relevant if it is assisted by industrial or commercial perspective.

3.4 Conclusion

The aim of this chapter was to validate the created 3TT device model and compare its performance with other tandem configuration's performance. This has been done firstly by confirming the accuracy of the optical simulation of the model. We successfully showed the reliability of the applied 2-D optical generation rate profiles in SDE tool. And how the optical inputs in Sentuarus agrees with the optical outputs from GenPro4. Furthermore, the electrical stimulation in both the IBC bottom cell and the PSC top cells were validated by their correspondent reference SJ cells. This was based on literature data as well as on previously validated models for SJ cells. These models were recreated and modified to imitate identical structure and parameters for the 3TT proposed device.

Additionally, the performance of the basic 3TT model was compared with its equivalent 4TT model. This required building a 4TT PSC/c-Si IBC model which share identical structure and properties to that of 3TT model except for the two extra layers in between the sub-cells. The comparison revealed that both models show high capacity to achieve high efficiency (30.38%, 30.69% for 3TT, 4TT models respectively) with some differences on how their perform. It can be concluded that both devices are efficient and have independent sub-cells' operation. Further, it was found that the 3TT device is more efficient in reducing parasitic losses. However, the 4TT device can compensate for the parasitic losses by including extra pattern of texture at the top surface of the IBC cell and/or extra ARC which reduces reflection by the bottom cell significantly. While this extra texture is still difficult to realize in 3TT devices since a flat top surface at the bottom cell is necessary to uncomplicate the fabrication process. Finally, it is concluded that both 3TT & 4TT devices have their pros and cons when it comes to fabrication costs and complexity which can be preferably assisted by industry itself.

It is worth mentioning that 4TT & 3TT devices can obtain even higher PCE if more means of optimizations are applied. The focus of this project will be enhancing the 3TT device's performance by some of these means. Which will be discussed in detail in the next chapter.

4 Optimization of 3TT Efficiency

By looking at the initial obtained results from the 3TT device's template in the previous chapter, our proposed 3TT device shows high efficiency potential that need further optimization to exceed the parity of 30% PCE. Which is one of the main targets of this project. Therefore, the aim of this chapter is to redesign parameters of Perovskite top cell (layer's thickness) and the architecture of c-Si IBC bottom cell (pitch and emitter/base ratio) to optimize the proposed 3TT model to achieve higher efficiency than that of the basic model. Section 4.1 study the effect of changing the thickness of Perovskite layer and optimize the model accordingly. While section 4.2 investigates the effect of changing the pitch width on the performance of the bottom IBC cell and the whole 3TT device. Further, in section 4.3, the ratio between emitter width & base width in the IBC bottom cell is optimized to improve outputs of the whole 3TT device. In section 4.4, several scenarios are nominated based on the previous optimizations. These scenarios represent the best performing models that have some flexibility in the chosen pitch and emitter/base ratio. Then in section 4.5, a full 2D performance map of the 3TT device is made based on the best scenario outputs, which aid understanding the operation of 3TT device on cell level as well as on a module level. And finally, section 4.6 studies the performance in one case of best scenarios when the device have/not surface recombination active.

4.1 Optimizing the thickness of perovskite layer

The initial proposed 3TT model has used a value of 0.5 µm thick perovskite absorber layer. But this value was based on a SJ PSC reference cell [74]. Therefore, it is necessary to optimize the perovskite thickness according to our 3TT model. Consequently, the thickness of perovskite layer was changed from 0.1 µm to 5 µm. This required substantial adjustment to the code for each thickness. Which included not only changing the thickness of the layer but also refining the optical simulation and adjusting the mesh in SDE tool accordingly. Thus, for each thickness, a unique 3TT model was created, optimized optically, and simulated in Sentuarus. The thickness span was changed in small increments (= 0.1 µm) from 0.1 to 1.5 µm. Then the increment size was increased to 1 µm step from 2 to 5 µm thickness to reduce simulation time. The results of these simulations are summarized in the following chart:

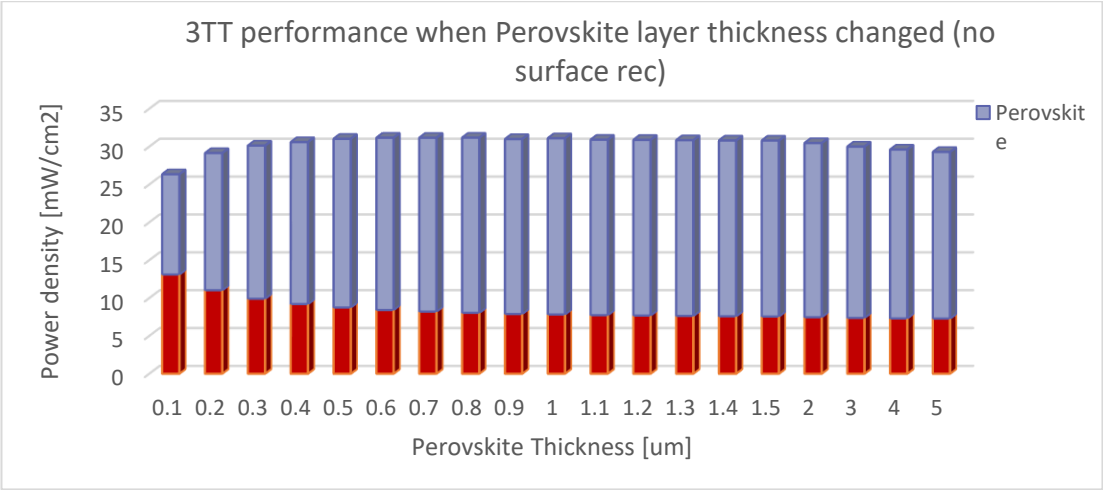

Figure 35 The performance of both top and bottom sub-cells in the 3TT PSC/c-Si IBC model when the Perovskite absorber layer's thickness is changed.

Figure 35 displays the performance of 3TT device when the Perovskite absorber layers is changed in thickness. From the chart, it is seen that the power contribution of the top cell increases when the perovskite thickness increases until it saturates around the thickness of 1 um then starts to decrease slowly when larger thicknesses are applied. On the other hand, the bottom IBC cell contribution decreases when the Perovskite layer is thicker, and it continues to decrease until the end of the span. This is due to higher absorption of light by the perovskite layer when it is thicker which let less photon flux to pass to the c-Si. In addition to that, the top cell becomes less transparent when the perovskite layer is thicker.

Furthermore, it is observed that the total power produced by the 3TT device also increases with the increasing perovskite thickness until it saturates between thickness of 0.5 to 1,2 µm. After that it starts decreasing when perovskite thickness increases. This can be explained by the stronger influence of Perovskite top cell. This influence is more visible at small thicknesses in perovskite layer since a change in thickness means utilizing more photons by the top cell and less photons reaches the bottom IBC cell. But due to the higher V_{OC} and V_{mpp} of PSC compared with those of the IBC cell, the gain in power production by the top cell is bigger than the reduction of power at the bottom cell. However, this influence begins to be less effective and saturates when the increasing of power produced by the perovskite is matched by a decreasing of power by c-Si. Therefore, the net total produced power density by the tandem device will not improve. And when the thickness is increased even further, more parasitic absorption occurs by the perovskite layer. Which means less high energy light is left to be utilized and more is blocked to pass to the c-Si layer. In addition to that, the bulk resistance of Perovskite layer increases. That leads to a noticeable decrease in the 3TT device performance when the perovskite layer has higher thicknesses > 1.5 µm.

Based on the simulations which was performed. It is found that the highest 3TT device performance happens when the thickness of perovskite layer is in between 0.8 – 0.9 µm where the PCE is higher than 31 %. For further optimizations in this project, we will consider the thickness of Perovskite absorber layer as 0.8 µm.

4.2 Pitch optimization

As it was stated in the first chapter, the one of the core objectives of this research is to redesign the cross-sectional geometry of c-Si IBC cell to be more suitable for 3TT device. Several geometrical parameters play a role in the IBC geometry but the focus in this section and the next section will be on the pitch and emitter/base ratio parameters respectively. The target of these optimizations will be to investigate which pitch and emitter/base ratio values deliver higher performance not only to the 3T IBC bottom cell but also to the whole 3TT device.

4.2.1 Optimizing approach

As it was discussed in section 1.3, It is well known that the smaller the pitch value is in SJ IBC cell, the higher the performance becomes. Because this allows the IBC cell to collect more carriers with less recombination losses. But very small pitches are challenging and more costly for fabrication. That is why the intention is to have as large pitch as possible to suit fabrication needs without losing significant power production. Thus, it is a tradeoff between high efficiency and lower costs and complexity [16]. But similar assumption cannot be generalized on three terminal tandem devices since it has more complex current flow mechanism. Therefore, pitch need to be investigated for different values and the relation between power conversion efficiency and the size of pitch needs first to be studied. Afterward a conclusion can be drawn about which values show better outcome.

In our 3TT model, the initial pitch was set to be 550 µm, while the emitter/base width's ratio was selected to be 1.5:1 or (60% to 40%) of the pitch value. The following graph (Figure 36) displays a schematics vertical cross section of the 3TT device and besides it a horizontal cross section of the back of the bottom IBC cell showing the pattern of emitter and base busbars and defining the pitch which is the distance between the middle of two contact fingers of the same polarity.

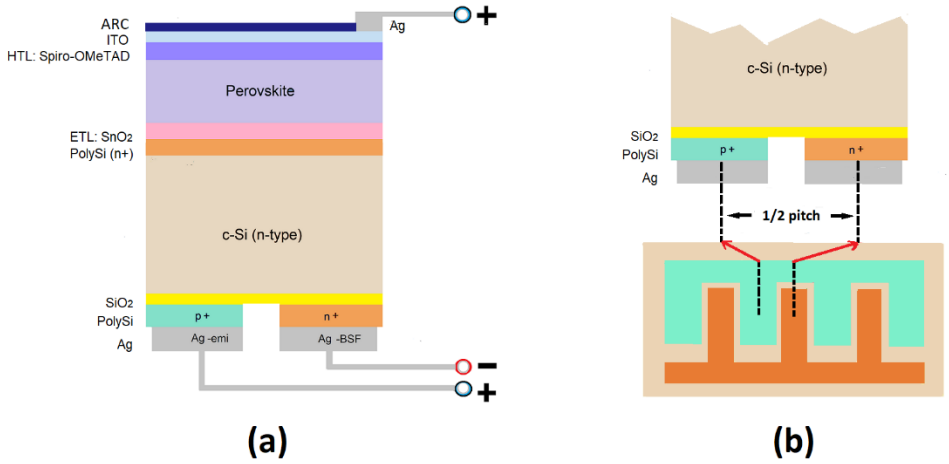

Figure 36 displays (a) a schematics vertical cross section of the proposed 3TT device unit cell (b) a horizontal cross section of the back of this device showing the pattern of emitter and base busbars.

Our approach in optimizing the pitch is to start with the SJ IBC cell by increasing the pitch incrementally in it from (50 µm) and up to 5 mm. At the same time, the same ratio between base and emitter widths should be fixed, which is 60% to 40% respectively. Then the performance of the cell is observed. A plot between power production vs pitch length is needed to optimize the pitch based on performance and industrial requirements.

The next step is to repeat the same procedures for the bottom IBC cell in the 3TT device. In this case, changing the pitch won't only influence the performance of the IBC cell but also the perovskite top cell, since the charge carrier's collection at the rear terminals is connected to the third top terminal. Thus, we look not only on the IBC performance to determine the optimum pitch but also on the whole 3TT performance under different pitch's values.

To carry out the electrical simulations for different pitch values the device geometry and the mesh in the SDE tool need to be adjusted according to each pitch value to sustain the same back contacts ratio and mesh resolution.

4.2.2 Pitch optimizing results and analysis

After performing the aforementioned simulations, the results are used to compare between the power conversion vs pitch value in the SJ IBC cell, 3T IBC bottom cell, PSC top cell, and 3TT device. The following plot (Figure 37) displays these comparison's curve.

Based on the result and curves in Figure 37, it can be said that the PCE show the same trend for all cells where PCE decreases when the pitch increases. Thus, it can be concluded that the finer the pitch is. the more power can be converted in 3TT device and in its component cells. It is also observed that the peak performance of all cells is at low pitch values (below 500 µm) where PCE for the 3TT model is higher than 31.2 % and can sustain more than 99% of the highest possible efficiency.

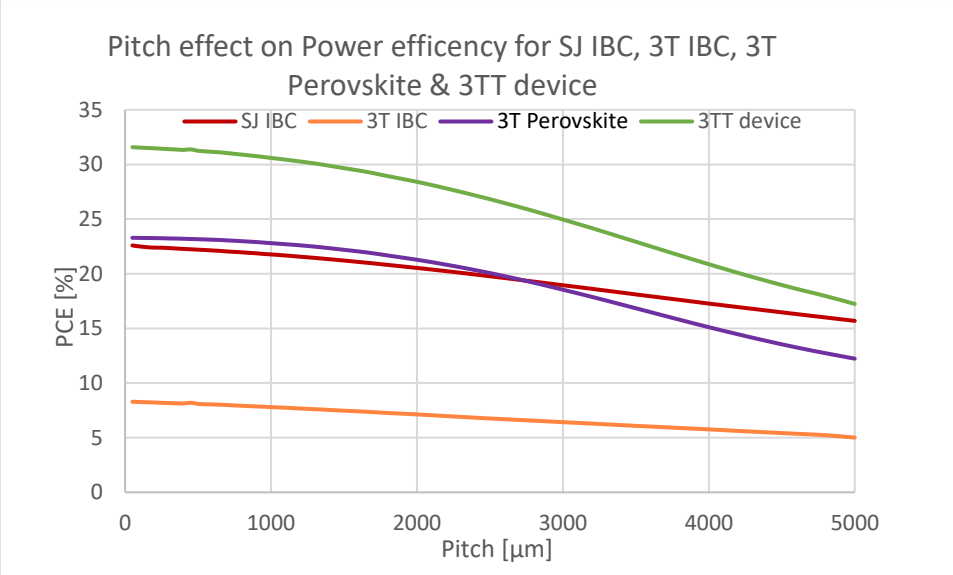

Figure 37 The effect of changing the pitch value in 3T IBC bottom cell on the tandem performance.

Furthermore, it is noticed that the behavior of PCE-curve in the PSC is distinguishes from that behavior of the curve in SJ IBC or 3T IBC cells. Where the PCE vs pitch value seems to decrease in steeper trend than the IBC cell. For example, when the pitch change from 100 µm to 5000 µm, the SJ IBC losses about ~ 30 % of its power production in almost a linear decreasing trend. Similarly, the 3T IBC losses about 37% of its power production in similar way. On the other hand, When the pitch value is increased to 5000 µm, the 3T PSC sub-cell will loss ~48% of its efficiency in a more parabolic fashion. Which influence the behavior of the whole 3TT device heavily. This can be explained by the fact that the current flow in the PSC is dependent on the top terminal and the rear back base terminal in the IBC bottom cell. When the pitch value in the IBC bottom cell is increased, the base contact is increased as well, while the front top PSC contact will stay with the same value. Therefore, both not only the pitch of the PSC will increase but also the emitter to base ratio for the top cell will decrease causing electrical shade losses. Which will cause sharper decrease in the PSC efficiency when pitch is increased compared to the decrease in the IBC efficiency.

Thus, it is clearly seen that the effect of changing the pitch value in the 3TT device doesn't have impact only on the IBC bottom cell, but it has even greater impact on the top perovskite cell as well as on the 3TT device. Consequently, we can conclude that the 3TT device is more sensitive to pitch value than the SJ IBC cell. Thus, it is recommended to redesign the 3T IBC to a finer pitch in order to harvest more power. But this also needs to be optimized according to fabrication costs and industrial priorities. The scope of this project doesn't allow for this kind of analysis. But the result which was obtained here delivers indications on how to produce higher performance tandem cells.

4.3 Base/emitter ratio optimizing

Similar to the pitch, the emitter/base ratio in the IBC cell also plays important role on influencing the collection of charge carriers as well as influencing the fabrication costs. For example, a neutral ratio (1:1) is more cost effective and easier to fabricate but it doesn't necessarily yield better power conversion since a wider base will cause electrical shade which reduces the collected current [90]. Thus, a higher emitter width ratio to the base is better from the perspective of power generation. As it

was discussed in section 1.3, the best design ratio between emitter to base passivating contacts for a SJ IBC cell is 3:1 [91]. But for 3TT device, this ratio may not be the optimum ratio. That is why it is necessary to investigate it for our model.

The approach which is used in optimizing the emitter/base ratio is similar to that used for optimizing the pitch. But the difference here is fixing the pitch at a value of 550 µm and changing the emitter to base ratio from 1:20 to 20:1. The obtained results from these simulations are shown in Figure 38:

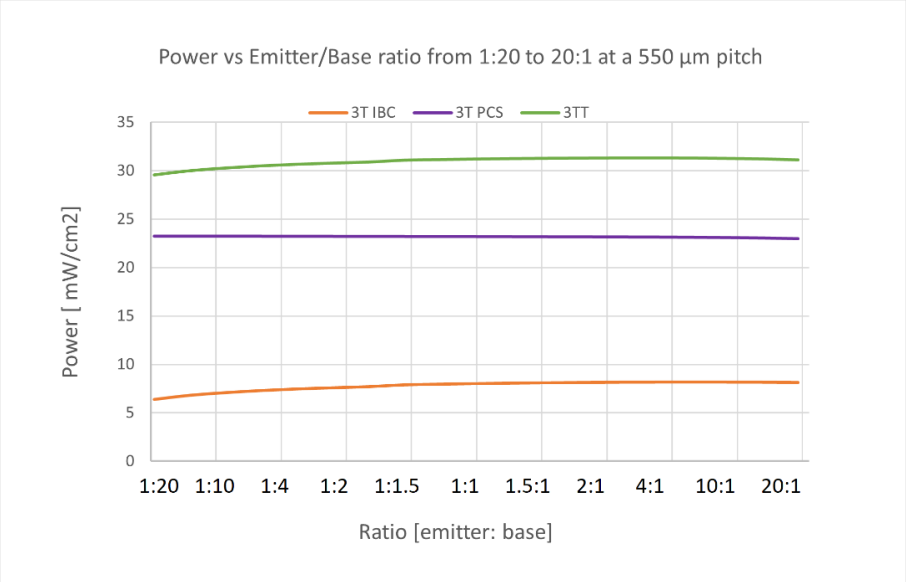

Figure 38 Power efficiency when the emitter to base ratio is changed from 1:20 to 20:1

It is observed that the power efficiency of the bottom IBC cell is low when the emitter width is smaller than the base width. While the efficiency saturates when the ratio exceeds 1.5:1. On the other hand, the top PSC cell seems to be little effected by the change of the ratio. In general, the 3TT device has its peak performance between the ratio of 1.5:1 to 4:1.

Although the ratio appears to influence the efficiency of the device, but so far, the ratio doesn't show a significant effect on the performance of the 3TT device. The reason could be that the pitch value is near or smaller than the range of the diffusion length of minority carriers in the bulk c-Si material which is ~900 µm based on the parameters used in for this model. Thus, no matter what the ratio is, the distance that the generated minority carriers need to travel stay within acceptable range (i.e., recombination stay small). That is why it was decided to carry out another simulation experiment with a bigger pitch value to investigate whether the aforementioned argument is true or not.

In the new scenario, the pitch is set to be at value of 5000 µm, while the emitter to base ratio is changed from 1:20 to 20:1. In this way, the variation of ratio will result in emitter and base widths big enough to confront the diffusion length limit. The electrical simulation results are then obtained for each ratio and displayed as a function of power density vs the ratio as shown in Figure 39:

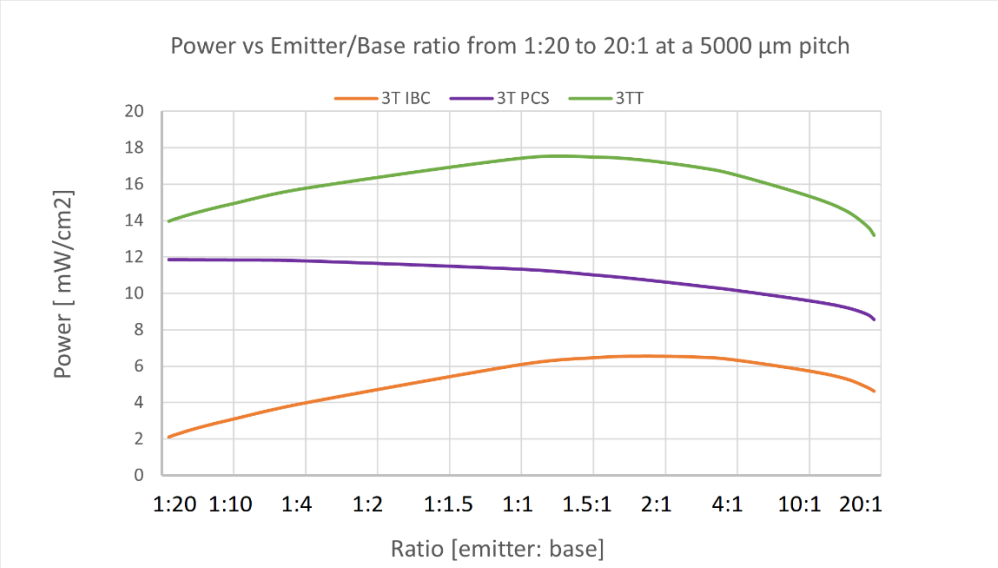

Figure 39 Power efficiency when the emitter to base ratio is changed from 1:20 to 20:1.

Here, it can be seen that a substantial change in the behavior of power density is detected when the ratio is changed. To begin with, the IBC bottom cell efficiency has almost increased by 300% when the ratio changed from 1:20 to 2:1. Then it decreased by almost 40% when ratio changed from 2:1 to 20:1. Meanwhile, the PSC top cell, which showed nearly no change in the previous experiment, now is showing a continuous decrease in the efficiency as long as the emitter width is increasing. Finally, the 3TT device efficiency behavior is a summation of both sub-cells' behavior. Where it decreases at the extreme ratios and peaks at the middle ratios. the peak performance is detected between the 1:1 and 2:1 ratio.

The result of this experiment proves that when the pitch value is bigger than the diffusion length of the bulk material, the emitter/base ratio has much greater influence on collecting the charge carriers at the terminals. Where the holes (electrons) have to travel longer distances if the (emitter) base width is small. Which will lead to bigger chance of recombination and thus a drop in the collected current.

Overall, it can be concluded that if the Pitch value is small, changing the emitter/base ratio has no significant impact on the conversion efficiency of the 3TT device. This feature of the ratio can be very beneficial in reducing manufacturing costs of the IBC cell, since the ratio can be adjusted to the most cost-effective ratio without noticeable reduction in the efficiency of the solar cell. On the other hand, If the pitch value is large, which reduces the costs and complexity of fabrication significantly, the emitter/base ratio can be very effective in improving the efficiency of the cell. That is why it is recommended to optimize the emitter/ratio in combination with optimizing the pitch to balance between cost and efficiency.

4.4 Best Scenario's optimization

In the previous sections of this chapter, different optimization approaches of the 3TT model have been applied successfully. However, this section will focus on how to bring the best outcomes of these optimization techniques combined. And offer several scenarios where the 3TT model can achieve the highest efficiency but with more design's parameter choices.

There are many scenarios that can be created for high efficiency model, but the choices were narrowed down to four scenarios that seem to be most interesting. These scenarios were based on best combination between Perovskite thickness, pitch value and emitter/base ratio. This is helpful from industrial point of view since we could optimize the thickness and emitter/base ratio to produce models with different pitch values but almost with similar efficiencies and performance. The selected Perovskite layer thickness in all these scenarios is chosen to be 0.8 µm since it has the potential for best efficiency according to the optimization which was done in section 4.2. Furthermore, the selected pitch values are 200, 300, 400, 500 µm with emitter/base ratio 2:1, 2:1, 4:1, 3:1 respectively. The geometry parameters and simulation results of these scenarios are summarized in the following table:

Table 5 Summary of best scenarios parameters and their opto-electrical simulation's outcomes

		Scenario1	Scenario2	Scenario3	Scenario4
Geometry	Unit	Value	Value	Value	Value
Pitch	[µm]	200	300	400	500
Emitter width	[µm]	135	195	310	370
Base width	[µm]	65	95	80	120
Gap	[µm]	10	10	10	10
Perovskite layer thickness	[µm]	0.8	0.8	0.7	0.8
c-Si layer thickness	[µm]	260	260	260	260
Emitter/Base ratio		2:1	2:1	4:1	3:1
3TT outcome					
$J_{ph\ IBC}$	[mA/cm²]	16.97	16.95	16.95	16.95
$J_{ph\ PSC}$	[mA/cm²]	23.65	23.65	23.65	23.65
$V_{OC\ IBC}$	[mV]	0.660	0.659	0.658	0.662
$V_{OC\ PSC}$	[mV]	1.184	1.185	1.183	1.183
$J_{SC\ IBC}$	[mA/cm²]	16.70	16.64	16.67	16.65
$J_{SC\ PSC}$	[mA/cm²]	23.64	23.64	23.64	23.64
$V_{mpp\ IBC}$	[mV]	0.568	0.568	0.576	0.576
$V_{mpp\ PSC}$	[mV]	1.02	1.00	1.00	1.00
$J_{mpp\ IBC}$	[mA/cm²]	15.87	15.91	15.75	15.76
$J_{mpp\ PSC}$	[mA/cm²]	22.28	22.62	22.60	22.54
FF_{IBC}	[-]	0.827	0.814	0.823	0.822
FF_{PSC}	[-]	0.811	0.808	0.808	0.807
IBC P_{mpp}	[mW/cm²]	9.01	9.03	9.07	9.08
PSC P_{mpp}	[mW/cm²]	22.73	22.62	22.60	22.54
3TT P_{mpp}	[mW/cm²]	31.74	31.65	31.67	31.63
H_3TT	[%]	31.74 %	31.65%	31.67 %	31.62 %

Based on the results, we were able to create 3TT models with different pitch values and emitter/base ratios but almost with similar efficiencies and performance. The results show that a relatively bigger pitch values such as 500 µm still can be used and achieve high performance similar to that when using a pitch value of 200 µm. This was possible by adjusting the emitter/base ratio. Such approach is helpful from industrial point of view since we could create alternative models with almost the same performance but yet could differ in fabricating costs. Which model is cheaper or easer to obtain can be decided by the industry itself based on the techniques they use. But we offered different design's parameters with the best outcomes.

4.5 Full Performance map of optimized 3TT device

Now after optimizing the proposed 3TT model and selecting the best scenarios, the next step is to create a surface power-Voltage (P-V) map of the optimized model. Which is necessary to track the performance of the 3TT device at any operational voltage of each sub-cell. However, most research which was done on 3TT devices has used a more simplified method to detect the performance using limiting modes that help identifying the contribution of each sub-cell at limiting conditions. The first limiting mode is the IBC mode, where no current is collected by p2-contact, and current collected between n-&p-contacts only. While the other mode is the FB (front back) mode where no current is collected from the back p-contact and current collected between n-&p2-contacts only, which allows the cell to work as a selective back junction device [46]. This enables to view the performance in simple J-V curves (line not surface). But it should be noticed that this does not show the performance at any operation condition.

Thus, to be able to describe the 3TT device in all operation conditions, a surface plot of the P-V curve is needed. This can be realized by showing the behavior of total 3TT power vs the two sub-cells voltages in one plot. Such a plot is realized in S.device by sweeping the front top contact and back emitter contact at different voltages ranges to extract the values of power production of the PSC top cell and the IBC bottom cell at different operating voltages. The sweeping is done incrementally with the equal voltage steps until the V_{OC} of correspondent sub-circuit is reached. Then the power is calculated at each point of voltage for both sub-cells. Subsequently, the generated data points are arranged in a m x n matrix, where n is the number of data points generated by the IBC cell, and m is the number of data points generated by the perovskite cell. The ijth element of that matrix represents the summation of the ith power and the jth power corresponds to the V_i in the IBC cell and V_j in the perovskite cell respectively. Then, this matrix used is to produce a contour plot which covers the power of the 3TT device at any given operating voltage for either sub-cell. The contour plot is displayed in Figure 40.

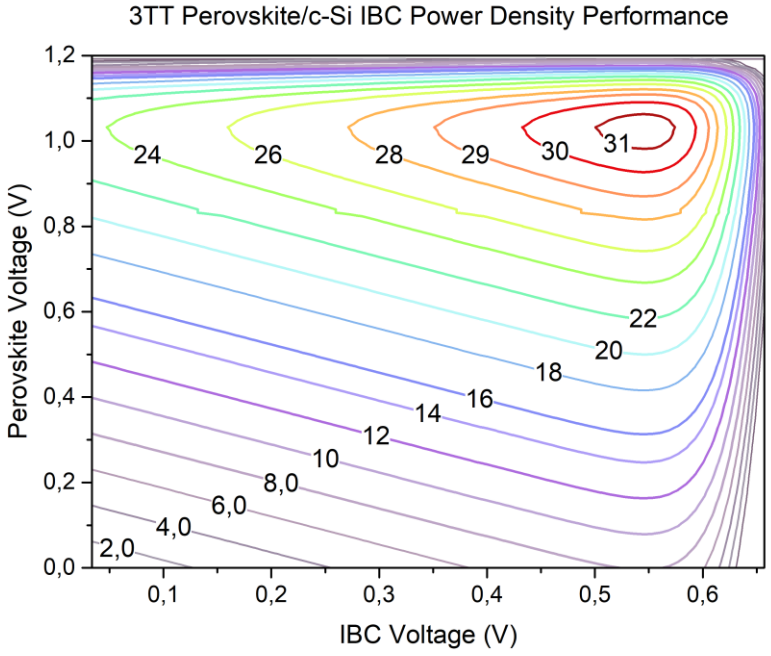

Figure 40 The 3TT P-V surface map, the contour lines represent the 3TT device's power density as a function of IBC & PSC operating voltages under STC illumination.

4.6 Reducing the surface recombination

In the previous simulations, the 3TT model has counted for surface recombination between all layer's interfaces. But since the surface recombination can be affected by several factors such as the material choice, doping concentration, bandgap energy, and fabrication condition. This can lead to a changeable effect of the surface recombination on the performance of the tandem device which can be altered and controlled by the lab or industry. Therefore, it worth to investigate the performance of our 3TT model for the ideal case when the surface recombination losses are negligible and therefore can be excluded. To so, one of the best scenarios (in this case the scenario of 200 um pitch and 2:1 emitter/base ratio) is adjusted for the new conditions of ideal surface recombination and re-simulated. the results are shown in the following table/figure.

Table 6 The best scenarios opto-electrical simulation's outcomes when surface recombination is neglected

3TT outcome	Unit	Value
$J_{ph\ IBC}$	[mA/cm²]	16.97
$J_{ph\ PSC}$	[mA/cm²]	23.65
$V_{OC\ IBC}$	[mV]	0.665
$V_{OC\ PSC}$	[mV]	1.182
$J_{SC\ IBC}$	[mA/cm²]	16.73
$J_{SC\ PSC}$	[mA/cm²]	23.64
$V_{mpp\ IBC}$	[mV]	0.583
$V_{mpp\ PSC}$	[mV]	1.05
$J_{mpp\ IBC}$	[mA/cm²]	15.88
$J_{mpp\ PSC}$	[mA/cm²]	22.93
FF_{IBC}	[-]	0.832
FF_{PSC}	[-]	0.861
IBC P_{mpp}	[mW/cm²]	9.26
PSC P_{mpp}	[mW/cm²]	24.07
3TT P_{mpp}	[mW/cm²]	33.33
η_3TT	[%]	33.33 %

It can be noticed that after suppressing the surface recombination, the generated current in both sub-cells has improved. But the improvement is more significant in the perovskite top cell where the filling factor changed from 0.811 to 0.861 almost 6% improvement. Based on the simulation outcomes of the 3TT model and the analysis used to assist them, it is believed that the largest source of surface recombination losses is coming from the interfaces between the perovskite layer and ETL & HTL layers. Thus, if these can be improved in the future research, this could very likely enable producing a 3TT device which is capable of a PCE higher than 33%.

Similar to what was done in section 4.6, a contour plot for the full operation of the 3TT model under these new conditions was created. The plot can be seen in Figure 41.

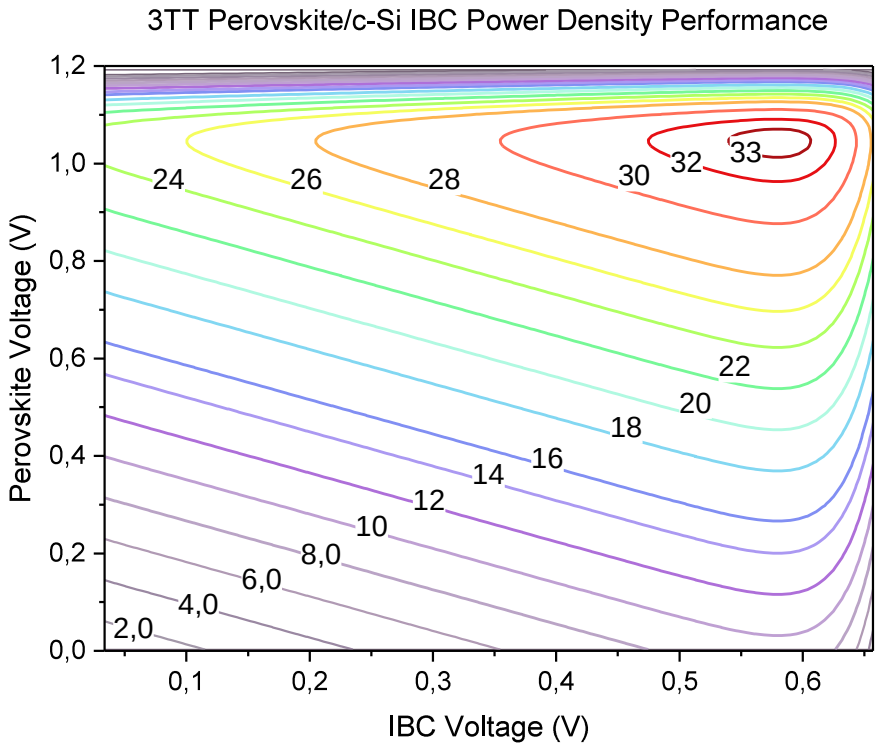

Figure 41 The 3TT P-V surface map when the surface recombination is neglected, the contour lines represent the 3TT device's power density as a function of IBC & PSC operating voltages under STC illumination

4.7 Conclusion

The aim of this chapter is to re-design parameters of Perovskite top cell (layer's thickness) and the architecture of c-Si IBC bottom cell (pitch and emitter/base ratio) to optimize the proposed 3TT model to achieve higher efficiency than that of the basic model.

The first step of optimization was to add an ITO layer to the model to enhance the conductivity of the HTL. This has resulted in a noticeable improvement in FF of the PSC top cell. In addition, the total efficiency of the 3TT model has improved by more than 1%.

The second optimization step was to investigate the influence of the perovskite layer thickness on the total efficiency of the 3TT device. The simulations have revealed that the PCE peaks when the thickness is between 0.8 to 0.9 µm with PCE greater than 31%.

The third optimization step was to investigate the effect of the pitch on the performance of the IBC bottom cell as well as on the PSC top cell. It has been found that the pitch value has a greater influence on the performance of the PSC cell than on the IBC. Moreover, the PCE peaks when the pitch value is smaller. But this is limited by the possible fabrication techniques and costs.

After that the emitter/base ratio in the IBC cell was investigated. It is found that the ratio has no big influence on the performance if the pitch value is small, while it has greater influence if the pitch value is large. In addition, the peak performance ratio for small pitch values is found to be between 1.5:1 and 4:1 while it is between 1:1 to 2:1 when pitch value is large. These results can be beneficial for fabrication firms since they alter the features of the deigned IBC to balance between efficiency and cost.

Additionally, and based on the previous optimization results, four scenarios have been suggested to offer 3TT models that have the highest possible efficiency with different design parameters. The four scenarios were based on different values of pitch and emitter/base ratios and the best perovskite thickness. The models have successfully achieved high PCE (> 31.5 %) with almost matching performance.

Moreover, a contour P-V plot of the best scenario 3TT model was created. The plot represents a map of the power density in 3TT device as a function of the sub-cells' voltages. The map is essential to understand the operating of the 3TT device.

Finally, the influence of the surface recombination between the 3TT device layers was examined. The 3TT model was refined to neglect the effect of this type of recombination losses. The results revealed that most of these loses come from interfaces between the perovskite layer and ETL & HTL layers. If these losses are suppressed, the proposed 3TT tandem device will achieve PCE higher than 33%. In addition, another P-V contour plots of the best scenario device was created when surface recombination is ignored.

5 Conclusion and Recommendations

The main work of this thesis was focused to answer the two research questions:

1. Can a 3TT PSC/c-Si IBC tandem device exceed the SJ limit and compete with 2TT & 4TT devices?
2. Can we improve the design of the tandem cell to increase efficiency of the device?

The answers to these questions were tackled through the different sections of the thesis. This chapter will summarize the main objectives, approaches, results and analysis that fulfill the objectives of this project. Further, conclusions will be drawn on each chapter. Moreover, several suggestions will be recommended to enhance the outcome of 3TT device and to give hints on key themes for future projects and students.

5.1 Conclusion

In chapter 2, the first objective of this project was achieved, which is designing a high efficiency 2-D 3TT PSC/c-Si IBC device's model. This was accomplished by proposing a device structure which complies with 3TT device's working principle where the functionality, material choice, and initial geometry parameters of each layer in the structure were based on experimental and literature references. Furthermore, the simulation and software setups as well as the methodology and process flow were explained. Moreover, optical simulation approach was discussed in more details regarding the use of GenPro4 software as well as the method to produce optical generation depth profiles. As well, electrical simulation approach was discussed for 3TT device's circuitry which more complicated than that of two terminal or four terminal devices. Where 3TT device has independent operational cells but one terminal is shared between them at the same time. We described how to simulate such device in dark and illuminated condition and explained how to obtain J-V curve for each sub-cell.

We also showed the simulated band diagrams of the proposed 3TT device in both dark and illuminated conditions, which showed what was expected theoretically from this structure and confirmed that the device indeed functions as a three-terminal device. Furthermore, the initial simulations were used to show how to obtain J-V curves of each sub-cell and how these curves are related to the terminal which is been swept in voltage.

Meanwhile, the aim of chapter3 was to validate the created 3TT device model and compare its performance with other tandem configuration's performance. Which has been done by confirming the accuracy of optical simulation and the reliability of the applied 2-D optical generation rate profiles in SDE tool. Furthermore, the electrical stimulation in both the IBC bottom cell and the PSC top cells were validated by their correspondent reference SJ cells. This was based on literature data as well as on building separate models for SJ cell to imitate identical structure and parameters for the compared cells.

Furthermore, a comparison in performance between the basic 3TT model and an equivalent 4TT model was conducted. This required building a 4TT PSC/c-Si IBC model which shares identical structure and properties with that of 3TT model except for the two extra layers in between the sub-cells. The comparison revealed that both models show similar capacities to achieve high efficiency (30.38%,

29.69% for 3TT, 4TT models respectively). It can be concluded that the sub-cells of both models have efficient independent operation. However, the 3TT device is more efficient in reducing parasitic losses but the 4TT device can compensate for the parasitic losses by including extra pattern of texture at the top surface of the IBC cell and/or extra ARC. But this extra texture is still difficult to realize in 3TT devices since a flat top surface at the bottom cell is necessary to uncomplicate the fabrication process.

Finally, chapter 4 aim is to redesign parameters of Perovskite top cell (layer's thickness) and the architecture of c-Si IBC bottom cell (pitch and emitter/base ratio) to optimize the proposed 3TT model to achieve higher efficiency than that of the basic model. This has been accomplished by different means of optimization.

Firstly, an ITO layer was added to the model to enhance the conductivity of the HTL. This has resulted in a noticeable improvement in the total efficiency of the 3TT model which has improved by more than 1%.

Secondly, we investigated the influence of the perovskite layer thickness on the total efficiency of the 3TT device. The simulations have revealed that the PCE peaks when the thickness of is between 0.8 to 0.9 μm PCE greater than 31%.

Thirdly, the effect of the changing the IBC cell pitch performance of the sub-cells as well as on the 3TT device was investigated. It has been found that the pitch value has a greater influence on the performance of the PSC cell than on the IBC bottom cell. Moreover, the PCE peaks when the pitch value is smaller. But this is limited by the possible fabrication techniques and costs.

And the final step of optimization was to examine the effect of changing the emitter/base ratio in the IBC cell. It is found that the ratio has no big influence on the performance if the pitch value is small, while it has greater influence if the pitch value is large. In addition, the peak performance ratio for small pitch values is found to be between 1.5:1 and 4:1 while it is between 1:1 to 2:1 when pitch value is large. These results can be beneficial for fabrication industry since they alter the features of the designed IBC to balance between efficiency and cost.

Additionally, four scenarios have been suggested to offer 3TT models that have the highest possible efficiency with different design parameters. The models have successfully achieved high PCE (> 31.5 %) with almost matching performance. Moreover, a contour P-V plot of the best scenario 3TT model was created. The plot represents a map of the power density in 3TT device as a function of the sub-cells' voltages.

Finally, the influence of the surface recombination between the 3TT device layers was examined. The 3TT model was refined to neglect the effect of this type of recombination losses. The results revealed that most of these loses come from interfaces between the perovskite layer and ET L& HTL layers. If these losses are suppressed, the device will achieve PCE higher than 33%.

To wrap it up, the first research question in this project was successfully answered by been able to create a 3TT PSC/c-Si IBC model which achieved an efficiency that exceeded the SQ-limit (>30%) and were capable of competing other tandem configuration such as 4TT devices as it was discussed in section 3.3. The second research question was also answered, since we were able to manipulate the design parameters of both top and bottom cells to increase the efficiency of our 3TT model which was demonstrated in Chapter 4.

5.2 Recommendations

Although this project has fruitful results, but many topics still need to be investigated and improved regarding this type of 3TT devices. The following list summarizes the recommendations that we advise as a continuation of this project or for new projects in future research.

- Since the 3TT model in this project used only a simple one layer of ARC (SiO2), it is recommended to use a more advanced stack of ARC coatings on the front top surface which will reduce the total reflection of the model and consequently improve the efficiency.
- Further, it is recommended to investigate the effect of adding an ultra-thin (<2 nm) layer of SiO_X between the sub-cells followed by a heavily doped n-type polysilicon layer which will allow electrons created in PSC to pass to the bottom cell by tunneling effect (extra passivating layers between sub-cells). And these layers could also improve the blockage of holes from intercrossing. Figure 42 shows a schematic of the 3TT structure after an ultra-thin layer of SiO_2 is added between sub-cells.

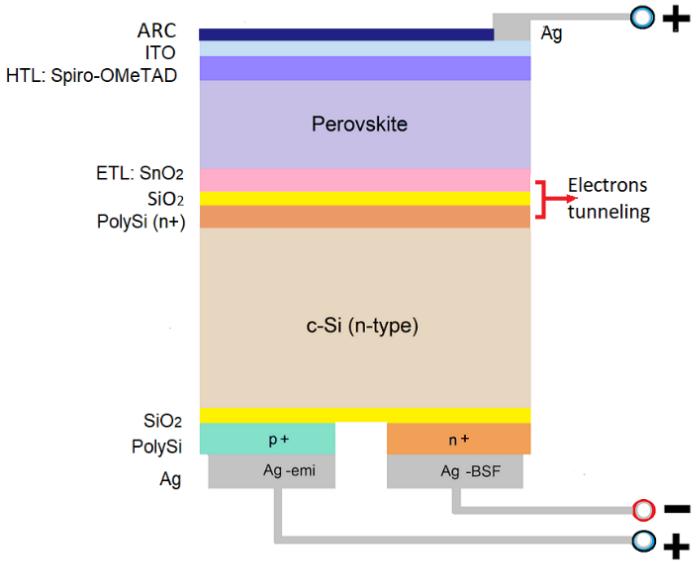

Figure 42 Schematic diagram of 3TT device's structure that includes extra layer of SiO_2 between sub-cells

- Also, different types of perovskite materials can be examined that could lead to better outcome. Since some perovskite variation could offer more suitable band gap energy or larger diffusion length which makes them more useful in certain optimization domains.
- Moreover, different types of HTL materials can be tested for better performance outcome or less costs. In this regard, we recommend examining PEDOT: PSS, PEDOT/graphene, PTAA, or NiOx.
- Likewise, alternative TCO materials can be investigated such FTO, ITiO.
- Finally, adding texture to the front of top cell or front of bottom cell will reduce reflection and increase absorption significantly. But this will require careful adjusting of layer's thickness and will be challenged by increased fabrication complexity and costs. However, it is worth investigation through 2-D modelling since that will deliver an indication whether it is encouraging to continue on this path.

Bibliography

[1] EESI, "Fossil Fuels in 2020," 22 July 2021. [Online]. Available: https://www.eesi.org/topics/fossil-fuels/description. [Accessed 15 June 2022].

[2] P. Friedlingstein, R. A. Houghton, G. Marland, J. Hackler, T. A. Boden, T. J. Conway, J. G. Canadell, M. R. Raupach, P. Ciais & C. Le Quéré, "Update on CO2 emissions," *Nature Geoscience,* vol. 3, pp. 811-812, 21 Nov. 2010.

[3] M. E. Mackay, "Why Solar Energy is Important",Solar Energy: An Introduction, First ed., Oxford: Oxford University Press, 2015, pp. 1-14.

[4] Ram, Manish & Child, Michael & Aghahosseini, Arman & Bogdanov, Dmitrii & Lohrmann, Alena., "A comparative analysis of electricity generation costs from renewable, fossil fuel and nuclear sources in G20 countries for the period 2015-2030," *Journal of Cleaner Production,* vol. 199, pp. 687-704, 2018.

[5] Goody, R. M.; Yung, Y. L., Atmospheric Radiation: Theoretical Basis, Second ed., Oxford,UK: Oxford University Press. ISBN 978-0-19-510291-8, 1989.

[6] C. Gueymard, "The Sun's total and spectral irradiance for solar energy applications and solar radiation models," *Solar Energy,* vol. 76, no. 39, pp. 423-453, 2004.

[7] Fahrenbruch, A. L., and Bube, R. H., Fundamentals in Solar Cells, New York: Academic Press, 1983.

[8] Arno Smets, Klaus Jäger, Olindo Isabella, René van Swaaij, Miro Zeman, Solar Energy: The physics and engineering of photovoltaic conversion, technologies and systems, First ed., Cambridge: UIT Cambridge Limited, 2016, p. 462.

[9] R. Raffaelle, Fundamentals of photovoltaics, NREL: John Wiley & Sons Canada, Limited, 2015, pp. 27-45.

[10] T. Dittrich, Materials Concepts for Solar Cells, Imperial College Press, ISBN 978-1-78326-444-5, 2015, p. 552.

[11] Alan L. Fahrenbruch, Richard H. Bube, CHAPTER 6 - THE CALCULATION OF SOLAR EFFICIENCY;“Fundamentals of Solar Cells”, Academic Press, 1983, pp. 210-244.

[12] S. Odeh, "Analysis of the Performance Indicators of the PV Power System," *Journal of Power and Energy Engineering,* vol. 6, no. 6, pp. 59-75, 2018.

[13] Jozef Szlufcik, Siva Sivoththaman, Johan F. Nijs, Robert P. Mertens, Roger Van Overstraeten, McEvoy's Handbook of Photovoltaics, Third ed., Academic Press, ISBN 9780128099216, 2018, pp. 129-158.

[14] Yoshikawa, K., Kawasaki, H., Yoshida, W., Irie, T., Konishi, K., Nakano, K.,Yamamoto, K., "Silicon heterojunction solar cell with interdigitated back contacts for a photoconversion efficiency over 26%," *Nature Energy,* vol. 2, no. 5, p. 15, 2017.

[15] E. Van Kerschaver, S. De Wolf and J. Szlufcik, "Towards back contact silicon solar cells with screen printed metallisation," *IEEE, Conference Record of the Twenty-Eighth IEEE Photovoltaic Specialists Conference,* vol. 37, no. 36, pp. 209-212, 2000.

[16] M.K. Mat Desa, S. Sapeai, A.W. Azhari, K. Sopian, M.Y. Sulaiman, N. Amin,, "Silicon back contact solar cell configuration: A path way towards higher efficiency," *Renewable and Sustainable Energy Reviews,* vol. 60, pp. 1516-1532, 2016.

[17] Lee, Youn-Jung & Kim, Byung-Sung & Ifitiquar, S. & Park, Cheolmin & Yi, Junsin, "Silicon solar cells: Past, present and the future," *Journal of the Korean Physical Society,* vol. 65, pp. 355-361, 2014.

[18] Di Yan, Andres Cuevas, Josua Stuckelberger, Er-Chien Wang, Sieu Pheng Phang,Teng Choon Kho, Jesús Ibarra Michel, Daniel Macdonald, James Bullock, "Silicon solar cells with passivating contacts: Classification and performance," *PHOTOVOLTAICS-Wiley,* no. SPECIAL ISSUE ARTICLE, p. 17, 2022.

[19] Kai Carstens, Morris Dahlinger, Erik Hoffmann, Jürgen R. Köhler, Renate Zapf-Gottwick, Jürgen H. Werner,, "Universal Passivation for p++ and n++ Areas on IBC Solar Cells," *Energy Procedia,* vol. 77, pp. 779-785, 2015.

[20] M. Belarbi , M. Beghdad , A. Mekemeche, "Simulation and optimization of n-type interdigitated back silicon heterojunction (IBC-SiHJ) solar cell structure using Silvaco Tcad Atlas," *Solar Energy,* vol. 127, pp. Pages 206-215,, 2016.

[21] Chopra, K. & Paulson, Puthur & Dutta, Viresh, "Thin-Film Solar Cells: An Overview. Progress in Photovoltaics," *PROG PHOTOVOLTAICS,* vol. 12, pp. 69-92, 2004.

[22] Edoff, M. et al., "Thin Film Solar Cells: Research in an Industrial Perspective," *Ambio,* vol. 41, no. Suppl 2, pp. 8-112, 2012.

[23] P. e. a. Sinha, "Life cycle materials and water management for CdTe photovoltaics," *Solar Energy Materials & Solar Cells,* vol. 119, p. 271–275, 2013.

[24] Powalla, Michael; Paetel, Stefan; Ahlswede, Erik; Wuerz, Roland; Wessendorf, Cordula D.; Magorian Friedlmeier, Theresa, "Thin-film solar cells exceeding 22% solar cell efficiency: An overview on CdTe-, Cu(In,Ga)Se2-, and perovskite-based materials," *Applied Physics Reviews,* vol. 5, no. 4, 2018.

[25] NREL, "Best Research-Cell Efficiency Chart, Photovoltaic Research," NREL, 05 July 2022. [Online]. Available: https://www.nrel.gov/pv/assets/pdfs/best-research-cell-efficiencies-rev220630.pdf. [Accessed 15 August 2022].

[26] L. Hamers, "Perovskites power up the solar industry," Science News, 26 July 2017. [Online]. Available: https://www.sciencenews.org/article/perovskites-power-solar-industry. [Accessed 23 June 2022].

[27] Wan-Jian Yin, Tingting Shi, Yanfa Yan, "Unique Properties of Halide Perovskites as Possible Origins of the Superior Solar Cell Performance," *Advanced Materials,* vol. 26, no. 27, p. 4653–4658, 2014.

[28] Jiang, Yan; Qiu, Longbin; Juarez-Perez, Emilio J.; Ono, Luis K.; Hu, Zhanhao; Liu, Zonghao; Wu, Zhifang; Meng, Lingqiang; Wang, Qijing; Qi, Yabing, "Reduction of lead leakage from damaged lead halide perovskite solar modules using self-healing polymer-based encapsulation," *Nature Energy,* vol. 4, no. 7, p. 585–593, 2019.

[29] Chen, Yichuan and Zhang, Linrui and Zhang, Yongzhe and Gao, Hongli and Yan, Hui, "Large-area perovskite solar cells – a review of recent progress and issues," *The Royal Society of Chemistry RSC,* vol. 8, no. 19, pp. 10489-10508, 2018.

[30] P. Tockhorn, "PhD thesis "Minimising Optical and Electrical Losses in Perovskite Solar Cells − From Single-Junctions to Advanced Tandem Designs"," Technischen Universität Berlin, Berlin, 2021.

[31] Richter, Armin & Hermle, Martin & Glunz, Stefan, "Reassessment of the Limiting Efficiency for Crystalline Silicon Solar Cells," *IEEE Journal of Photovoltaics,* vol. 3, pp. 1184-1191, 2013.

[32] De Vos, A. et al., "Detailed balance limit of the efficiency of tandem solar cells," *Journal of Physics D: Applied Physics,* vol. 13, no. 5, p. 839–846, 1980.

[33] A. De Vos & H. Pauwels, "n the Thermodynamic Limit of Photovoltaic Energy Conversion," *Appl. Phys.,* vol. 25, no. 2, p. 119–125, 1981.

[34] Yamaguchi, Masafumi, Dimroth, Frank, Geisz, John F., & Ekins-Daukes, Nicholas J., "Multi-Junction Solar Cells Paving the Way for Super High-Efficiency," *Journal of Applied Physics,* vol. 129, no. 240901, pp. 1-15, 2021.

[35] D. McMeekin, et al., "A mixed-cation lead mixed-halide perovskite absorber for tandem solar cells," *Science,* vol. 351, p. 151, 2016.

[36] Chen, Bo; Zheng, Xiaopeng; Bai, Yang; Padture, Nitin P.; Huang, Jinsong, "Progress in Tandem Solar Cells Based on Hybrid Organic-Inorganic Perovskites," *Advanced Energy Materials,* vol. 7, no. 14:1602400, p. 13, 2017.

[37] J. e. a. Tong, "Carrier lifetimes of >1 µs in Sn-Pb perovskites enable efficient all-perovskite tandem solar cells," *Science,* vol. 364, p. 475–479, 2019.

[38] H. Imran, I. Durrani, M. Kamran, T. M. Abdolkader, M. Faryad and N. Z. Butt, "High-Performance Bifacial Perovskite/Silicon Double-Tandem Solar Cell," *IEEE Journal of Photovoltaics,* vol. 8, no. 5, pp. 1222-1229, 2018.

[39] James M. Gee et al., "A comparison of different module configurations for multi-band-gap solar cells," *Solar Cells,* vol. 24, no. 1-2, pp. 147-155, 1988.

[40] S. Akhil, S. Akash, Altaf Pasha, Bhakti Kulkarni, Mohammed Jalalah, Mabkhoot Alsaiari, Farid A. Harraz, R Geetha Balakrishna,, "Review on perovskite silicon tandem solar cells: Status and prospects 2T, 3T and 4T for real world conditions," *Materials & Design,* vol. 211, no. 110138, 2021.

[41] Ongqi Li, Yingzhi Zhao, Xi Wang, Yuchao Sun, Zhiguo Zhao, Yujing Li, Huanping Zhou, Qi Chen, "Cost Analysis of Perovskite Tandem Photovoltaics," *Joule,* vol. 2, no. 8, pp. 1559-1572, 2018.

[42] Köhnen, E.; Jošt, M.; Morales-Vilches, A. B.; Tockhorn, P.; Al-Ashouri, A.; Macco, B.; Kegelmann, L.; Korte, L.; Rech, B.; Schlatmann, R.; Stannowski, B.; Albrecht, S., "Highly efficient monolithic perovskite silicon tandem solar cells: analyzing the influence of current mismatch on device," *Sustainable Energy Fuels,* vol. 3, p. 1995, 2019.

[43] R. Now, "Q Cells hits 28.7% efficiency for 2T perovskite-silicon tandem solar cell," Renewables Now, 08 March 2022. [Online]. Available: https://www.renewablesnow.com/news/q-cells-hits-287-efficiency-for-2t-perovskite-silicon-tandem-solar-cell-776072/. [Accessed 17 Aug. 2022].

[44] CSEM, "NEW WORLD RECORDS: PEROVSKITE-ON-SILICON-TANDEM SOLAR CELLS," CSEM & EPFL, 7 July 2022. [Online]. Available: https://www.csem.ch/press/new-world-records-perovskite-on-silicon-tandem-solar?pid=172296. [Accessed 9 Oct. 2022].

[45] Fabrizio Gota, Malte Langenhorst, Raphae Schmager, Jonathan Lehr, Ulrich W. Paetzold, "Energy Yield Advantages of Three-Terminal Perovskite-Silicon Tandem Photovoltaics," *Joule,* no. https://doi.org/10.1016/j.joule.2020.08.021, pp. 1-18, 2020.

[46] Emily L. Warren, William E. McMahon, Michael Rienäcker, Kaitlyn T. VanSant, Riley C. Whitehead, Robby Peibst, and Adele C. Tamboli, "A Taxonomy for Three-Terminal Tandem Solar Cells," *ACS Energy Letters,* vol. 5, no. 4, pp. 1233-1242, 2020.

[47] Chen, B., Baek, SW., Hou, Y. et al., "Enhanced optical path and electron diffusion length enable high-efficiency perovskite tandems," *Nature Commun,* vol. 11, no. 1257, 2020.

[48] Philipp Tockhorn, Johannes Sutter, Alexandros Cruz et al., "Nano-optical designs enhance monolithic perovskite/silicon tandem solar cells toward 29.8% efficiency," *Research Square,* no. PREPRINT (Version 1), p. 11, 2022.

[49] Yu Z. J., Leilaeioun M., Holman Z., "Selecting tandem partners for silicon solar cells," *Nature Energy,* vol. 1, no. 16137, 2016.

[50] Philipp Tockhorn, Philipp Wagner, Lukas Kegelmann, Johann-Christoph Stang, Mathias Mews, Steve Albrecht, and Lars Korte, "Three-Terminal Perovskite/Silicon Tandem Solar Cells with Top and Interdigitated Rear Contacts," *ACS Applied Energy Materials,* vol. 3, no. 2, pp. 1381-1392, 2020.

[51] R. Santbergen, H. Uzu, K. Yamamoto and M. Zeman, "Optimization of Three-Terminal Perovskite/Silicon Tandem Solar Cells," *IEEE Journal of Photovoltaics,* vol. 9, no. 2, pp. 446-451, 2019.

[52] Park I. J., Ji S. G., Park M.-A., Jang J. H., Kim J.Y. , " Three-Terminal Monolithic Perovskite/Si Tandem Solar Cell Characterization Platform," *Joule,* vol. 3, no. 807, 2019.

[53] Chiang S. Y., Carbajal B. G., Wakefield G. F., "Improved performance thin solar cells," *IEEE Trans. Electron Devices,* vol. 25, p. 1405−1409, 1978.

[54] Emily L. Warren, Michael G. Deceglie, Michael Rien¨acker, Robby Peibst, "Maximizing tandem solar cell power extraction using a three-terminal design," *The Royal Society of Chemistry,* vol. 2, pp. 1141-1147, 2018.

[55] Manuel Schnabel, Henning Schulte-Huxel, Michael Rienäcker, Emily L. Warren, Paul F., "Three-Terminal III-V/Si Tandem Solar Cells Enabled by a Transparent Conductive Adhesive," *Sustainable Energy & Fuels,* vol. 2, no. 1-3, pp. 1-12, 2019.

[56] J.P. Connolly, Koffi Ahanogbe, Jean-Paul Kleider, J Alvarez, Hiroyuki Kanda,, "Recent results on carrier selective three terminal perovskite on silicon-IBC tandem solar cells," in *37th European Photovoltaic Solar Energy Conference and Exhibition (EU PVSEC 2020)*, Lisbon, Portugal, 2020.

[57] Zakaria Djebbour, Walid El-Huni, Anne Migan-Dubois, Jean-Paul Kleider, "Bandgap engineered smart three-terminal solar cell: New perspectives towards very high efficiencies in the silicon world," *Progress in Photovoltaics, Wiley,* vol. 27, no. 4, p. 306, 2019.

[58] P. Procel, G. Yang, O. Isabella and M. Zeman, "Numerical Simulations of IBC Solar Cells Based on Poly-Si Carrier-Selective Passivating Contacts," *IEEE Journal of Photovoltaics,* vol. 9, no. 2, pp. 374-384, 2019.

[59] Z. Hawash, L.K. Ono, Y. Qi, "Recent Advances in Spiro-MeOTAD Hole Transport Material and Its Applications in Organic-Inorganic Halide Perovskite," *Solar Cells,* vol. 5, no. 1700623, https://onlinelibrary.wiley.com/doi/abs/10.1002/admi.201700623, 2018.

[60] J. H. Heo, M. H. Lee, M. H. Jang, and S. H. Im, "Highly efficient CH3NH3PbI3−xClx mixed halide perovskite solar cells prepared by re-dissolution and crystal grain growth via spray coating," *J. Mater. Chem.,* vol. 4, no. 45, p. 17636–17642, 2016.

[61] Seongrok Seo, Sooeun Shin, Eunsoo Kim, Seonghwa Jeong, Nam-Gyu Park,and Hyunjung Shin, "Amorphous TiO2 Coatings Stabilize Perovskite Solar Cells," *ACS Energy Lett.,* vol. 6, no. DOI: 10.1021/acsenergylett.1c01446, p. 3332−3341, 2021.

[62] Filipe Martinho, "Challenges for the future of tandem photovoltaics on the path to terawatt levels: a technology review," *Energy & Environmental Science,* no. 7, https://doi.org/10.1039/D1EE00540E, pp. 1-50, 2021.

[63] D. Diouf, J.P. Kleider, T. Desrues, P.-J. Ribeyron, "Effects of the front surface field in n-type interdigitated back contact silicon heterojunctions solar cells," *Energy Procedia,* vol. 2, no. 1, https://doi.org/10.1016/j.egypro.2010.07.011, pp. 59-64, 2010.

[64] Stefan W. Glunz, Frank Feldmann, "SiO2 surface passivation layers – a key technology for silicon solar cells," *olar Energy Materials and Solar Cells,* vol. 185, no. , ISSN 0927-0248, https://doi.org/10.1016/j.solmat.2018.04.029, pp. 260-269, 2018.

[65] Jiakai Zhou, Qian Huang, Yi Ding, Guofu Hou, Ying Zhao, "Passivating contacts for high-efficiency silicon-based solar cells: From single-junction to tandem architecture," *Nano Energy,* vol. 92, no. 106712, ISSN 2211-2855, https://doi.org/10.1016/j.nanoen.2021.106712, 2022.

[66] Synopsys, "Sentaurus Device-An advanced multidimensional (1D/2D/3D) device simulator," Synopsys(c), [Online]. Available: https://www.synopsys.com/silicon/tcad/device-simulation/sentaurus-device.html. [Accessed 14 April 2022].

[67] COMSOL.Trustees, "The Finite Element Method (FEM)," COMSOL, 21 Feb. 2017. [Online]. Available: https://www.comsol.com/multiphysics/finite-element-method. [Accessed 20 May

2022].

[68] Stanford.edu, "Sentaurus Workbench," Synopsys©, 3 Sep. 2011. [Online]. Available: https://web.stanford.edu/class/ee328/swb/swb_a.html. [Accessed 15 April 2022].

[69] Chatterjee, Somenath, Sumeet Singh and Himangshu Pal, "Effect of Multijunction Approach on Electrical Measurements of Silicon and Germanium Alloy Based Thin-Film Solar Cell Using AMPS-1D," *International Journal of Photoenergy,* no. DOI:10.1155/2014/653206, pp. 1-6, 2014.

[70] Bae, M., Estrada, D., Liao, A.D., Lyons, A.S., Ong, Z., Ramasubramanian, B., Xiong, F., Wood, J.D., Datta, S., & Fuhrer, "MOBILITY AND SATURATION VELOCITY IN GRAPHENE ON SILICON DIOXIDE BY VINCENT E. DORGAN THESIS Submitted in partial fulfillment of the requirements for the degree of Master of Science in Electrical and Computer Engineering.," *M.S.,* pp. 1-73, 2010.

[71] Andyaningrum Fauziah, "Electrical Simulations of Perovskite/c-Si Tandem Solar Cells, Master thesis in Sustainable Energy Technology, Delft University of Technology," Photovoltaic Materials and Devices Group, EEMCS, TU Delft, Delft, , 2021.

[72] Neukom MT, Schiller A, Züfle S, Knapp E, Ávila J, Pérez-Del-Rey D, Dreessen C, Zanoni KPS, Sessolo M, Bolink HJ, Ruhstaller B. Consistent, "Device Simulation Model Describing Perovskite Solar Cells in Steady-State, Transient, and Frequency Domain," *ACS Appl Mater Interfaces,* vol. 11, no. 26, pp. 23320-23328., 2019.

[73] Samuel D Stranks, Giles E Eperon, et al., "Electron-hole diffusion lengths exceeding 1 micrometer in an organometal trihalide perovskite absorber," *Science,* vol. 342, no. 6156, p. 341–344, 2013.

[74] Rik van Heerden, Paul Procel, Luana Mazzarella, Rudi Santbergen and Olindo Isabella, "Slow Shallow Energy States as the Origin of Hysteresis in Perovskite Solar Cells," *Frontiers in Photonics,* vol. Sec. Photovoltaic Materials and Devices, pp. 1-13, 2022.

[75] A. Alnuaimi, I. Almansouri, and A. Nayfeh, "Effect of mobility and band structure of hole transport layer in planar heterojunction perovskite solar cells using 2D TCAD simulation," *J. Comput. Electron.,* vol. 15, no. 3, p. 110–1118, 2016.

[76] Rui Huang, Jiyu Tang, "Simulation studies on the electron transport layer based perovskite solar cell to achieve high photovoltaic efficiency," *Journal of Physics: Conference Series,* vol. 2083, no. 02201, doi:10.1088/1742-6596/2083/2/022011, pp. 2-9, 2021.

[77] Steffens, Jonathan., "Dependencies Between poly-Si Composition and Solar Cell Performance of poly-Si/SiOx Passivating Contacts, PhD dissertation," Konstanzer Online-Publikations-System (KOPS), Konstanz, 2020.

[78] Terence K.S. Wong * and Keyi Pei, "Double Heterojunction Crystalline Silicon Solar Cells: From Doped Silicon to Dopant-Free Passivating Contacts," *Photonics,* vol. 9, no. 477, https://doi.org/10.3390/photonics9070477, pp. 1-32, 2022.

[79] C Flynn, D König, I Perez-Wurfl, M A Green and G Conibeer, "Correlation between fixed charge and capacitance peaks in silicon nanocrystal metal–insulator–semiconductor devices," *Semicond. Sci. Technol. 25 045011,* vol. 25, no. 045011, DOI:10.1088/0268-1242/25/4/045011,

2010.

[80] Xie Zhang, Jimmy-Xuan Shen, Wennie Wang, and Chris G. Van de Walle, "First-Principles Analysis of Radiative Recombination in Lead-Halide Perovskites," *ACS Energy Lett.,* vol. 3, no. 10, https://doi.org/10.1021/acsenergylett.8b01297, p. 2329–2334, 2018.

[81] Jakapan Chantana, Yu Kawano, Takahito Nishimura, Abdurashid Mavlonov, Qing Shen, Kenji Yoshino, Satoshi Iikubo, Shuzi Hayase, Takashi Minemoto, "Impact of Auger recombination on performance limitation of perovskite solar cell," *Solar Energy,* vol. 217, no. ISSN 0038-092X, https://doi.org/10.1016/j.solener.2021.02.018, pp. 342-353, 2021.

[82] Y Arafat , F Mohammedy , M Shahidul Hassan, "Optical and Other Measurement Techniques of Carrier Lifetime in Semiconductors," *International Journal of Optoelectronic Engineering,* vol. 2, no. 2, doi: 10.5923/j.ijoe.20120202.02, pp. 5-11, 2012.

[83] M. Singh, R. Santbergen, L. Mazzarella, A. Madrampazakis, G. Yang, R. Vismara, Z. Remes, A. Weeber, M. Zeman, O. Isabella, "Optical characterization of poly-SiOx and poly-SiCx carrier-selective passivating contacts," *Solar Energy Materials and Solar Cells,* vol. 210, no. 110507, ISSN 0927-0248, 2020.

[84] Fuhua Hou, Can Han, Olindo Isabella, Lingling Yan, Biao Shi, Junfan Chen, Shichong An, Zhongxin Zhou, Wei Huang, Huizhi Ren, Qian Huang, Guofu Hou, Xinliang Chen, Yuelong Li, Yi Ding, Guangcai Wang, Changchun Wei, Dekun Zhang, Miro Zeman, Ying Zhao, Xiaod, "Inverted pyramidally-textured PDMS antireflective foils for perovskite/silicon tandem solar cells with flat top cell," *Nano Energy,* vol. 56, no. ISSN 2211-2855, pp. 234-240, 2019.

[85] D. Rossi, F. Santoni, M. Auf Der Maur and A. Di Carlo, "A Multiparticle Drift-Diffusion Model and its Application to Organic and Inorganic Electronic Device Simulation," *IEEE Transactions on Electron Devices,* vol. 66, no. 6, pp. 2715-2722, 2019.

[86] Dricus De Rooij, "Dark IV Measurements," SINO VOLTAICS, 11 Aug. 2017. [Online]. Available: https://sinovoltaics.com/learning-center/basics/dark-iv-measurements/. [Accessed 17 Sep. 2022].

[87] G. Yang, A. Ingenito, O. Isabella, and M. Zeman, "IBC c-Si solar cells based on ion-implanted poly-silicon passivating contacts," *Sol. Energy Mater. Sol. Cells,* pp. 1-7, 2016.

[88] Dong Yang, Ruixia Yang, Kai Wang, Congcong Wu, Xuejie Zhu, Jiangshan Feng, Xiaodong Ren, Guojia Fang, Shashank Priya & Shengzhong (Frank) Liu, "High efficiency planar-type perovskite solar cells with negligible hysteresis using EDTA-complexed SnO2," *Nature Communications,* vol. 9, no. 3239, https://doi.org/10.1038/s41467-018-05760-x, 2018.

[89] Arthur Onno, Nathan Rodkey, Amir Asgharzadeh, Salman Manzoor, Zhengshan J., "Predicted Power Output of Silicon-Based Bifacial Tandem Photovoltaic Systems, Supplemental Information," *JOUL,* vol. 4, no. 3, https://doi.org/10.1016/j.joule.2019.12.017., pp. 580-596, 2020.

[90] Peng Dong, Yuming Zhang, Hui Guo, Chenxu Zhang, Jikui Ma, Xiaoyong Qu, "Efficient Low-Cost IBC Solar Cells with a Front Floating Emitter: Structure Optimization and Passivation Layer Study," *Energies,* vol. 11, no. 4: 939, https://doi.org/10.3390/en11040939, pp. 1-9, 2018.

[91] Pawlak BJ,Sojka B,Robbelein J,Singh S,Janssens T, Das J et al., "Industrial integration of interdigitated back-contact Si solar cells by laser ablation," in *Proceedings of the 37th IEEE photovoltaic specialists conference (PVSC), p.001116–001118.*, doi: 10.1109/PVSC.2011.6186148., 2011.

[92] Takashi Minemoto and Masashi Murata., "Device modeling of perovskite solar cells based on," *Journal of applied physics,* vol. 116, no. 054505, 2014.

[93] Dmitry Poplavskyy and Jenny Nelson, "Nondispersive hole transport in amorphous films of methoxy-spirofluorene-arylamine organic compound," *Journal of Applied Physics,* vol. 93, no. 1, p. 341–346, 2003.

[94] Dianyi Liu and Timothy L Kelly, "Perovskite solar cells with a planar heterojunction structure prepared using room-temperature solution processing techniques," *Nature photonics,* vol. 8, no. 2, pp. 133-138, 2014.

[95] G. Yang, P. Guo, P. Procel, A. Weeber, O. Isabella, and M. Zeman, "Poly-crystalline silicon-oxide films as carrier-selective passivating contacts for c-Si solar cells," *App;. Phys. Lett.,* vol. 112, no. 19, pp. 1-6, 2018.

[96] Paul Procel, Haiyuan Xu, Aurora Saez, Carlos Ruiz-Tobon, Luana Mazzarella, Yifeng Zhao,Can Han, Guangtao Yang, Miro Zeman, Olindo Isabella, "The role of heterointerfaces and subgap energy states on transport mechanisms in silicon heterojunction solar cells," *Prog. Photovoltaics Res. Appl.,,* vol. 28, no. 9, p. 935–945, 2020.

[97] Luan Y, Yi X, Mao P, Wei Y, Zhuang J, Chen N, Lin T, Li C, Wang J. , "High-Performance Planar Perovskite Solar Cells with Negligible Hysteresis Using 2,2,2-Trifluoroethano," *iScience,* no. doi: 10.1016/j.isci.2019.06.004., pp. 433-441, 2019.

[98] Alexander J. Bett*, Kristina M. Winkler, Martin Bivour, Ludmila Cojocaru, Özde Ş. Kabakli, Patricia S. C. Schulze, Gerald Siefer, Leonard Tutsch, Martin Hermle, Stefan W. Glunz, and Jan Christoph Goldschmidt, "Semi-Transparent Perovskite Solar Cells with ITO Directly Sputtered on Spiro-OMeTAD for Tandem Applications," *ACS Appl. Mater. Interfaces,* vol. 11, no. 49, https://doi.org/10.1021/acsami.9b17241, p. 45796–45804, 2019.

[99] Di Yan, Andres Cuevas, Josua Stuckelberger, Er-Chien Wang, Sieu Pheng Phang2, Teng Choon Kho2 , Jesús Ibarra Michel, "Silicon solar cells with passivating contacts: Classification and performance," *Prog Photovolt Res Appl.,* no. S P E C I A L I S S U E AR T I C L E, DOI: 10.1002/pip.3574, pp. 1-17, 2022.